Synthesis and characterization of novel highly-functional zeolites for vehicle emission control

（自動車排ガス浄化用新規高機能ゼオライトの合成とキャラクタリゼーション）

by

Yusuke Naraki

Submitted to Hiroshima University

In partial fulfillment of the requirements for the degree of
Philosophy of Doctor

Supervisor: Professor Dr. Tsuneji Sano

Department of Applied Chemistry,
Graduate School of Engineering,
Hiroshima University

September 2017

Referee in Chief: Professor Tsuneji Sano

Referees: Professor Takeshi Shiono

Professor Shinjiro Hayakawa

Associate Professor Masahiro Sadakane

Department of Applied Chemistry,
Graduate School of Engineering,
Hiroshima University

Chapter 1

An Overview

1. Zeolites

1.1. What are zeolites?

1.1.1. Structure, composition and chemistry

Zeolites are a group of aluminosilicate minerals that are found naturally or synthesized. Silicon and aluminium atoms in zeolites are tetrahedrally coordinated and connected with each other via oxygen atoms periodically, forming crystalline three-dimensional networks. The structures of zeolites typically have “micropores” defined as the pore opening of < 2 nm, expressed as the minimum number of T-atoms (tetrahedral atoms in the framework) that form rings (e.g. 8-membered rings, 8MR; 10-membered rings, 10MR; and 12-membered rings, 12MR) surrounding the channel [1,2]. Zeolites are often differentiated as zero to three dimensional according to the number of micropores in different crystallographic directions [3,4]. Figure 1-1 shows some examples of zeolite structures. In most cases, channels are interconnected with each other in two- or three-dimensional zeolites, forming unique and complex channel systems. Each zeolite structure is named with three-letter alphabetical codes as shown in Table 1-1 by International Zeolite Association (IZA) according to its framework topology, not composition.

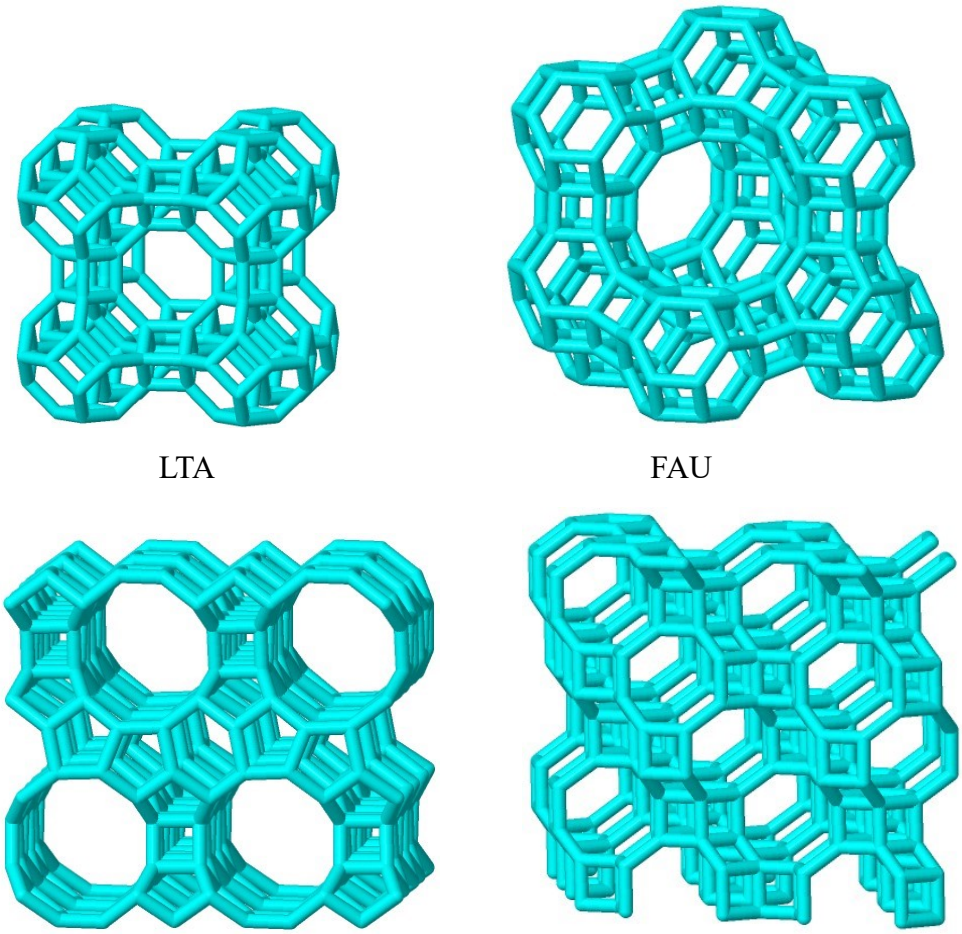

Figure 1-1 Structural models of zeolites. Oxygen atoms and ionic radius are not described.

Table 1-1 Framework type codes (IZA website [3]).

Fully ordered Type Materials *

ABW	ACO	AEI	AEL	AEN	AET	AFG	AFI	AFN	AFO	AFR	AFS	AFT	AFV	AFX
AFY	AHT	ANA	APC	APD	AST	ASV	ATN	ATO	ATS	ATT	ATV	AVL	AWO	AWW
BCT	BEC	BIK	BOF	BOG	BOZ	BPH	BRE	BSV	CAN	CAS	CDO	CFI	CGF	CGS
CHA	-CHI	-CLO	CON	CSV	CZP	DAC	DDR	DFO	DFT	DOH	DON	EAB	EDI	EEI
EMT	EON	EPI	ERI	ESV	ETL	ETR	EUO	EZT	FAR	FAU	FER	FRA	GIS	GIU
GME	GON	GOO	HEU	IFO	IFR	-IFU	IFW	IFY	IHW	IMF	IRN	IRR	-IRY	ISV
ITE	ITG	ITH	ITR	ITT	-ITV	ITW	IWR	IWS	IWV	IWW	JBW	JNT	JOZ	JRY
JSN	JSR	JST	JSW	KFI	LAU	LEV	LIO	-LIT	LOS	LOV	LTA	LTF	LTJ	LTL
LTN	MAR	MAZ	MEI	MEL	MEP	MER	MFI	MFS	MON	MOR	MOZ	MSE	MSO	MTF
MTN	MTT	MTW	MVY	MWF	MWW	NAB	NAT	NES	NON	NPO	NPT	NSI	OBW	OFF
OKO	OSI	OSO	OWE	-PAR	PAU	PCR	PHI	PON	POS	PSI	PUN	RHO	-RON	RRO
RSN	RTE	RTH	RUT	RWR	RWY	SAF	SAO	SAS	SAT	SAV	SBE	SBN	SBS	SBT
SEW	SFE	SFF	SFG	SFH	SFN	SFO	SFS	SFW	SGT	SIV	SOD	SOF	SOS	SSF
SSY	STF	STI	STT	STW	-SVR	SVV	SZR	TER	THO	TOL	TON	TSC	TUN	UEI
UFI	UOS	UOV	UOZ	USI	UTL	UWY	VET	VFI	VNI	VSV	WEI	-WEN	YUG	ZON

Partially disordered Type Materials

*BEA
*-EWT
*-ITN
*MRE
*SFV
*-SSO
*STO

The chemical formula of zeolites is generally written in the form of mixed oxides as $M^{n+}_{2/n}O{\cdot}xSiO_2{\cdot}Al_2O_3{\cdot}yH_2O$, wherein M means hydrogen, alkali metals, or alkaline earth metals, $x \geq 2$, and $y \geq 0$. Since the trivalent Al^{3+} has four bondings with neighboring oxygen (O-Si), one aluminium atom in the framework of zeolites generates a negative charge, being compensated by the cation M^{n+}. If the M^{n+} is H^+, it works as an acid site in zeolites. The schematic description of the acid site in zeolites is shown in Figure 1-2. Zeolites with lower x (typically x = 2–5) are called “low-silica zeolites”, which shows hydrophilicity due to the electrical charges by abundant aluminium atoms. In contrast, zeolites with higher x (typically $x \geq 5$) are called “high-silica zeolites”. High-silica zeolites have less aluminium atoms and are more hydrophobic than low-silica zeolites [5]. Zeolites with pure silica composition ($x \approx \infty$) is also known to be synthesized [6]. Hydrated zeolites contain water molecules in the structures. The value y is variable because the water molecules in zeolites easily move by adsorption and desorption depending on partial pressure of water and temperature.

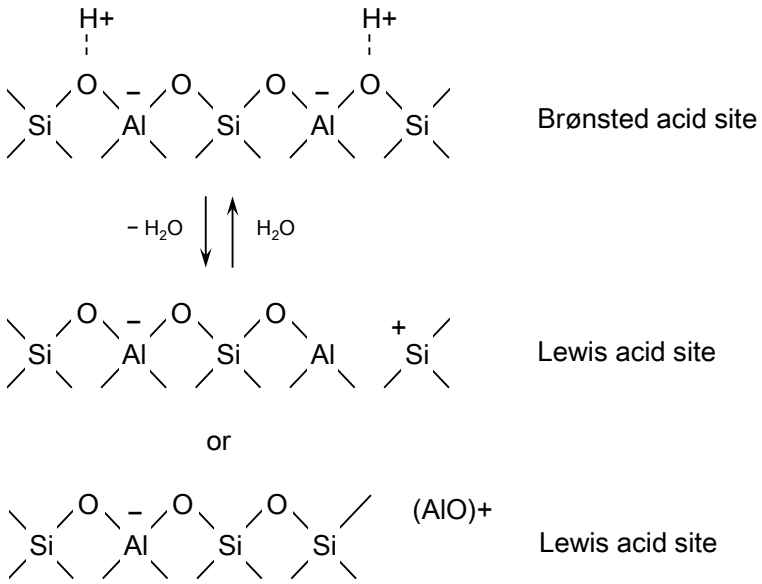

Figure 1-2 Acid sites in zeolites. Lewis acid sites generate by dehydration from Brønsted acid sites or dealumination.

Since zeolites have micropores, they can adsorb various molecules with the size smaller than their pore opening. Due to the well-defined structures, zeolites have a narrow distribution of the micropore size compared to e.g. activated carbons [7,8]. Taking advantage of these characteristics, molecules with different sizes can be separated by zeolites ("molecular sieving") [9]. Zeolites also work as ion-exchangers. Charge compensating cations at aluminium sites can be exchanged by other cations by commonly known methods such as liquid-phase ion exchange [10]. Another function of zeolites is catalysis on a variety of reactions. In catalysis, H^+ zeolites and other metal-exchanged zeolites with diverse structures have been studied so far [11-13].

1.1.2. General applications

Based on the functions referred in section 1.1.1., zeolites are used in worldwide as water softener (in detergent), dehydrating agents, cracking catalysts in petrochemical industry, fine chemicals catalysts, vehicle emission control catalysts, and so on. General

applications of zeolites are listed in Table 1-2.

Table 1-2 General applications of zeolites (referred to the website of Tosoh Corporation)

Field	Applications
Gas Production	Separation of nitrogen and oxygen from air H_2 purification in PSA processes Removal of carbon dioxide and moisture from air Purification in cryogenic processes
Chemical **Petrochemical**	Fine chemicals catalysts Drying of naphtha cracked gas Drying of organic solutions Petroleum refining (hydrocracking, isomerization, dewaxing etc.) Petrochemical catalysts (alkylation, isomerization etc.)
Environment	Adsorption of hydrocarbons in vehicle emissions Removal of nitrogen oxides (NO_x) in vehicle emissions Removal of emissions from semiconductor production Adsorption of volatile organic compound (VOC) Adsorption of radioactive ions (Cs^+, Sr^{2+} etc.) Deodorization
Living	Water softening for detergents Drying and purification of refrigerants Prevention of cloudiness in multilayer glass Removal of trace moisture from urethane paints and sealants Desulfurization for fuel cells Drying of vacuum insulation panels Moisture control in pharmaceutical and food packaging

1.2. Synthesis of zeolites

1.2.1. Brief history of synthetic zeolites

The first synthetic zeolite was levynite, reported in the mid-19th century [14]. However, an important work in the field of synthetic zeolites was done by R. M. Barrer in 1940s who established well-defined synthesis with reproducibility [15]. Following his pioneering work, Milton and co-workers in Union Carbide Corporation first

synthesized A, X and Y type zeolites [16]. They also first industrialized commercial synthetic zeolites. In late-1960s, Mobil Oil Corporation discovered new high-silica zeolites (beta and ZSM-5) using organic molecules as templates [17,18]. With the use of organic templates, also called “organic structure-directing agents” (OSDA), the number of newly synthesized structures has been increasing explosively, reaching for more than 230 types [3]. New class of zeolites, such as crystalline aluminophosphates (AlPOs) [19,20], silico-aluminophosphates (SAPOs) [21,22], metalo-aluminophosphates (MeAPOs) [23], borosilicate zeolites [24,25], and germanosilicate zeolites [26,27] among others contributed the new findings of zeolite structures. Although a number of structures have been discovered in recent years, the commercialized zeolites are still limited with some zeolites (Y, mordenite, ZSM-5, ferrierite, beta, chabazite etc.) for the reason of costs, unique applications, and stability of materials.

1.2.2. Hydrothermal synthesis

Zeolites are generally synthesized by the hydrothermal reaction in basic media [28]. Silica source, alumina source, alkali source (mineralizer), water, and OSDA (if necessary) are mixed together and well homogenized. Seed crystals are sometimes added to promote the nucleation of the target zeolite. Then, the obtained hydrogel is heated under atmospheric pressure or in a Teflon-lined stainless steel autoclave at the reaction temperature of 80–200 °C under autogenous pressure, typically. Fumed silica, sodium silicate, silica sol, and tetraethylorthosilicate (TEOS) among others can be used as a silica source. As an alumina source, such as aluminium hydroxide, aluminium

sulphate, sodium aluminate, and aluminum isopropoxide are often used. Sodium hydroxide and potassium hydroxide are commonly used as an alkali source of the reaction. Hydroxide anion OH^- in the raw materials works as a mineralizer, promoting dissolution-precipitation process of silicates by hydrolysis [29]. OH^- can be replaced by fluoride anion F^-. Some new zeolites have been synthesized with F^- [30,31].

The crystallization process of zeolites is described as three parts, that is, induction period, nucleation, and crystal growth (Figure 1-3) [29]. The induction period is the most mysterious part of zeolite crystallization due to the difficulties of analysis with no crystalline phase. During induction period, the *primary amorphous phase*, consisting of non-equilibrium mixture of raw materials, is converted to the *secondary amorphous phase*. The secondary amorphous phase is a pseudo-steady-state intermediate, which has partly ordered structures, that is, more complex and larger polysilicates, called "secondary building units" (SBUs) [29]. SBUs are considered to be used as building blocks for the nucleation and growth of zeolite crystals (Figure 1-4) [32]. Supersaturation of the dissolved silicates is the driving force to promote nucleation and growth. The crystallization process would become faster and more efficient if the aforementioned building blocks are provided as raw materials. For example, Sano has been succeeded to synthesize various zeolites in facile routes using parent zeolites as only source of silica and alumina [33,34].

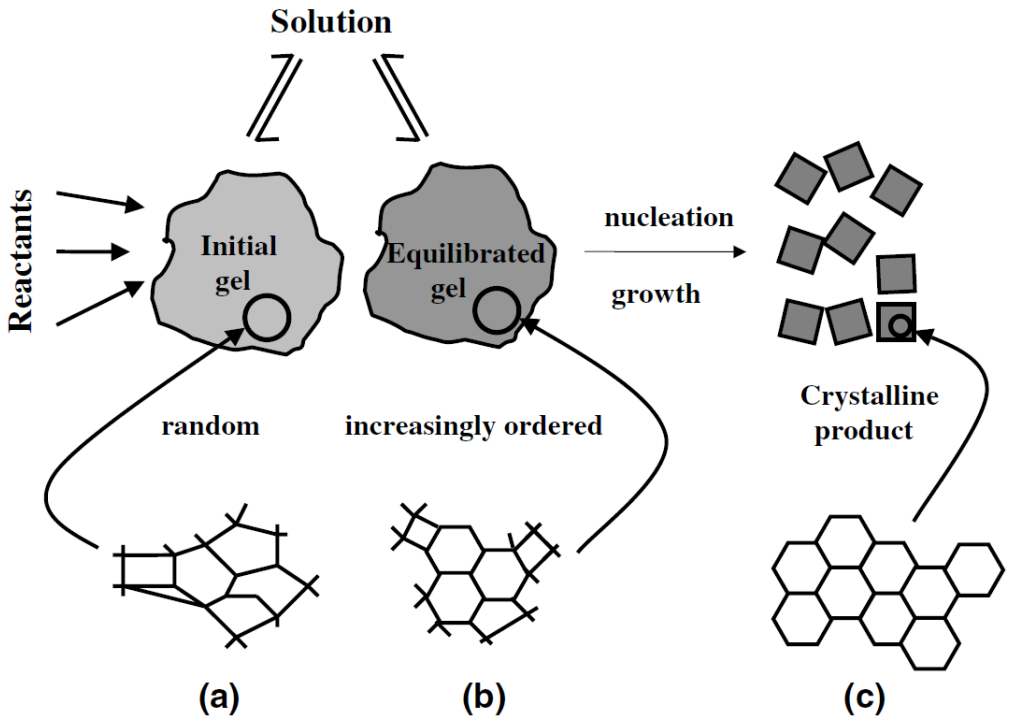

Figure 1-3 Scheme of zeolite crystallization. (a) Primary amorphous phase, (b) secondary amorphous phase, and (c) crystalline product [29].

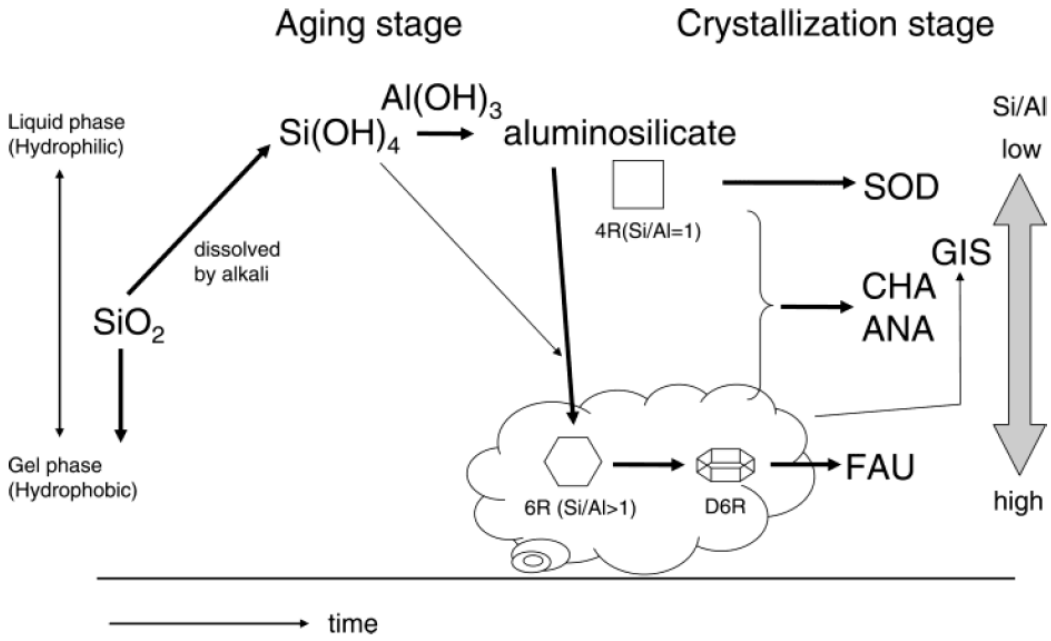

Figure 1-4 Illustration of the promotional effect of aging on the zeolites crystallization [32]. In this proposed mechanism, different phases are obtained from the gel containing corresponding SBUs.

1.2.3. Organic structure-directing agent (OSDA)

In the basic process of zeolite synthesis, alkali cations such as Na^+ and K^+ show structure-directing effect through modifying the amorphous aluminosilicate microstructure (Figure 1-4) and stabilizing zeolite framework as charge compensating cations. The OSDA, typically selected from the group of quaternary alkylammonium cations, works similarly as alkali cations above. However, because the OSDA is bulkier and more hydrophobic than alkali cations, it is able to stabilize less aluminium building blocks with low electrical density. This is why the OSDA is frequently used to synthesize high-silica zeolites [28,29].

Since Barrer first reported the use of tetramethylammonium cation as an OSDA [35], almost every kind of available molecules have been tested to synthesize novel zeolites. Then actually, lots of novel structures have been discovered with the help of OSDAs [17,18,36-38]. Along with the discoveries, the role of OSDA in zeolites synthesis process has been also studied. Moor and coworkers proposed that in the Si-tetrapropylammonium-MFI (Si-TPA-MFI) synthesis system, TPA interacts with soluble silicates, forming hydrophobic hydration spheres. Then, overlapped these spheres (primary units) aggregates and leads to the nucleation of MFI phase (Figure 1-5) [39].

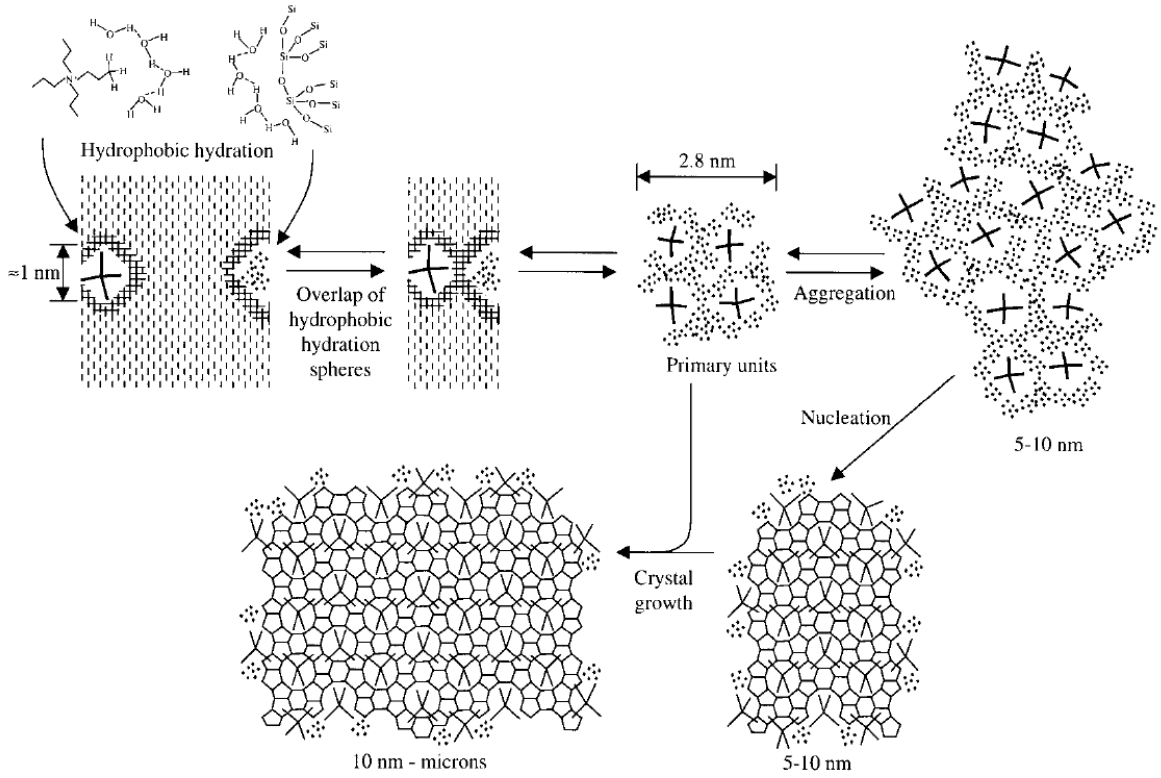

Figure 1-5 A scheme of the function of OSDA in the Si-TPA-MFI system [39].

1.2.4. Isomorphous substitution of trivalent metals in zeolites

Trivalent aluminium atoms in the framework of zeolites act as “acid sites” when protons exist as charge compensating cations. If the acid strength of zeolites is controllable by substituting aluminium atoms with other metals, it is expected to expand its applications in catalysis [40]. In addition to varying acid strength, detached metals from the framework, as isolated ions, clusters or particles, can be active sites for catalytic reactions. Kharitonov reported that the ferrisilicate analogs of ZSM-5 zeolite show good catalytic activity for one-step oxidation of benzene to phenol [41]. Isomorphous substitution of aluminosilicate zeolites has been investigated for the metals such as B, Fe, Ga, V, Zn, Cr, In, Ti, Sn, and Zr among others (see Table 1-3). Ti,

Sn, and Zr are tetravalent cations in the framework and therefore do not generate Brønsted acid sites.

Table 1-3 Examples of isomorphously substituted zeolites.

Metals	Structures	References
B	ZSM-5 (MFI)	42, 43
	ZSM-11 (MEL)	43
	Beta (*BEA)	44
	Mordenite (MOR)	45
	SSZ-33 (CON)	46
Fe	Beta (*BEA)	47
	ZSM-5 (MFI)	48,49
	Mordenite (MOR)	50
	Ferrierite (FER)	51
	Theta-1 (TON)	52
Ga	ZSM-5 (MFI))	42
	Beta (*BEA)	53
	Sodalite (SOD)	54
V	Beta (*BEA)	55
	ZSM-5 (MFI)	56
	ZSM-48 (*MRE)	57
Zn	VPI-7 (VSV)	58
	VPI-9 (VNI)	59
	CIT-6 (*BEA)	60
Cr	ZSM-5 (MFI)	61
In	Beta (*BEA)	62
Ti	TS-1 (MFI)	63
	TS-2 (MEL)	63
	Beta (*BEA)	63
Sn	Beta (*BEA)	64
Zr	Beta (*BEA)	65

Experimentally, isomorphously substituted zeolites (hereinafter also called "metallosilicate") are obtained by post-treatment or hydrothermal synthesis. An example of the post-treatment method is dealumination of the zeolites and following insertion of metals into the defect site [55]. The hydrothermal synthesis of metallosilicate is

basically the same as that of aluminosilicate zeolites. However, sometimes there are difficulties in synthesizing metallosilicates due to their stricter crystallization conditions, such as the use of fluoride and prolonged crystallization time [40,64]. This arises from that the metal ions used as raw materials often deposit in basic media as insoluble hydroxides. In addition, the ionic radii of the other metals (e.g. 0.067 nm for Fe^{3+}) are not as close to Si^{4+} (0.039 nm) as Al^{3+} (0.057 nm), leading to more distortions in the framework. Tetraethylorthosilicate (TEOS), silica sol or sodium silicate are often used as silica source to avoid generating the insoluble hydroxides by making them react with metal ions during raw materials mixing. Using F^- is also an effective way to synthesize metallosilicates [44,64].

1.2.5. Intergrowth (disordered) zeolites

The structure code of zeolite beta is *BEA, in which asterisk means the structure is disordered. The actual structure of beta is made of two similar but distinguished polymorphs named BEA and BEB (such structures are called "end-member structures"), inter-layered in one direction [66]. Figure 1-6 describes the structure of beta (*BEA), BEA, and BEB [66]. As shown for beta, intergrowth zeolites contain in their structure the "stacking disorder (fault)" and show no periodicity at least in one direction. Unlike the physical mixture of different zeolites, the channel system of each end-member structure in intergrowth zeolites is interconnected, forming one combined channel system. This is expected to exhibit a unique function in adsorption and catalysis use.

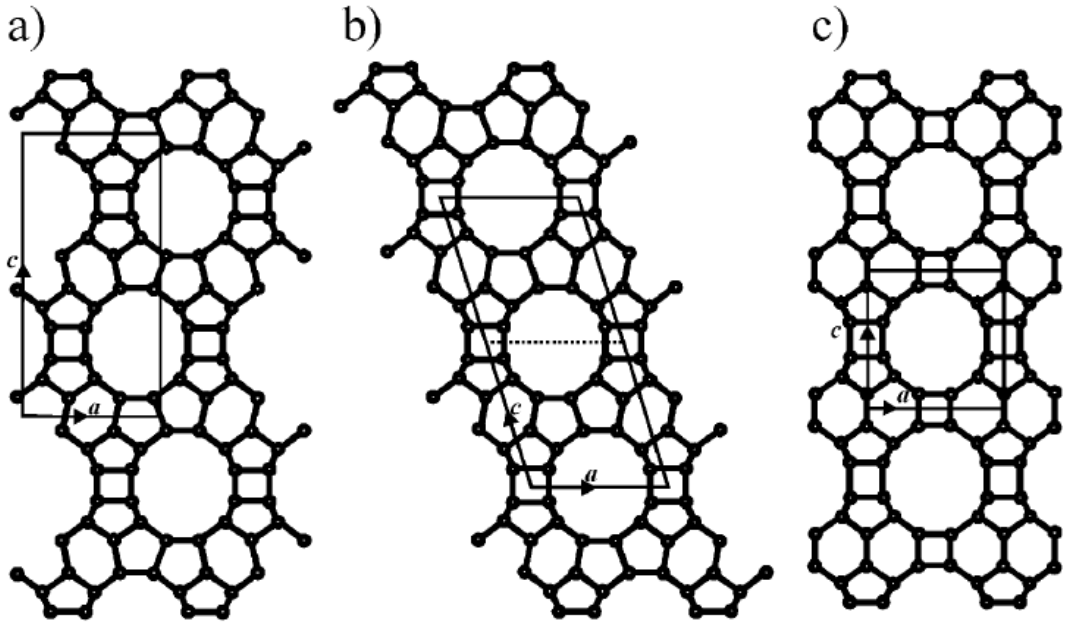

Figure 1-6 (010)-Projections of *BEA related end-members. (a) BEA (polymorph A), (b) BEB (polymorph B) [66]. (c) BEC (polymorph C) is not contained in *BEA structure.

In many cases intergrowth structures have been synthesized unintentionally, because the constituting end-member structures are similar and often crystallize under the same synthetic conditions. *BEA is a good example of it because *BEA is always obtained as an intergrowth zeolite. Under general synthetic conditions, the ratio of BEA and BEB phase is constant (A:B = 60:40). However, Corma et al. reported highly polymorph B enriched beta (A:B = 15:85) by controlling the kinetics of transformation from polymorph B to polymorph C [67]. Nobody has succeeded to synthesize pure BEA or BEB phase. On the contrary, to synthesize an intergrowth zeolite that has never been synthesized, it is necessary to identify the common synthesis condition for both end-member structures. If they are synthesized with different OSDAs, one promising

approach is using both OSDAs (dual-SDA synthesis). However, this is not as simple as it seems to be. The synthetic conditions other than OSDAs have to be overlapped for both structures. In addition, the structure-directing effect of the OSDAs should be independent from each other, not conflicting when interacting with the silicates. Cao et al. synthesized AFX/CHA intergrowth of silicoaluminophosphate by using N,N-dimethylcyclohexylamine and N,N,N',N'-tetramethyl-1,6-hexanediamine as OSDAs [68].

1.3. Characterization

Variety of analytical techniques are available to characterize basic properties, fine structure, OSDAs inside the pores and incorporated metals of zeolites. Some representative techniques and those used in this research are listed in Table 1-4. The most fundamental analyses to characterize zeolites are X-ray diffraction (XRD), scanning electron microscopy (SEM), and elemental analysis. N_2 adsorption is also a common method to evaluate the microporosity of zeolites through the analysis of adsorption-desorption isotherm.

Table 1-4 Analytical techniques of zeolites.

Techniques	**Abbreviation**	**Information obtained**
Powder X-ray diffraction	XRD (PXRD)	Crystalline phase, crystallite size, unit cell parameter
Scanning electron microcopy	SEM	Crystal morphology
Inductively-coupled plasma emission spectroscopy	ICP-AES	Elemental composition

N_2 adsorption	-	BET surface area, micropore volume, total pore volume, average pore diameter
Ammonia-temperature programmed desorption	NH_3-TPD	NH_3 adsorption capacity, amount of acid sites, acid strength
^{27}Al / ^{29}Si magic-angle spinning nuclear magnetic resonance	^{27}Al MAS NMR ^{29}Si MAS NMR	Coordination structure of Al and Si, distribution of Al site
Fourier transform infrared spectroscopy	FT-IR	Acid strength, silanols, catalyst characteristics (with probe molecules)
X-ray photoelectron spectroscopy	XPS	Surface elemental composition, chemical state, electronic state
Diffuse reflectance ultraviolet-visible absorption spectroscopy	Diffuse reflectance UV-Vis	Coordination structure of metal cations, quantification of metal cations with different polymerization degree (isolated, clusters, and particles)
Electron paramagnetic resonance	EPR	Environment symmetry of transition metal ions with unpaired electron
X-ray absorption fine structure spectroscopy	XAFS (XANES, EXAFS)	Electronic state, coordination structure of metal cations, distance to neighboring atoms, number of neighboring atoms
Electron diffraction	-	Symmetry of crystal
High-resolution transmission electron microscopy	HRTEM	Crystal structure, dislocations, grain boundaries
Solid-state ^{13}C dipolar decoupled magic-angle-spinning nuclear magnetic resonance	^{13}C DD/MAS NMR	Identification and quantification of organic molecules
Thermogravimetric and differential thermal analysis	TG/DTA	Amount and state of organic molecules in zeolites, silanols, thermal stability
CHN analysis	-	Elemental composition of organic molecules in zeolites

2. Zeolites for vehicle emission control

2.1. Worldwide diesel emissions standards

Any engines driven by fossil fuels generate pollutants when combusting fuels. Major pollutants from gasoline engines are nitrogen oxides (NO, NO_2, and N_2O, also

called NO_x), carbon monoxide (CO), and unburned hydrocarbons (HC). For diesel engines, soot, or particulate matter (PM) is added as pollutants. Since the development of the three-way catalyst [69], which reduces NO_x, CO, and HC with high efficiency in stoichiometric fuel gas, gasoline emissions have been relatively well-controlled. In contrast, there are inherent difficulties for diesel emission control, despite the diesel technology is gathering attentions for its better fuel economy. Diesel engines are normally operated under "lean" environment, in which the three-way catalyst cannot be used due to the excess of oxygen in the exhaust. For the NO_x and PM reduction, trade-off problem arises when it is to be controlled by engines only [70].

However, recent regulations for diesel emissions have been strictly tightened in many countries to minimize the negative impact on the environment and protect public health. North America, Europe, and Japan are at the leading position in this field, with the background that they have huge automotive industries with state-of-the-art technologies. China and India, which are both suffering from serious air pollution, are gathering much attention recently, because they are to introduce strict regulations comparable to those of the above leading regions. Figure 1-7 summarizes the current and future regulations for each region until 2025. In the most tightened regulations, emissions from diesel vehicles are required to be close or the same level as those from gasoline engines. Well-harmonized worldwide and real-emission based testing methods are also in discussions. To meet these regulations, various catalyst systems have been developed as shown in Figure 1-8 for example. Zeolites are mainly used for the abatement of NO_x, HC, and CO. PM is removed from the exhaust by filtration using

ceramics filter called DPF (Diesel Particulate Filter). To improve the system efficiency and minimize overall converter units, the combination of the SCR catalysts on DPF filter substrate has been investigated.

2.2. Diesel emission control technologies using zeolites

2.2.1. NOx

NO_x is a harmful component in emissions which causes smog, acid rain, and respiratory diseases and so on [71]. The amount of it increases when N_2 and O_2 containing fuel gas combusts at high temperature. For the abatement of NO_x, several techniques, that is, EGR (Exhaust Gas Recirculation), LNT (Lean NO_x Trap), and SCR (Selective Catalytic Reduction) are often used [70]. The SCR, also called Urea-SCR or NH_3-SCR, is a promising technique that utilizes NH_3 from the decomposition of urea as a reductant, showing superior NO_x conversion and N_2 selectivity in the wide range of temperature (e.g. 150–500 °C) [70]. The SCR is beneficial especially for low-temperature NO_x reduction; however, further reduction at lower temperature is strongly desired. One reason for that is that the cold-start NO_x (NO_x emitted during the engine/catalyst warming-up) should be reduced under the stricter regulations. Another reason is the improvement of fuel economy, which results in lower exhaust temperature [72].

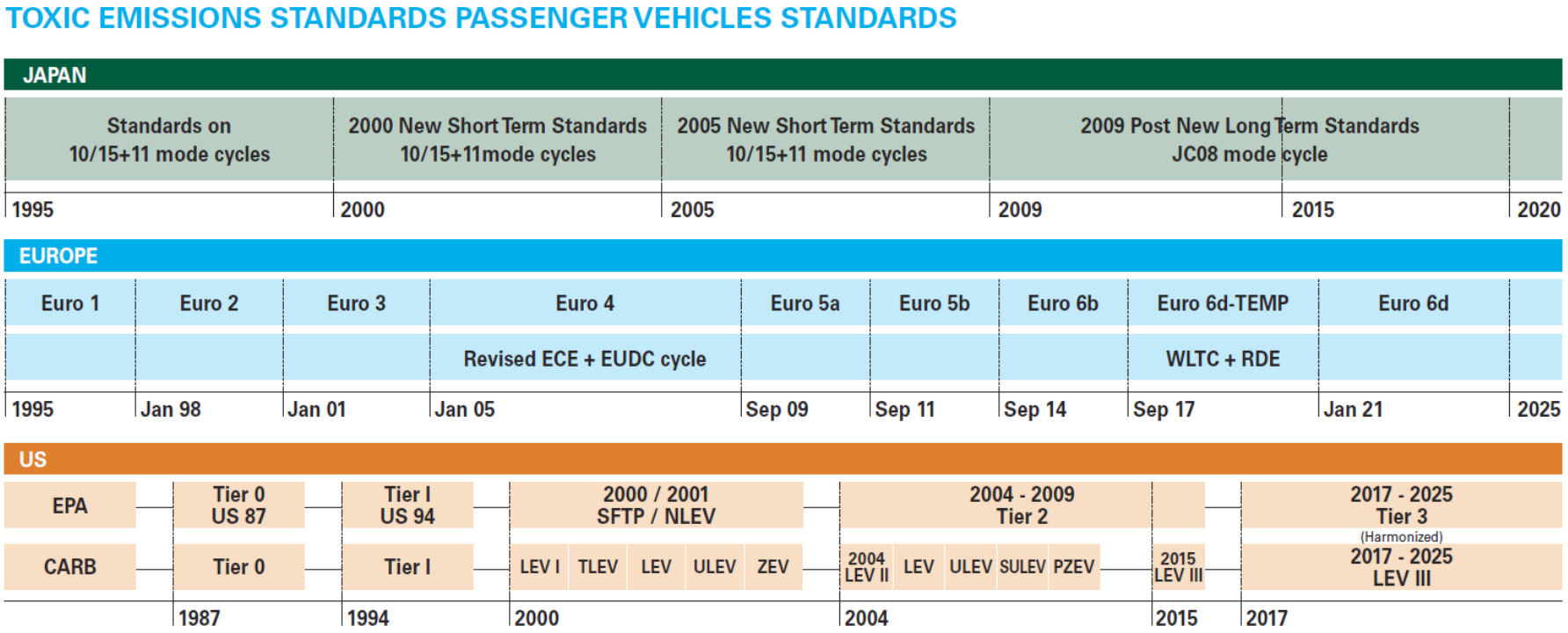

Figure 1-7 Emission standards in Japan, Europe, and the US (from DELPHI, 2016 | 2017 Worldwide Emissions Standards).

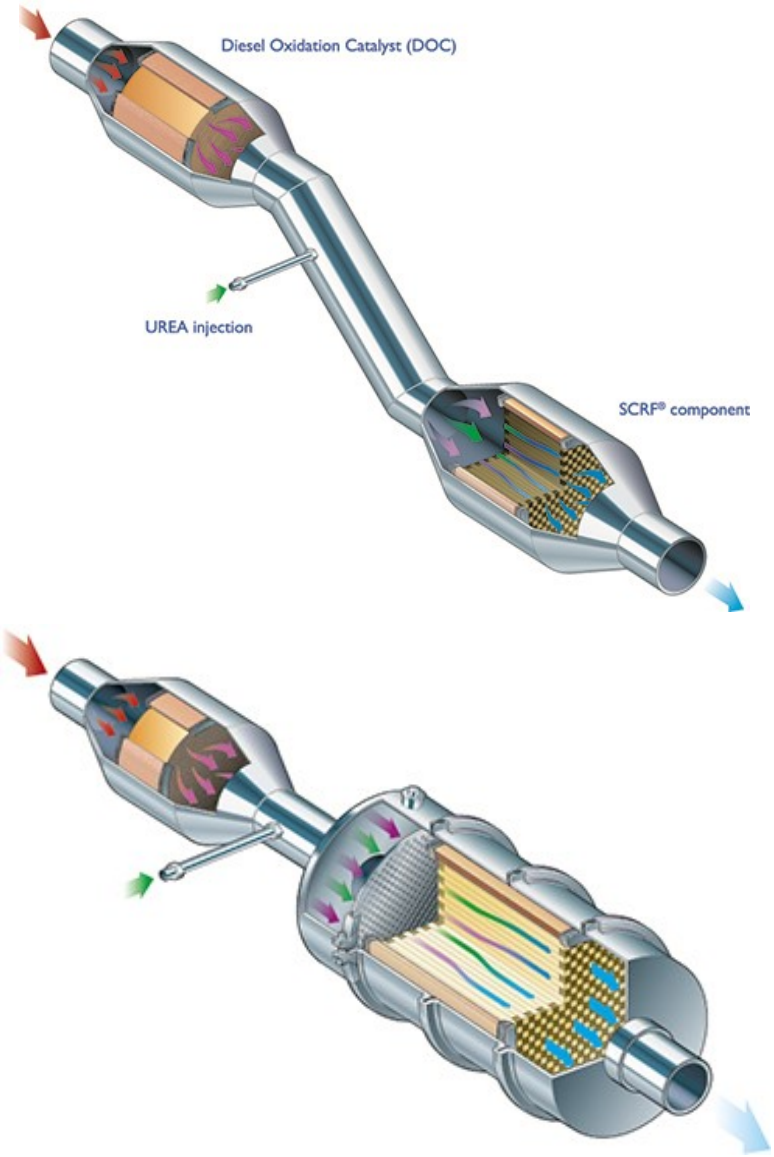

Figure 1-8 Examples of the catalytic system for (top) light-duty diesel and (bottom) heavy-duty diesel (from the website of Johnson Matthey). “SCRF” indicates the SCR catalyst on soot filter (DPF).

As catalysts for the SCR, vanadium-based catalysts have been commonly used especially for the stationary use such as power plants [73]. They can also be used for automobile catalysts, however, zeolite-based catalysts show much advantage for their greater low-temperature catalytic activity. Iron-exchanged beta and copper-exchanged SSZ-13 (CHA structure) are the well-known catalysts for the SCR [70]. Especially,

copper-exchanged CHA has attracted much attention and been intensively studied as promising catalyst due to its excellent catalytic activity, hydrothermal stability, and hydrocarbon-resistance [74-77]. CHA belongs to the structural group of "small-pore" zeolites, which contain 8MR pores as maximum openings. Lobo et al. proposed that these small-pores prevent Al atoms in the cages of CHA structure from migrating outside the cages, resulting in re-insertion of Al atoms into the framework at low temperature [78]. Copper ions are considered to be stabilized outside the plane of six-membered ring of CHA structure based on Rietveld refinements of synchrotron XRD (Figure 1-9) [79]. Other copper-exchanged small-pore zeolites, e.g. SSZ-16 (AFX) [79], SSZ-39 (AEI) [80], and LTA [81], have been also gathering attention for the reason that they are also expected to have the abovementioned microstructure (Figure 1-10). The reaction mechanism of the SCR of NO_x is complex [82], but simplified reactions are described as follows:

1) $4NO + 4NH_3 + O_2 \rightarrow 4N_2 + 6H_2O$ Slow

2) $NO + NO_2 + 2NH_3 \rightarrow 2N_2 + 3H_2O$ Very fast

The reaction proceeds without NO_2 in reaction 1), whereas equimolar amount of NO and NO_2 are involved in reaction 2). Because the kinetics of reaction 2) is very fast, controlling NO/NO_x ratio as it is close to 0.5 is important to achieve higher NO_x conversion at low-temperature. This is more the case for iron-exchanged zeolites due to the higher sensitivity of catalytic activity for the NO/NO_x ratio, compared to copper-exchanged zeolites [70]. In general, iron-exchanged zeolites are suitable for high-temperature SCR, however, its low-temperature catalytic activity can be improved

drastically by taking advantage of the reaction 2) by oxidizing a part of NO to NO_2 on oxidation catalysts.

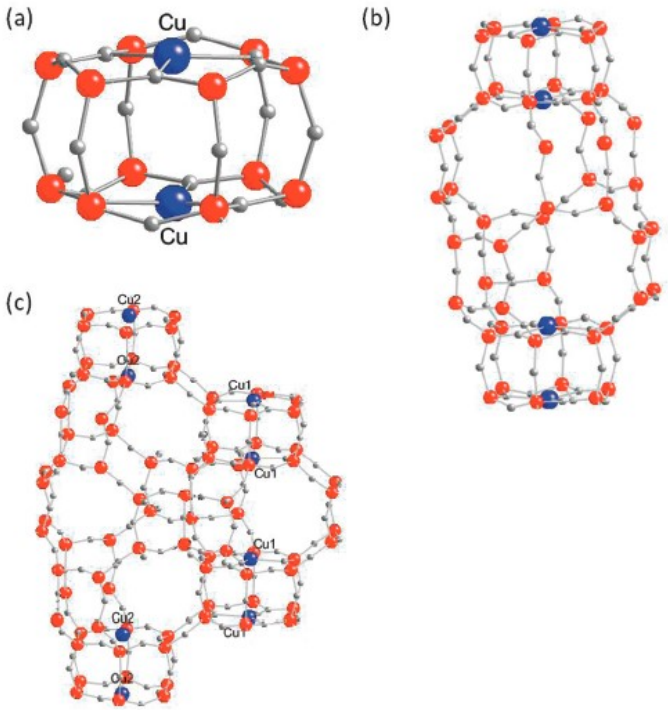

Figure 1-9 Location of copper ions in copper-exchanged SSZ-13 [76]: (a) side view, (b) entire cage, and (c) copper-exchanged SSZ-16.

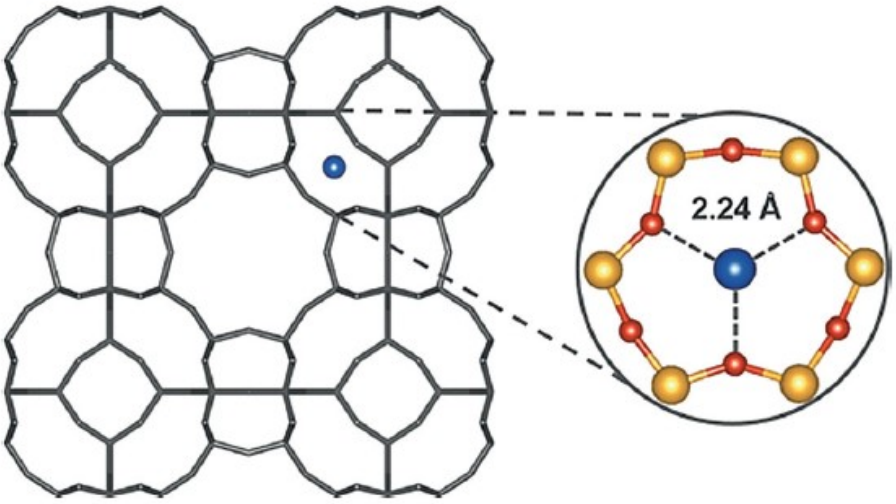

Figure 1-10 Location of copper ions in LTA structure [78].

2.2.2. HC and CO

HC emitted in the atmosphere is considered to be the cause for harmful smog by photochemical reaction with NO_x. CO is also known as highly toxic compound for humans. In diesel emissions, HC and CO are removed by DOC (Diesel Oxidation Catalyst), which typically consists of zeolites with platinum group metals loaded on a substrate [83]. The important function of zeolites here is the adsorption of hydrocarbons in the micropores to prevent HC slip during cold-start. DOC also converts NO to NO_2, improving the NO_x reduction on the SCR catalyst and helping PM oxidation on the DPF.

3. Objectives of the research

The overall objective of this research is to develop novel and highly-functional zeolites which are suitable for vehicle emission control. Zeolites for this application have been required to be stable in severe, hydrothermal conditions under which they are actually used. With the recent development of more complex and integrated exhaust systems, more hydrothermally stable zeolites are desired. At the same time, such zeolites are expected to show greater catalytic activity and/or characteristic adsorption-desorption properties in their applications based on their acidity, metal-promoted functions, unique micropore systems and so on.

In Chapters 2–4, I investigated the metal-promoted functions of zeolites (*BEA zeolite with iron) by the isomorphous substitution. Synthesized zeolites which contain iron atoms in the framework were evaluated mainly on the NH_3-SCR reaction. Their

material properties and the state of iron were characterized in detail by various analytical techniques. In Chapter 5, I tried to develop a novel intergrowth zeolite with AFX/CHA structures (ZTS-1 and ZTS-2) by dual-SDA approach. Other than the functional evaluation as SCR catalysts, the determination of the AFX/CHA ratio of ZTS-1 and ZTS-2 is also the major theme in this chapter.

References

[1] G. Leofanti, M. Padovan, G. Tozzola, and B. Venturelli, *Catal. Today* 41, 207 **(1998)**.

[2] A. Corma, F. Rey, S. Valencia, J.L. Jordá, and J. Rius, *Nat. Mater.* 2, 493 **(2003)**.

[3] http://www.iza-structure.org/

[4] J.A. Martens, M. Tielen, P.A. Jacobs, and J. Weitkamp, *Zeolites* 4, 98 **(1984)**.

[5] H. Nakamoto and H. Takahashi, *Zeolites* 2, 67 **(1982)**.

[6] R.W. Grose and E.M. Flanigen, *U S Pat.* 4,061,724 **(1985)**.

[7] L.S. Cheng and Y. Ralph T, *Chem. Eng. Sci.* 49, 2599 **(1994)**.

[8] M. Molina-Sabio, M.T. González, F. Rodriguez-Reinoso, and A. Sepúlveda-Escribano, *Carbon* 34, 505 **(1996)**.

[9] N.Y. Chen and W.E. Garwood, *J. Catal.* 52, 453 **(1978)**.

[10] F. Helfferich, *Ion Exchange*, Dover Publications, Inc. New York **(1962)**.

[11] J. Li, H. Chang, L. Ma, J. Hao, and R.T. Yang, *Catal. Today* 175, 147 **(2011)**.

[12] A. Corma, *J. Catal.* 216, 298 **(2003)**.

[13] R.L. Smith, C.D. Chang, and W.H. Lang, *J. Catal.* 56, 169 **(1979)**.

[14] H. de St Claire Deville, *Comptes Rendus Acad. Sci.*, 54, 324 **(1862)**.

[15] R.M. Barrer, *J. Chem. Soc.* 2158 **(1948)**.

[16] J.A. Rabo and M.W. Schoonover, *Appl. Catal. A Gen.* 222, 261 **(2001)**.

[17] R.J. Argauer and G.R. Landolt, *U S Pat.* 3,702,886 **(1972)**.

[18] R.L. Wadlinger, G.T. Kerr, and E.J. Rosinski, *U S Pat.* 3,308,069 **(1967)**.

[19] S.G. Hedge, P. Ratnasamy, L.M. Kustov, and V.B. Kazansky, *Zeolites* 8, 137 **(1988)**.

[20] A. Simmen, L.B. McCusker, C. Baerlocher, and W.M. Meier, *Zeolites* 11, 654 **(1991)**.

[21] B.M. Lok, C.A. Messina, R.L. Patton, R.T. Gajek, T.R. Cannan, and E.M. Flanigen, *J. Am. Chem. Soc.* 106, 6092 **(1984)**.

[22] S.T. Wilson, R.W. Broach, C.S. Blackwell, C. a Bateman, N.K. McGuire, and R.M. Kirchner, *Microporous Mesoporous Mater.* 28, 125 **(1999)**.

[23] J.M. Bennett and B.K. Marcus, *Stud. Surf. Sci. Catal.* 269 **(1988)**.

[24] S. Vortmann, B. Marler, H. Gies, and P. Daniels, *Microporous Mater.* 4, 111 **(1995)**.

[25] R. Simancas, J.L. Jordá, F. Rey, A. Corma, A. Cantín, I. Peral, and C. Popescu, *J. Am. Chem. Soc.* 136, 3342 **(2014)**.

[26] R. Castañeda, A. Corma, V. Fornés, F. Rey, and J. Rius, *J. Am. Chem. Soc.* 125, 7820 **(2003)**.

[27] A. Corma, F. Rey, S. Valencia, J.L. Jordá, and J. Rius, *Nat. Mater.* 2, 493 **(2003)**.

[28] H. Robson, *Verified Synthesis of Zeolitic Materials 2nd Revised Edition*, **(2001)**, ELSEVIER SCIENCE B.V., Amsterdam.

[29] C.S. Cundy and P.A. Cox, *Microporous Mesoporous Mater.* 82, 1 **(2005)**.

[30] A. Corma, M. Puche, F. Rey, G. Sankar, and S.J. Teat, *Angew. Chemie - Int. Ed.* 42, 1156 **(2003)**.

[31] A. Corma, M.J. Diaz-Cabanas, J.L. Jorda, F. Rey, G. Sastre, and K.G. Strohmaier, *J. Am. Chem. Soc.* 130, 16482 **(2008)**.

[32] M. Ogura, Y. Kawazu, H. Takahashi, and T. Okubo, *Chem. Mater.* 15, 2661 **(2003)**.

[33] M. Itakura, I. Goto, A. Takahashi, T. Fujitani, Y. Ide, M. Sadakane, and T. Sano, *Microporous Mesoporous Mater.* 144, 91 **(2011)**.

[34] T. Inoue, M. Itakura, H. Jon, Y. Oumi, A. Takahashi, T. Fujitani, and T. Sano, *Microporous Mesoporous Mater.* 122, 149 **(2009)**.

[35] R. Aiello and R.M. Barrer, *J. Chem. Soc. A Inorganic, Phys. Theor.* 1470 **(1970)**.

[36] B.M. Lok, T.R. Cannan, and C.A. Messina, *Zeolites* 3, 282 **(1983)**.

[37] P. Wagner, Y. Nakagawa, G.S. Lee, M.E. Davis, S. Elomari, R.C. Medrud, and S.I. Zones, *J. Am. Chem. Soc.* 122, 263 **(2000)**.

[38] A. Corma and M.E. Davis, *ChemPhysChem* 5, 304 **(2004)**.

[39] P.-P.E.A. de Moor, T.P.M. Beelen, B.U. Komanschek, L.W. Beck, P. Wagner, M.E. Davis, and R.A. van Santen, *Chem. - A Eur. J.* 5, 2083 **(1999)**.

[40] G. Bellussi and V. Fattore, *Stud. Surf. Sci. Catal.* 79 **(1991)**.

[41] A.S. Kharitonov, G.A. Sheveleva, G.I. Panov, V.I. Sobolev, Y.A. Paukshtis, and V.N. Romannikov, *Appl. Catal. A Gen.* 98, 33 **(1993)**.

[42] C.T.W. Chu and C.D. Chang, *J. Phys. Chem.* 89, 1569 **(1985)**.

[43] G. Coudurier, A. Auroux, J.C. Vedrine, R.D. Farlee, L. Abrams, and R.D. Shannon, *J. Catal.* 108, 1 **(1987)**.

[44] S. Kallus, J. Patarin, P. Caullet, and A.C. Faust, *Microporous Mater.* 10, 181 **(1997)**.

[45] T.R. Gaffney, R. Pierantozzi, and M.R. Seger, *Stud. Surf. Sci. Catal.* 374 **(1989)**.

[46] S.I. Zones and Y. Nakagawa, *Microporous Mater.* 2, 557 **(1994)**.

[47] R. Kumar, A. Thangaraj, R.N. Bhat, and P. Ratnasamy, *Zeolites* 10, 85 **(1990)**.

[48] A. Meagher, V. Nair, and R. Szostak, *Zeolites* 8, 3 **(1988)**.

[49] S. Bordiga, R. Buzzoni, F. Geobaldo, C. Lamberti, E. Giamello, A. Zecchina, G. Leofanti, G. Petrini, G. Tozzola, and G. Vlaic, *J. Catal.* 158, 486 **(1996)**.

[50] A.J. Chandwadkar, R.N. Bhat, and P. Ratnasamy, *Zeolites* 11, 42 **(1991)**.

[51] R.B. Borade and A. Clearfield, *Chem. Commun.* 11, 2267 **(1996)**.

[52] M. Asensi, A. Corma, A. Martínez, M. Derewinski, J. Krysciak, and S. Tamhankar, *Appl. Catal. A Gen.* 174, 163 **(1998)**.

[53] C. Prieto, T. Blasco, M. Camblor and J. Pérez-Pariente, *J. Mater. Chem.* 10, 1383 **(2000)**.

[54] K. Suzuki, Y. Kiyozumi, S. Shin, and S. Ueda, *Zeolites* 5, 11 **(1985)**.

[55] F. Tielens, M. Trejda, M. Ziolek, and S. Dzwigaj, *Catal. Today* 139, 221 **(2008)**.

[56] J. Kornatowski, B. Wichterlová, J. Jirkovský, E. Löffler and W. Pilz, *J. Chem. Soc., Faraday Trans.* 92, 1067 **(1996)**.

[57] A. Tuel and Y. Ben Taârit, *Zeolites* 14, 18 **(1994)**.

[58] M.J. Annen, M.E. Davis, J.B. Higgins, and J.L. Schlenker, *J. Chem. Soc. Chem. Commun.* 1175 **(1991)**.

[59] L.B. McCusker, R.W. Grosse-Kunstleve, C. Baerlocher, M. Yoshikawa, and M.E. Davis, *Microporous Mater.* 6, 295 **(1996)**.

[60] M. Dong, J. Wang, and Y. Sun, *Microporous Mesoporous Mater.* 43, 237 **(2001)**.

[61] T. Chapus, A. Tuel, Y.B. Taarit, and C. Naccache, *Zeolites* 14, 349 **(1994)**.

[62] M. Chatterjee, D. Bhattcharya, H. Hayashi, T. Ebina, Y. Onodera, T. Nagase, S. Sivasanker, and T. Iwasaki, *Microporous Mesoporous Mater.* 20, 87 **(1998)**.

[63] R. Murugavel and H.W. Roesky, *Angew. Chemie Int. Ed. English* 36, 477 **(1997)**.

[64] A. Corma, M.E. Domine, L. Nemeth, and S. Valencia, *J. Am. Chem. Soc.* 124, 3194 **(2002)**.

[65] Y. Zhu, G. Chuah, and S. Jaenicke, *J. Catal.* 227, 1 **(2004)**.

[66] B. Mihailova, V. Valtchev, S. Mintova, A.-C. Faust, N. Petkov, and T. Bein, *Phys. Chem. Chem. Phys.* 7, 2756 **(2005)**.

[67] A. Corma, M. Moliner, Á. Cantín, M.J. Díaz-Cabañas, J.L. Jordá, D. Zhang, J. Sun, K. Jansson, S. Hovmöller, and X. Zou, *Chem. Mater.* 20, 3218 **(2008)**.

[68] G. Cao and M.J. Shah, *U S Pat.* 7,906,099 **(2011)**.

[69] M. Shelef and G.W. Graham, *Catal. Rev.* 36, 433 **(1994)**.

[70] I. Nova and E. Tronconi, *Urea-SCR Technology for deNOx After Treatment of Diesel Exhausts*, Springer **(2014)**.

[71] United States Environmental Protection Agency, *NOx How nitrogen oxides affect the way we live and breathe*, U.S. EPA Washington, DC **(1998)**.

[72] D.K. Pappas, T. Boningari, P. Boolchand, and P.G. Smirniotis, *J. Catal.* 334, 1 **(2016)**.

[73] Y. Liu, Z. Liu, B. Mnichowicz, A. V. Harinath, H. Li, and B. Bahrami, *Chem. Eng. J.* 287, 680 **(2016)**.

[74] J.H. Kwak, R.G. Tonkyn, D.H. Kim, J. Szanyi, and C.H.F. Peden, *J. Catal*. 275, 187 **(2010)**.

[75] R. Nedyalkova, C. Montreuil, C. Lambert, and L. Olsson, *Top. Catal.* 56, 550 **(2013)**.

[76] F. Gao, J.H. Kwak, J. Szanyi, and C.H.F. Peden, *Top. Catal.* 56, 1441 **(2013)**.

[77] F. Liu, Y. Yu, and H. He, *Chem. Commun.* 50, 8445 **(2014)**.

[78] D.W. Fickel, E. D'Addio, J.A. Lauterbach, and R.F. Lobo, *Appl. Catal. B Environ.* 102, 441 **(2011)**.

[79] D.W. Fickel and R.F. Lobo, *J. Phys. Chem. C* 114, 1633 **(2010)**.

[80] M. Moliner, C. Franch, E. Palomares, M. Grill, and A. Corma, *Chem. Commun.* 48, 8264 **(2012)**.

[81] T. Ryu, N.H. Ahn, S. Seo, J. Cho, H. Kim, D. Jo, G.T. Park, P.S. Kim, C.H. Kim, E.L. Bruce, P.A. Wright, I.-S. Nam, and S.B. Hong, *Angew. Chemie Int. Ed.* 56, 3256 **(2017)**.

[82] B. Guan, R. Zhan, H. Lin, and Z. Huang, *Appl. Therm. Eng.* 66, 395 **(2014)**.

[83] K. Hauff, U. Tuttlies, G. Eigenberger, and U. Nieken, *Appl. Catal. B Environ.* 100, 10 **(2010)**.

Chapter 2

Synthesis of Fe-based BEA zeolites in fluoride media and their catalytic performance in the NH_3-SCR of NOx

1. Introduction

As the regulations concerning waste gases from various sources are getting stricter worldwide, there are increasing demands for improved efficiency in the removal of pollutants such as NOx, particulate matter, hydrocarbons, and CO. The selective catalytic reduction of NOx with ammonia (NH_3-SCR) is an effective technique for purifying exhaust gases from internal combustion engines [1-3]. This technique has been used in mainly stationary sources like power plants, wherein a V_2O_5-WO_3/TiO_2 catalyst is widely employed. However, this catalyst has exhibited poor thermal stability, low space velocity, and a narrow temperature window in diesel engine applications. Recently, NH_3-SCR systems with Fe- and Cu-based zeolite catalysts have been widely used to control automobile emissions because they have a wider temperature window and higher thermal stability than the vanadia catalyst systems [1,2]. Moreover, for NOx reduction under lean-burn conditions, excellent deNOx activity in the low-temperature range of 150 to 350 ºC as well as the operating temperature window is required.

Fe-based zeolites have been intensively studied as suitable catalysts for the NH_3-SCR because the active Fe component is less toxic than V [1,2.4-8]. Fe-based

zeolite catalysts can remove NOx effectively in the broad temperature range of 200-500 ºC, especially for equimolar amounts of NO and NO_2 ("fast" SCR). The Fe-based zeolite catalysts are prepared by several methods, such as liquid or solid ion-exchange, incipient wetness impregnation (IWI), chemical vapor deposition (CVD), and isomorphous substitution (direct hydrothermal synthesis) [9-12]. The liquid ion-exchange method is most commonly used and isolated metal ions are incorporated into zeolite pores without agglomeration. However, the extent of metal ion incorporation depends on the number of Al centers in the zeolite framework used. Although the IWI and CVD methods are also effective, and a Fe content higher than that incorporated by the ion-exchange method can be easily achieved, it is difficult to keep the incorporated Fe species isolated [11,13,14].

It is well known that the isomorphous substitution method is very effective for synthesizing zeolites with highly dispersed, tetrahedrally coordinated Fe in the framework [15,16], and this feature is expected to be useful for various catalytic reactions [17]. Many types of Fe-substituted zeolite frameworks have been reported so far, including MFI [16,17], BEA [15], MOR [18], FER [19], and TON [20] among others. In the field of deNOx catalysts, the Fe-MFI zeolite has been particularly investigated [9,10]. In contrast, although the Fe-based BEA zeolite is also widely recognized as an excellent catalyst for the NH_3-SCR [5,12,14,21], there are few reports on the catalytic performance of isomorphously substituted Fe-BEA zeolite. Frey et al. investigated the NH_3-SCR activities of several Fe-based zeolite catalysts, and concluded that the Fe-BEA zeolite had the lowest activity among all of Fe-based zeolite catalysts

evaluated [22]. However, the low catalytic activity appears to be due to the poor crystallinity of the prepared Fe-BEA zeolite, which suggests that the full potential of the Fe-BEA zeolite was not realized.

Here, I hydrothermally synthesized highly crystalline Fe-based BEA zeolites with various Si/Al and Si/Fe ratios to develop a novel catalyst with improved low-temperature activity in the NH_3-SCR reaction. The influence of the chemical composition of the Fe-based BEA zeolites was systematically investigated. Furthermore, the catalytic activity of the Fe-based BEA zeolites was compared with that of the conventional Fe-loaded zeolite prepared by IWI. As a result, I found that the low-temperature activity can be improved using the isomorphous substitution method. Also, the synthesized Al-free Fe-BEA zeolite exhibited excellent catalytic activity even after hydrothermal aging at 700 ºC for 20 h, indicating its high hydrothermal durability.

2. Experimental

2.1. Synthesis of Fe-based BEA zeolite

To synthesize Fe-based BEA zeolites with a wide range of Si/Al and Si/Fe ratios, fluoride anions were used as a mineralizer. In general, addition of fluoride anions to the starting hydrogel can broaden the range of zeolite chemical compositions obtained. Camblor et al. reported that even a pure silica beta can be synthesized in fluoride media [23]. Although Fe-based BEA zeolite can also be obtained in OH^- media, highly crystalline zeolites with sufficiently wide composition ranges cannot always be readily prepared [15,24-26]. In this study, Fe-based BEA zeolite was hydrothermally

synthesized according to the method reported by Pérez-Ramírez et al [27]. $Fe(NO_3)_3 \cdot 9H_2O$ and $Al(NO_3)_3 \cdot 9H_2O$ were added to an aqueous solution of tetraethylammonium hydroxide (35%TEAOH, Sachem) and stirred until the solids were completely dissolved. Then, tetraethylorthosilicate (TEOS, 98%, Kishida) was added to the solution, which was stirred at room temperature. After complete hydrolysis of TEOS, the ethanol generated was removed by evaporation. Finally, aqueous HF solution (47%, Hirota) was added to the solution dropwise, and then the resulting hydrogel was homogenized using a mortar. The molar composition of the hydrogel was SiO_2 : xAl_2O_3 : yFe_2O_3 : 0.61TEAOH : 0.50HF : $7.5H_2O$, where x and y varied independently (x: 0-0.0625, y: 0.0066-0.0286). The hydrogel was heated at 150 ºC under static conditions in a Teflon-sealed stainless-steel autoclave (80 mL). After the crystallization was complete, the crystalline solid of the Fe-based BEA zeolite was filtered, washed, and dried overnight at 110 ºC. The dried product was calcined in air at 600 ºC for 2 h to eliminate TEA cations in the zeolitic pores.

The conventional Fe-loaded beta zeolite, Fe/beta(Si/Al), was also prepared by incipient wetness impregnation. Commercial beta zeolites with Si/Al ratios of 19 and 250 (beta(19) and beta(250) from TOSOH Co.) were used as catalyst supports. First, an aqueous $Fe(NO_3)_3$ solution having volume equivalent to the micropore volume of the support zeolite was prepared. Then, the aqueous Fe solution was added to the zeolite, and the resulting powder was mixed homogeneously and dried overnight at 110 ºC. Finally, the sample was calcined in air at 500 ºC for 2 h. The amounts of Fe loaded were 3.4 and 3.0 wt% for Fe/beta(19) and Fe/beta(250), respectively.

2.2. Characterization

Powder X-ray diffraction patterns of the products were measured on a diffractometer (MXP-3, MAC Science, Japan) using Cu K_α radiation. The scanning range (2θ) was 3º-43º. Elemental analysis was carried out by ICP-AES (OPTIMA 3000 DV, Perkin Elmer). The morphology of the zeolite crystals was studied using a scanning electron microscope (SEM; JSM-6390LV, JEOL). Nitrogen adsorption isotherms were measured at -196 °C with a volumetric apparatus (BELSORP-max, MicrotracBEL Corp.). Samples (~0.05 g) were evacuated at 350 °C for 2 h prior to the measurement.

The acidic properties of the Fe-based BEA zeolites were measured by the temperature programmed desorption of ammonia (NH_3-TPD). Prior to measurements, the samples (0.100 g) were heated in a flow of He at 500 ºC for 1 h. NH_3 adsorption was conducted in a flow of 10% NH_3/He (60 mL/min) at 100 ºC for 30 min, followed by flushing with He to remove excess NH_3. The temperature was then gradually increased from 100 to 700 ºC in a flow of He (60 mL/min), ramping at 10 ºC/min, and the desorbed NH_3 was measured by a thermal conductivity detector. To eliminate interference from the dehydration of silanol groups on the crystal surfaces above 500 ºC, a blank measurement was performed separately in a flow of He and the desorption curve was subtracted from that observed in the NH_3 desorption process.

Ultraviolet-visible absorption spectra were recorded on a diffuse reflectance UV-Vis spectrometer (UV-Vis 3100, Shimadzu, Japan) in the range of 220–700 nm using $BaSO_4$ as a blank, and subjected to the Kubelka-Munk conversion.

2.3. Catalytic test

NH_3-SCR reaction was performed using a fixed-bed flow reactor under atmospheric pressure in the 150-500 ºC temperature range. The catalyst was pelletized, crushed, and sieved to 0.85-1.4 mm, and 1.5 mL of the sieved sample was placed in a quartz tube. The gas composition was 200 ppm NO, 200 ppm NH_3, 10 vol% O_2, 3 vol% H_2O, and the balance made up with N_2. The total flow rate was set to 1.5 L/h and the gas hourly space velocity (GHSV) was 60,000 h^{-1}. During the experiments, the temperature was reduced from 500 to 150 °C in steps of approximately 50 °C, and the NOx conversion was calculated as follows:

$$\text{NOx conversion (\%)} = \frac{NO_{in} - NO_{out} - NO_{2out}}{NO_{in}} \times 100$$

where NO_{in} represents the NO inlet concentration (200 ppm) and NO_{out} and NO_{2out} represent the NO and NO_2 outlet concentrations, respectively. In order to assess the long-term hydrothermal durability of the catalyst, I investigated the catalytic performance after hydrothermal treatment at 700 °C for 20 h in a flowing gas containing 10 vol% H_2O and 90 vol% air with a GHSV of 6,000 h^{-1} (300 mL/min flow, 3 mL catalyst). To evaluate the steady state catalytic activity, the concentrations of NH_3, NO, and NO_2 in the outlet gas after 10 min of time-on-stream at each reaction temperature were analyzed by an FT-IR spectrometer (FT/IR-6100, JASCO, Japan) equipped with a gas cell (LPC-12M-S, 12m) and a mercury cadmium telluride detector cooled by liquid nitrogen. The concentrations were determined by the intensities of the peaks at 1033, 1875, and 2917 cm^{-1} for NH_3, NO, and NO_2, respectively. Thirty scans were averaged

for each normalized spectrum.

3. Results and discussion

3.1. Synthesis and characterization of Fe-based BEA zeolite

Table 2-1 lists the hydrothermal synthesis conditions and characteristics of Fe-based BEA zeolites (Al,Fe-BEA and Al-free Fe-BEA) with various Si/Al and Si/Fe ratios. Although the time for complete crystallization was dependent on the chemical composition of the starting hydrogel, highly crystalline BEA type zeolites could be obtained within 2 weeks. The as-prepared Al,Fe-BEA and Al-free Fe-BEA zeolites were white in color, suggesting that the Fe present in the BEA zeolite is incorporated into the framework structure. However, Al,Fe-BEA and Al-free Fe-BEA zeolites with higher Fe contents turned light brown after calcination, indicating that some of the Fe present detached from the framework and formed iron oxide species.

Table 2-1

Synthesis conditions and characteristics of Fe-based BEA zeolites.

Sample	Synthesis conditions[a]				Product (Fe-BEA)					
	Si/Al	Si/Fe	Si/(Al + Fe)	Reaction time [d]	Si/Al[b]	Si/Fe[b]	Si/(Al + Fe)[b]	Fe [wt%][b]	BET surface area [m^2/g][c]	Micropore volume [cm^3/g][d]
1	16	90	13.6	13.5	17	84	14.1	1.0	540	0.25
2	16	152	14.5	10.0	15	140	13.9	0.6		
3	20	44	13.8	10.5	19	40	13.0	2.2	510	0.24
4	20	88	16.3	10.5	21	83	16.6	1.1		
5	20	152	17.7	6.5	19	138	16.6	0.6		
6	36	35	17.8	10.5	36	33	17.2	2.7	470	0.23
7	36	44	19.8	10.5	36	41	19.2	2.1	470	0.22
8	36	74	24.3	10.5	35	69	23.4	1.3		
9	36	152	29.1	11.5	35	140	27.7	0.6		
10	-	44	-	10.0	2400	31	30.7	2.9	480	0.22

[a]H_2O/SiO_2 = 7.5, $TEAOH/SiO_2$ = 0.61, HF/SiO_2 = 0.50, Temperature = 150 ºC, Static conditions.

[b]Measured by ICP.

[c]Calculated by the BET method.

[d]Calculated by the t-plot method.

The representative XRD patterns of as-prepared Fe-BEA zeolites (samples 1, 3, 7 and 10) are displayed in Figure 2-1. The XRD patterns of all samples show the typical diffraction patterns of BEA zeolites containing no impurities from a co-crystallized phase. The lattice spacing calculated from the main peak (2θ = 22.46 º) of sample 7 (Si/Al = 36, Si/Fe = 41, Si/(Al+Fe) = 19.2) was 0.396 nm, while that of the commercial beta (Si/Al = 19) used in this study was 0.393 nm. Given the ionic radii of Si^{4+} (0.039 nm), Al^{3+} (0.057 nm), and Fe^{3+} (0.067 nm), incorporation of Fe into the framework clearly expands the lattice spacing in BEA zeolites. Figure 2-2 shows the SEM images

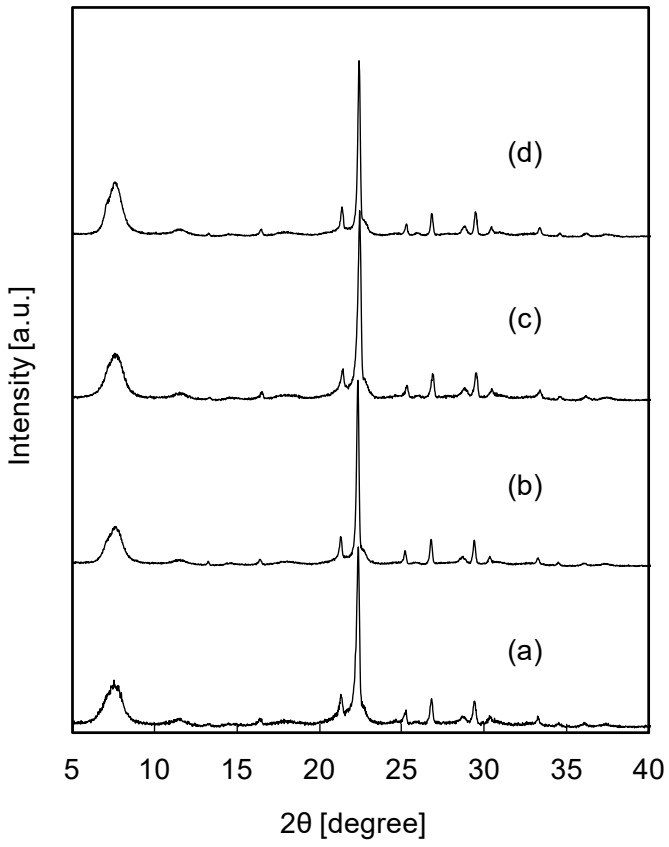

Figure 2-1 XRD patterns of as-prepared Al,Fe-BEA and Al-free Fe-BEA zeolites. (a) sample 1, (b) sample 3, (c) sample 7 and (d) sample 10.

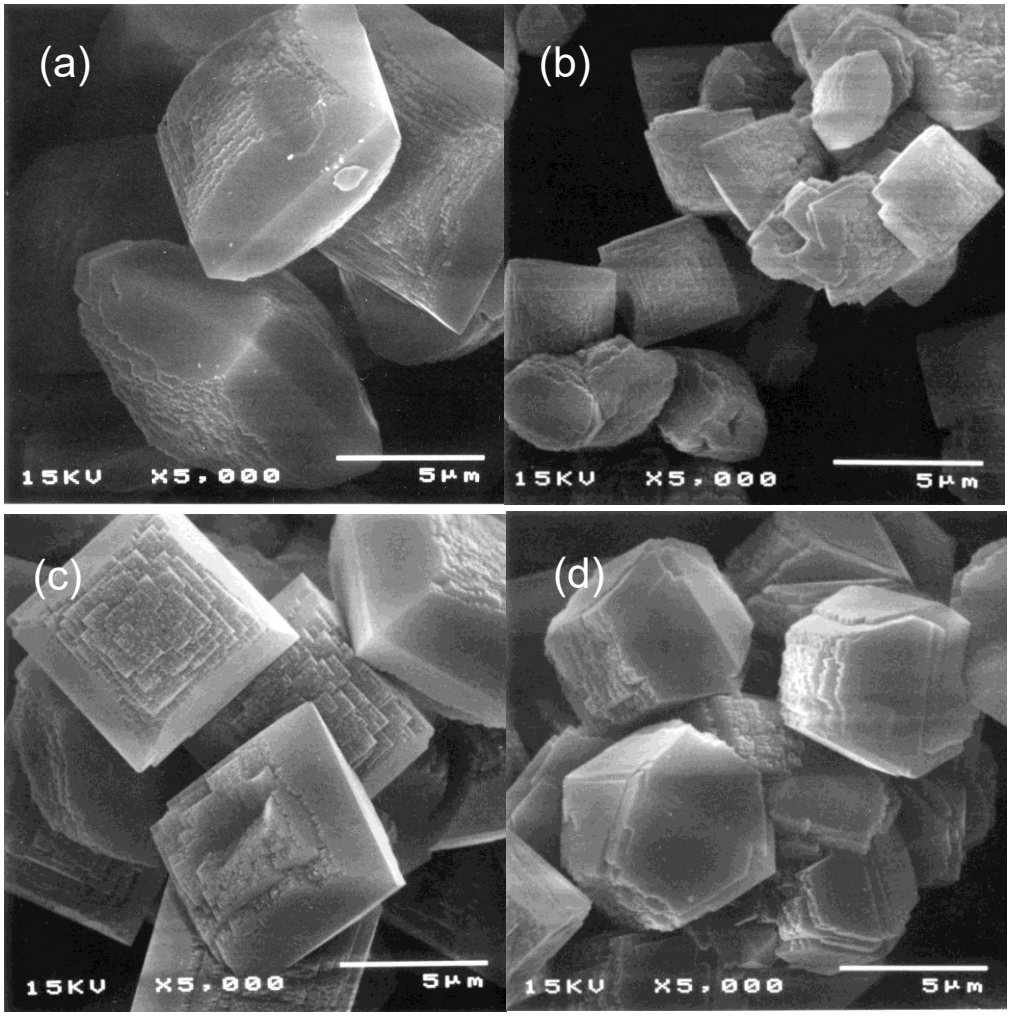

Figure 2-2 SEM images of as-prepared Al,Fe-BEA and Al-free Fe-BEA zeolites. (a) sample 1, (b) sample 3, (c) sample 7 and (d) sample 10.

of these zeolites, revealing large crystals with truncated square bipyramidal morphology. This is typical of beta zeolites crystallized from fluoride media [28], and fewer defects are present when they are synthesized in this manner.

The chemical compositions of as-prepared Fe-based BEA zeolites are summarized in Table 2-1. The Si/Al and Si/Fe ratios were almost the same as those of the starting hydrogels. Figure 2-3 shows the number of Fe atom per unit cell in as-prepared samples plotted against the number of Al atom. For the Al,Fe-BEA zeolite with a Si/Al ratio of

ca. 35 (approximately 1.7 Al atom per unit cell), the number of Fe atom per unit cell could be varied from 0.4 to 1.8. However, I have not succeeded in simultaneously incorporating large amounts of both Al and Fe atoms (e.g. 4.0 Al/u.c. and 1.5 Fe/u.c.) at present.

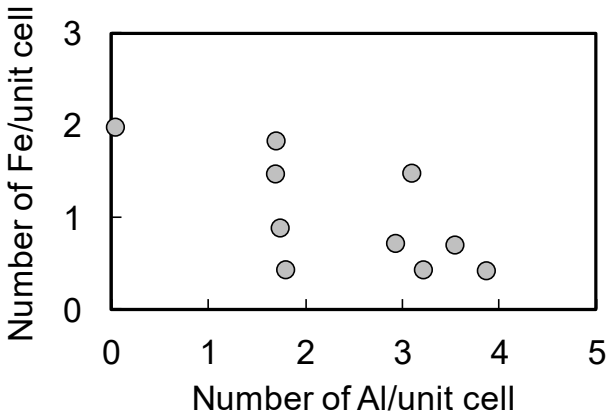

Figure 2-3 Numbers of Al and Fe atoms per unit cell of Al,Fe-BEA and Al-free Fe-BEA.

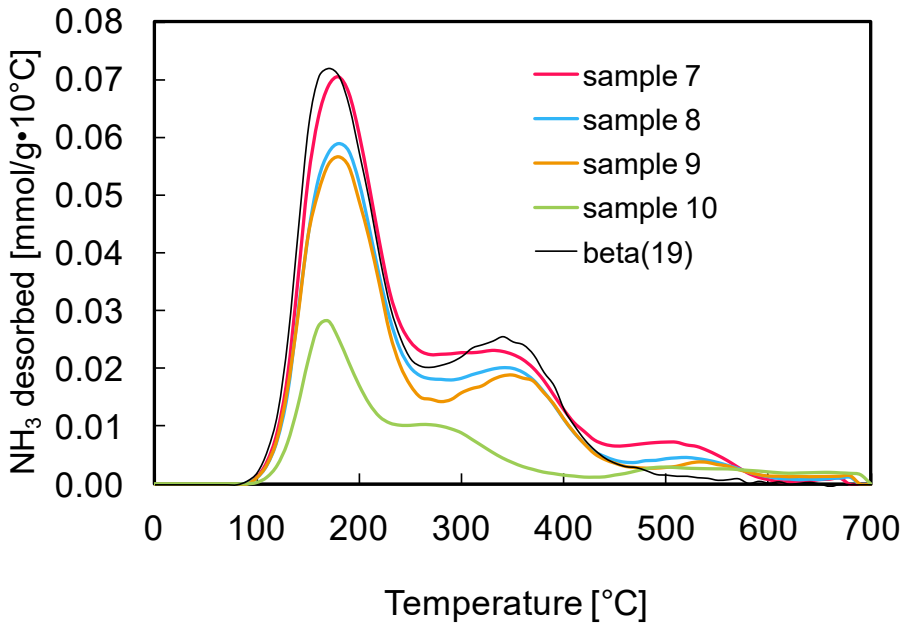

Figure 2-4 NH_3-TPD profiles of various Fe-based BEA zeolites and the conventional beta(19).

Figure 2-4 shows the NH_3-TPD curves of Fe-based BEA zeolites (samples

7-10) and commercial beta(19). Samples 7-9 have Si/Al ratios of ca. 35 but different Si/Fe ratios (41 for the sample 7, 69 for the sample 8, and 140 for the sample 9). The NH_3-TPD curve of the beta(19) showed two distinct peaks, viz. l-peak (ca. 190 ºC) and h-peak (ca. 360 ºC), which reflect the strength of NH_3 adsorption on acidic zeolite sites. Physisorbed NH_3 inside micropores desorbs at low temperature, giving the l-peak. In general, the h-peak is attributed to NH_3 desorbed from Brønsted acid sites [27]. As there are various kinds of acid sites in zeolites with different acid strengths, the h-peak position changes depending on the sites involved. Multiple h-peaks are observed in some cases [14]. The Al-free Fe-BEA zeolite (sample 10) also had two peaks, and the h-peak was shifted to a lower temperature (ca. 280 ºC) compared to beta(19). This probably means that sample 10 has weaker Brønsted acid sites caused by Fe in the framework. In the case of Al,Fe-BEA zeolites (samples 7-9), the amount of desorbed NH_3 increased with increasing Fe content. Based on the h-peak position for sample 10, the increase in the amount of desorbed NH_3 for samples 7-9 indicates the formation of highly crystalline Fe-based Brønsted acid sites. This suggests simultaneous incorporation of Al ad Fe atoms into the zeolite framework. A small peak was also observed around 500 ºC for samples 7-9. It is known that AlO^+ and $Al(OH)_2^+$ species generated by dealumination treatment act as Lewis acid sites [29]. Given that the intensity of the peak around 500 ºC for beta(19) is lower than that for the Al-free Fe-BEA zeolite (sample 10), the corresponding peaks for samples 7-9 seem to be due to NH_3 desorbing from the Lewis acid sites of extra-framework Fe species.

The amounts of NH_3 desorbed from various Fe-BEA zeolites are summarized

in Table 2-2. The NH_3 desorption in the temperature range from 220 to 700 °C was regarded as the h-peak. The amount of desorbed NH_3 for sample 7, with a Si/(Al + Fe) ratio of 19.2, was 0.57 mmol/g, which was larger than the 0.49 mmol/g found for beta(19) with Si/Al ratio of 19.0. If all of the Al or Fe atoms present in the zeolite are incorporated into the framework, the numbers of acid sites calculated from the framework compositions for the sample 7 and the beta(19) are 0.83 mmol/g and 0.84 mmol/g, respectively. Therefore, it is clear that some Al or Fe atoms are detached from the framework. From their NH_3 desorption profiles, it seems that the difference in the amount of NH_3 desorption between both samples is mainly due to the NH_3 desorption above 450 °C (0.09 mmol/g for the sample 7). This suggests that the detached Fe atoms in the sample 7 are present in the zeolitic pores as the Lewis acid FeO^+, whereas complete removal of Al from the framework hardly occurs in the beta(19), resulting in no formation of Lewis acid AlO^+. In the case of sample 10, the amount of desorbed NH_3 (0.19 mmol/g) was considerably smaller than expected from the Si/Fe ratio, indicating the formation of extra-framework Fe species. The Brunauer–Emmett–Teller (BET) surface area, and the micropore volume (calculated from the N_2 adsorption measurement), of the sample 10 were 480 m^2/g and 0.22 cm^3/g, respectively, almost the same as for other samples measured (Table 2-1). The small amount of desorbed NH_3 of the sample 10 is thus not due to its crystallinity. The sample 10 exhibited a smaller peak for temperatures over 450 °C compared to the sample 7, even though the amount of Fe in the sample 10 is slightly higher. This strongly indicates that the extra-framework Fe species in the sample 10 do not contribute to the formation of Lewis acid sites and the

chemical state is somewhat different. As shown in Figure 2-5(a), in the UV-Vis spectrum of the sample 10 the strong absorption was observed below 300 nm, indicating most part of the Fe species is present as isolated Fe^{3+} [27].

Table 2-2
Amounts of NH_3 desorbed from Fe-based BEA zeolites with various Si/Fe ratios, evaluated by NH_3-TPD.

Sample[a]	Si/Fe ratio (Fe wt%)	Si/(Al+Fe) ratio	Amount of NH_3 desorbed [mmol/g][b]
7	41 (2.1)	19.2	0.57
8	69 (1.3)	23.4	0.47
9	140 (0.6)	27.7	0.42
10	31 (2.9)	30.7	0.19
beta(19)	-	19.0	0.49

[a]Si/Al ratios of samples 7, 8 and 9 are 35 – 36 (see Table 2-1)
[b]Amount of NH_3 desorbed at the temperature range of 220-700 °C.

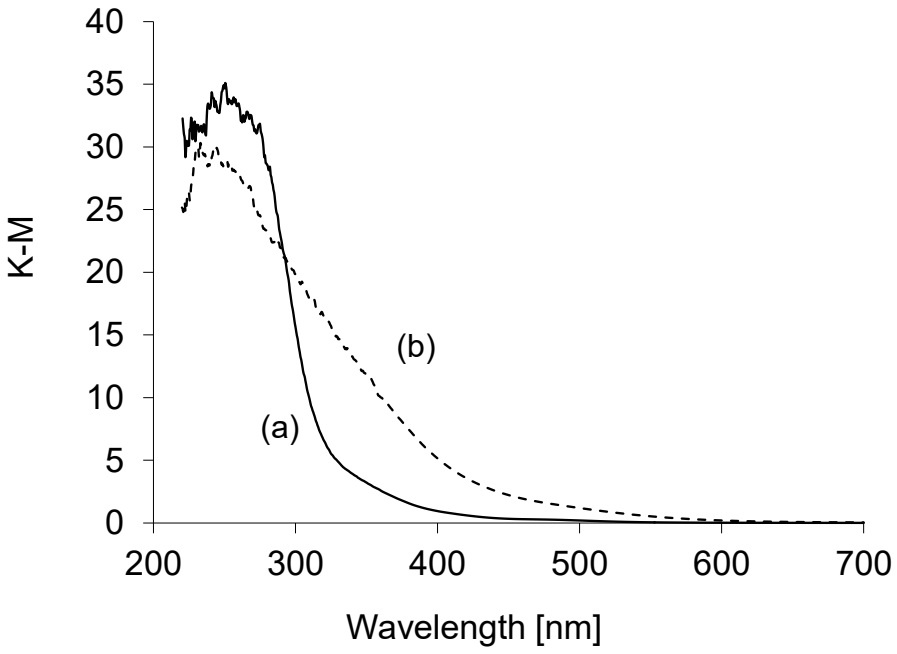

Figure 2-5 Diffuse reflectance UV-Vis spectra of Al-free Fe-BEA zeolites (sample 10) before and after hydrothermal treatment at 700 ºC for 20 h. (a) before hydrothermal treatment (b) after hydrothermal treatment

3.2. Catalytic test

Figure 2-6 shows the relationship between the reaction temperature and NOx conversion for the Al,Fe-BEA zeolite (Si/Al ratio = 21; Fe 1.1wt% (sample 4)) and the Fe/beta(19) (Si/Al ratio = 19; Fe 3.4 wt%), before and after hydrothermal treatment at 700 °C for 20 h. The fresh Al,Fe-BEA zeolite exhibited higher NOx conversion in the low to middle temperature range (200-300 ºC) compared to the Fe/beta(19), despite having one third of the Fe content. The NOx conversion at 200 ºC for the Al,Fe-BEA was 74%, but 48% for the Fe/beta(19). Although the NOx conversion was reduced by the hydrothermal treatment at 700 ºC for 20 h, higher NOx conversion was still observed for the Al,Fe-BEA zeolite. I have now rationalized the difference in the catalytic performance as follows. The presence of highly dispersed Fe species contributes to excellent catalytic performance in the low to middle temperature range. Such Fe species are mainly generated by the isomorphous substitution method. In contrast, the Fe/beta(19) showed better catalytic performance in the high-temperature range (400-500 ºC). This is probably due to the formation of agglomerated Fe species, which are considered to be active in NH_3-SCR at high-temperatures [30]. It is also likely that the Al,Fe-BEA have less agglomerated Fe species compared to the Fe/beta(19), even though the NH_3-TPD results suggest that there are some extra-framework Fe species in the Al,Fe-BEA zeolite.

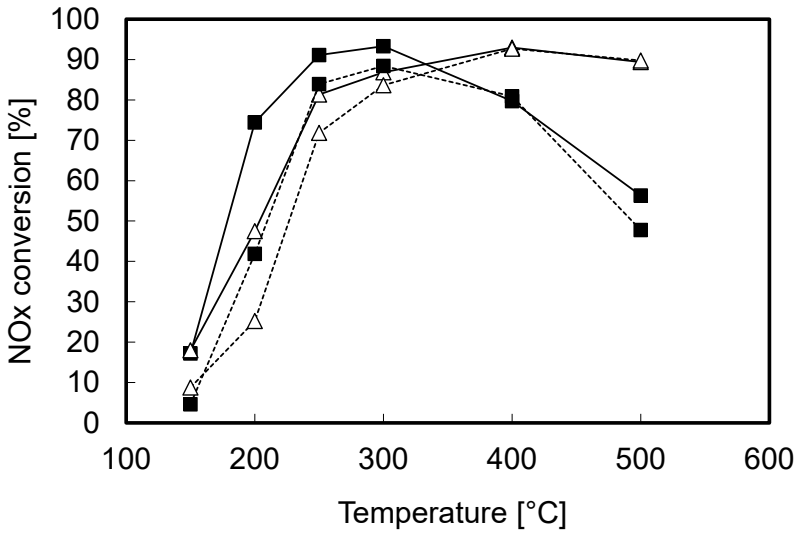

Figure 2-6 Conversion of NOx over (■) Al,Fe-BEA(sample 4) and (△) Fe/beta(19) before and after hydrothermal treatment at 700 ºC for 20 h. Solid line, fresh (before hydrothermal treatment); dotted line, after hydrothermal treatment.

To clarify the effect of the Si/Fe ratio on the NH_3-SCR activity, the catalytic performance of Al,Fe-BEA zeolites with various Si/Fe ratios was investigated. The Si/Al ratio of all these zeolites was approximately 35. Figure 2-7 illustrates the NOx conversion before and after hydrothermal aging at 700 ºC for 20 h. For fresh catalysts, before hydrothermal treatment, the NOx conversion in the low-temperature range (150-200 ºC) increased with an increase in the Fe content, or a decrease in the Si/Fe ratio. This suggests that a highly dispersed and isolated Fe species increases the low-temperature activity of NH_3-SCR. The role of Fe species has been discussed in many previous reports concerning NH_3-SCR over conventional Fe ion-exchanged zeolite catalysts [1,2.4-8]. The Fe species contributes to the oxidation of NO to NO_2, which is the rate-determining step of the NH_3-SCR reaction [4,21,31]. Although the NOx conversions decreased for all zeolites after hydrothermal treatment, the zeolites with higher Fe content demonstrated higher NOx conversion.

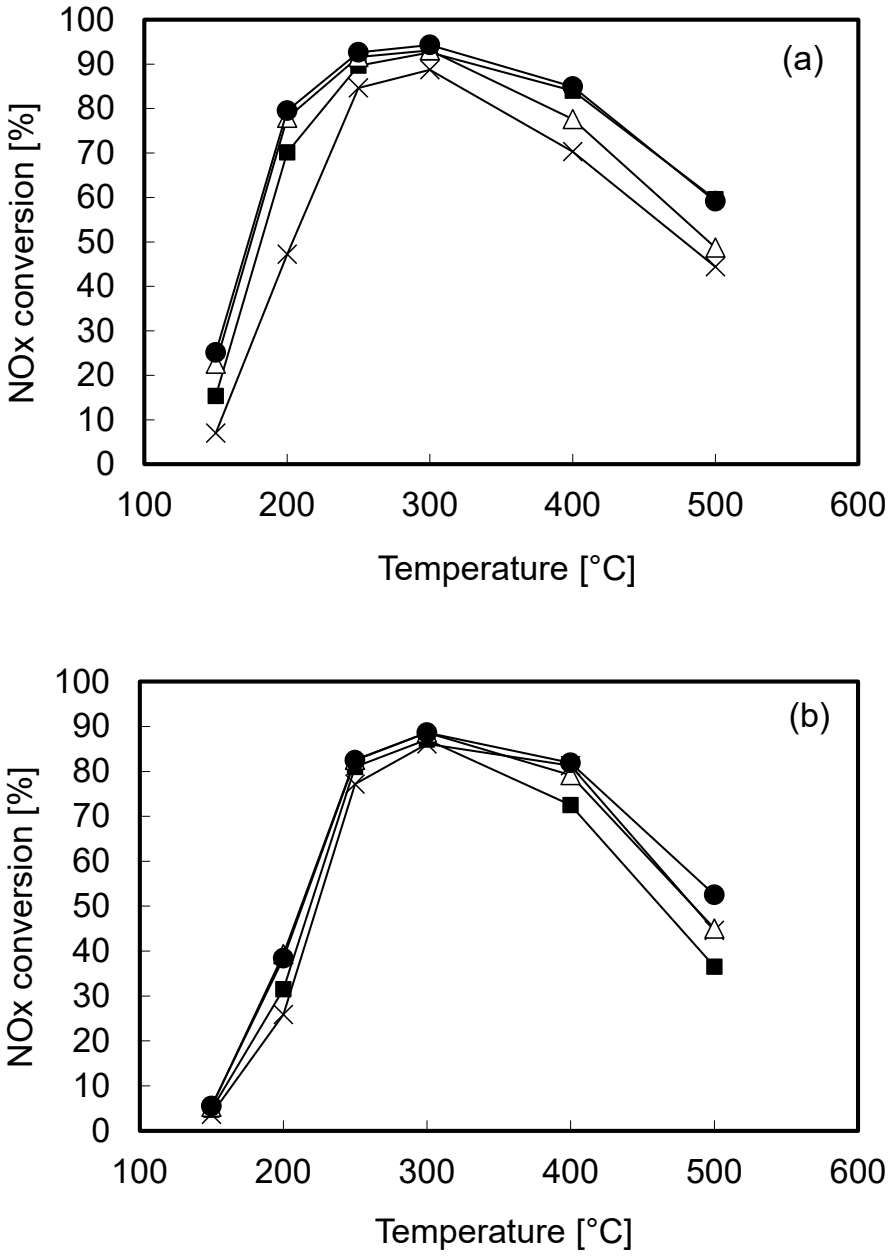

Figure 2-7 Conversion of NOx over Al,Fe-BEA zeolites with various Si/Fe ratios (a) before and (b) after hydrothermal treatment at 700 ºC for 20 h. ● sample 6 (Si/Fe = 33), ∆ sample 7 (Si/Fe = 41), ■ sample 8 (Si/Fe = 69), × sample 9 (Si/Fe = 140).

The effect of the Si/Al ratio on NOx conversion was also investigated. In Figure 2-8 the NOx conversions over the Al,Fe-BEA zeolites with Si/Fe ratios of 69-84 (samples 1, 4, and 8) are displayed against the reaction temperature. Figure 2-9 shows

the corresponding results for zeolites with greater amounts of Fe, i.e. Si/Fe ratios of 31-33, (samples 6 and 10). A similar trend is observed in both Figures. For fresh zeolites, the NOx conversion in the low-temperature range increased with increasing Al content, or acidity. Brandenberger et al. reported that Brønsted acidity has no significant effect on NH_3-SCR activity [32]. Shwan et al. also showed that little change in NH_3-SCR activity was observed even by a 40% decrease in NH_3 storage capacity [33]. The effect of the Si/Al ratio observed in my study may be explained thus. An increase in the number of framework Al atoms enhances the anchoring of Fe species by ion-exchange. When extra-framework Fe species are formed by a thermal/hydrothermal treatment, this prevents the Fe species from agglomerating. Among all fresh zeolites, the Al,Fe-BEA zeolite with the highest Al content (sample 1, Si/Al = 17) exhibited the best catalytic activity over the temperature range studied. However, the activity dropped drastically after hydrothermal treatment. As the relative crystallinities of the zeolites after hydrothermal treatment, evaluated by XRD, were 92% for sample 1, 89% for the sample 4, and 96% for the sample 9, structural collapse would not seem to be the main reason for the large reduction in activity after hydrothermal treatment. It may be due to severe dealumination, resulting in agglomeration of the extra-framework Fe species anchored on the framework Al sites by ion-exchange. It is known that the dealumination rate is dependent upon the amount of framework Al [34].

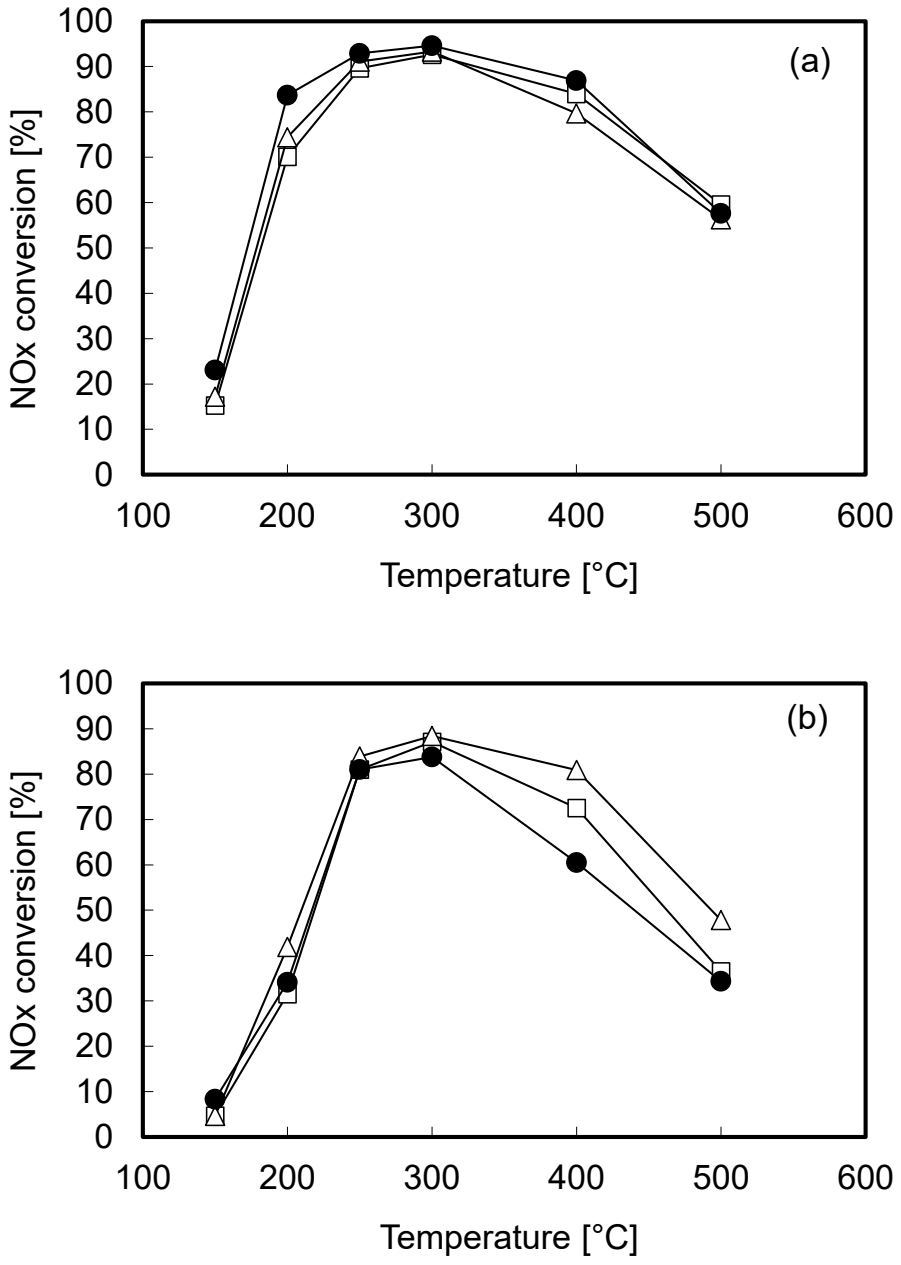

Figure 2-8 Conversion of NOx over Al,Fe-BEA zeolites with various Si/Al ratios (a) before and (b) after hydrothermal treatment at 700 ºC for 20 h. ● sample 1(Si/Al = 17), ∆ sample 4 (Si/Al = 21), □ sample 8 (Si/Al = 35)

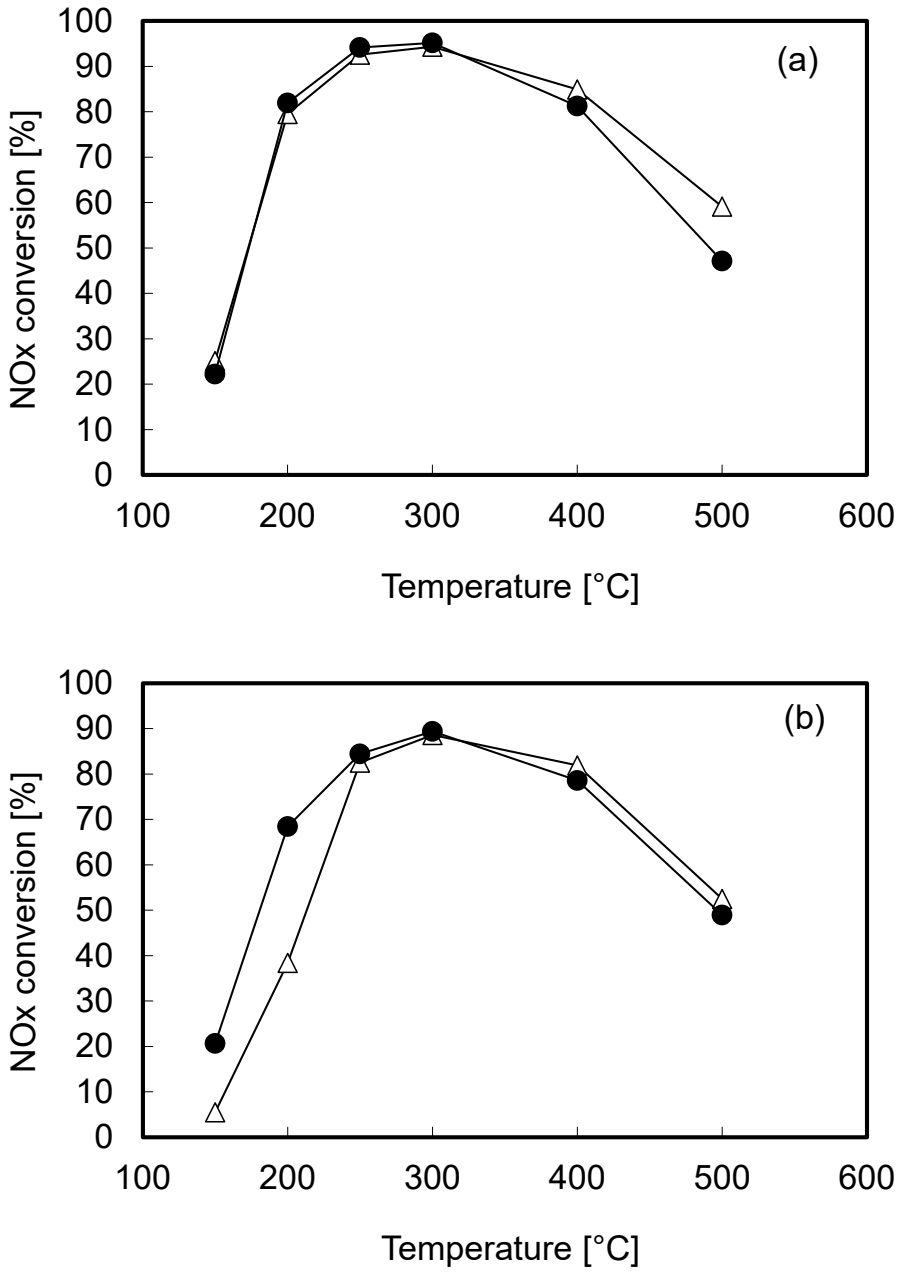

Figure 2-9 Conversion of NOx over Al,Fe-BEA zeolites with different Si/Al ratios (a) before and (b) after hydrothermal treatment at 700 ºC for 20 h. ∆ sample 6 (Si/Al = 36), ● sample 10 (Si/Al = 2400)

From the above investigation of the effects of the Si/Al ratio, it was found that the sample 10, which had Si/Al = 2400 and Si/Fe = 31 (Fe 2.9 wt%) displayed excellent low-temperature activity and post-hydrothermal aging stability (Figure 2-9). The NOx

conversions at 200 ºC before and after hydrothermal treatment were 82% and 68%, respectively, indicating high hydrothermal stability. The high hydrothermal stability was also confirmed by UV-Vis measurement. In the UV-Vis spectrum of the sample 10 after hydrothermal treatment at 700 ºC for 20 h (Figure 2-5(b)), the strong absorption assigned to isolated Fe^{3+} species was still observed below 300 nm, although the weak absorption assigned to Fe clusters was observed above 300 nm. To my knowledge, the hydrothermal stability of the sample 10 is the highest among Fe-based zeolite catalysts reported so far, although there are slight differences in the catalyst test conditions [5,6,8,22,33]. From Figure 2-9, it was also found that the fresh Al-free sample 10 showed a comparable performance to the sample 6 with a Si/Al ratio of 36, especially in the low to middle temperature range. This is not consistent with the result in Figure 2-8, where Al-richer zeolites show greater low-temperature activity. I now believe that the active Fe species is dispersed within the zeolite crystals in a different way. The proposed mechanism will be discussed later. In the high-temperature range (400-500 ºC), the NOx conversion with sample 6 was slightly higher than that with the sample 10. This difference in the NOx conversion may be due to the difference in the Si/(Al + Fe) ratio (17.2 for the sample 6 and 30.7 for the sample 10), namely the number of Brønsted acid sites, which is related to adsorption of NH_3 [35,36]. However, there was no difference in the NOx conversion between both samples after hydrothermal treatment. There was also no difference in NOx conversion over the sample 10 before and after hydrothermal treatment. These results strongly suggest that considerable numbers of catalytically active Fe species are present even after hydrothermal treatment.

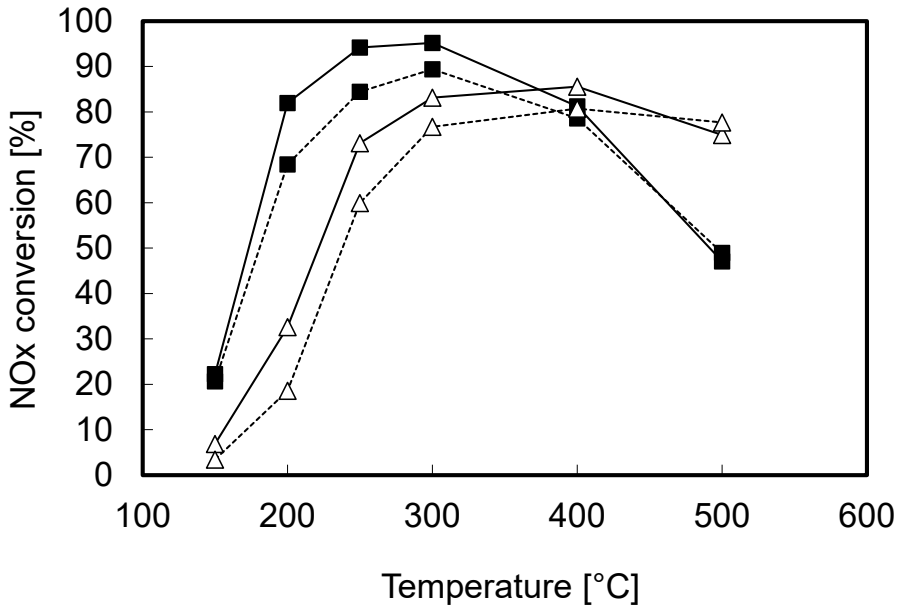

Figure 2-10 Conversion of NOx over the Al,Fe-BEA zeolite(■; sample 10) and (△) Fe/beta(250) before and after hydrothermal treatment at 700 ºC for 20 h. Solid line, fresh (before hydrothermal treatment); dotted line, after hydrothermal treatment.

To clarify the reason for the high hydrothermal stability of the sample 10, the catalytic performance of Fe-loaded beta (Fe/beta (250)) was investigated as a reference. In the preliminary experiments, there was no difference in the catalytic performance between Al,Fe-BEA zeolites with Si/Al ratios of 2400 and 200 (data not shown). Therefore, I compared the Al,Fe-BEA (Si/Al = 2400) with the Fe/beta(250). As shown in Figure 2-10, the NOx conversion of Fe/beta(250) in the lower-temperature range was considerably lower than that of the sample 10. As the silica-rich beta (Si/Al = 250) has few ion-exchange sites, hardly any highly dispersed Fe species are incorporated into the zeolite crystals by incipient wetness impregnation. Consequently, this is why Al-free Fe-BEA zeolite synthesized by the direct hydrothermal synthesis is very effective in the NH_3-SCR reaction.

In general, the active species in Fe-based zeolite catalysts for the NH_3-SCR in the low-temperature range is considered to be isolated Fe species. These include tetrahedrally coordinated framework Fe, non-framework Fe species (where the Fe atom is connected to the framework only by one, two or three remaining chemical bonds), and extra-framework Fe species (FeO^+). Figure 2-11 shows my putative mechanism for the formation of FeO^+ species during the calcination process [37]. For the Al,Fe-BEA zeolite, a framework Fe species is attacked by a proton from neighboring framework Al sites (Brønsted acid sites) resulting in formation of an extraframework FeO^+ species. The FeO^+ species is stabilized by the Al sites, and is active in NH_3-SCR as a Lewis acid site. This probably produces the h-peak around 500 ºC in the NH_3-TPD profiles. When dealumination occurs by hydrothermal treatment, however, the Fe species can move within zeolite pores and easily form agglomerates. Conversely, I believe, in the case of the Al-free Fe-BEA, the first neighboring proton attack step hardly occurs because the Si(OH)Fe group is a weaker acid than the conventional Si(OH)Al group. Consequently, complete removal of framework Fe and agglomeration of the generated extra-framework Fe species are greatly suppressed for Fe-BEA zeolites.

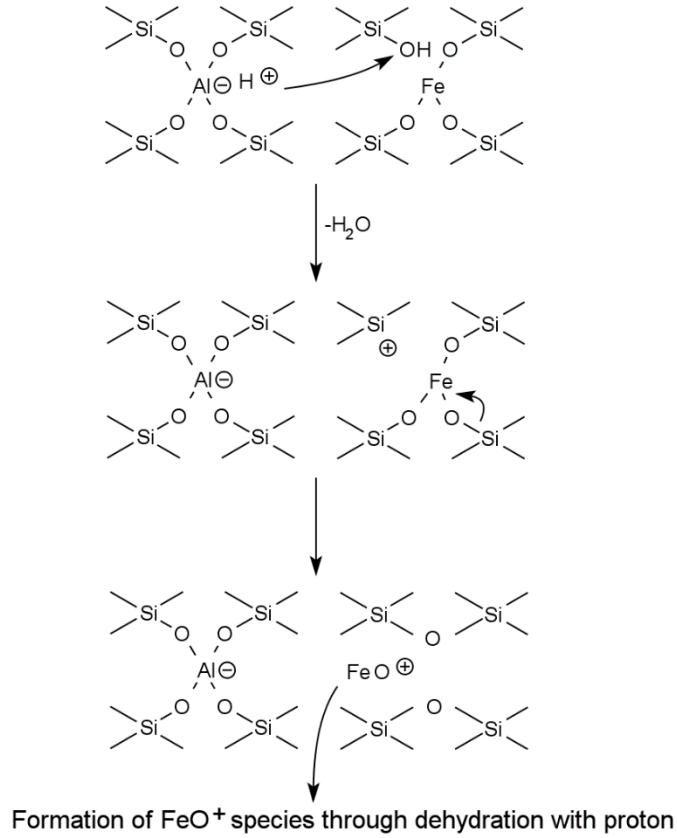

Figure 2-11 Scheme of formation of extraframework FeO^+ species in Al,Fe-BEA and Fe-BEA zeolites during calcination process.

4. **Conclusions**

I synthesized isomorphously substituted Fe-based BEA zeolites (Al,Fe-BEA and Al-free Fe-BEA) with various Si/Al and Si/Fe ratios to develop a novel catalyst with improved low-temperature activity in the NH_3-SCR of NOx. The resulting Al,Fe-BEA and Fe-BEA zeolites were highly crystalline, showing the large bipyramidal morphology that is typical of beta zeolites synthesized with fluoride. Their colors and XRD patterns indicated that the Fe present had been successfully incorporated into the BEA zeolite framework. For the fresh Al,Fe-BEA zeolites, the catalytic activity in the

low-temperature range (150-200 ºC) increased with a decrease in Si/Al and Si/Fe ratios. However, after hydrothermal treatment of the zeolites at 700 ºC for 20 h, a considerable reduction in the NOx conversion was observed. For the Al-free Fe-BEA zeolites, however, the NOx conversions at 200 ºC before and after hydrothermal treatment were 82% and 68%, respectively, indicating high hydrothermal stability. It was also found that the low-temperature activity of Al,Fe-BEA zeolite was higher than that of the Fe/beta catalysts. This strongly suggests that the incorporation of Fe into the zeolite framework is very effective for forming active species for the NH_3-SCR reaction.

References

[1] I. Nova and E. Tronconi, *Urea-SCR Technology for deNOx After Treatment of Diesel Exhausts*, Springer-Verlag New York **(2014)**.

[2] S. Brandenberger, O. Kröcher, A. Tissler, and R. Althoff, *Catal. Rev*. 50, 492 **(2008)**.

[3] M. Koebel, M. Elsener, and M. Kleemann, *Catal. Today* 59, 335 **(2000)**.

[4] H.Y. Huang, R.Q. Long, and R.T. Yang, *Appl. Catal. A Gen.* 235, 241 **(2002)**.

[5] P. Balle, B. Geiger, and S. Kureti, *Appl. Catal. B Environ.* 85, 109 **(2009)**.

[6] A. Grossale, I. Nova, and E. Tronconi, *Catal. Today* 136, 18 **(2008)**.

[7] M.P. Ruggeri, I. Nova, and E. Tronconi, *Top. Catal.* 56, 109 **(2013)**.

[8] Q. Sun, Z.-X. Gao, H.-Y. Chen, and W.M. Sachtler, *J. Catal.* 201, 89 **(2001)**.

[9] J. Perezramirez, *J. Catal.* 223, 13 **(2004)**.

[10] G.D. Pirngruber, M. Luechinger, P.K. Roy, A. Cecchetto, and P. Smirniotis, *J. Catal.* 224, 429 **(2004)**.

[11] H.-Y. Chen and W.M. Sachtler, *Catal. Today* 42, 73 **(1998)**.

[12] C. He, Y. Wang, Y. Cheng, C.K. Lambert, and R.T. Yang, *Appl. Catal. A Gen.* 368, 121 **(2009)**.

[13] P. Marturano, L. Drozdová, G.D. Pirngruber, A. Kogelbauer, and R. Prins, *Phys. Chem. Chem. Phys.* 3, 5585 **(2001)**.

[14] M. Høj, M.J. Beier, J.-D. Grunwaldt, and S. Dahl, *Appl. Catal. B Environ.* 93, 166 **(2009)**.

[15] R. Kumar, A. Thangaraj, R.N. Bhat, and P. Ratnasamy, *Zeolites* 10, 85 **(1990)**.

[16] A. Meagher, V. Nair, and R. Szostak, *Zeolites* 8, 3 **(1988)**.

[17] S. Bordiga, R. Buzzoni, F. Geobaldo, C. Lamberti, E. Giamello, A. Zecchina, G. Leofanti, G. Petrini, G. Tozzola, and G. Vlaic, *J. Catal.* 158, 486 **(1996)**.

[18] A.J. Chandwadkar, R.N. Bhat, and P. Ratnasamy, *Zeolites* 11, 42 **(1991)**.

[19] R.B. Borade and A. Clearfield, *Chem. Commun.* 11, 2267 **(1996)**.

[20] M. Asensi, A. Corma, A. Martínez, M. Derewinski, J. Krysciak, and S. Tamhankar, *Appl. Catal. A Gen.* 174, 163 **(1998)**.

[21] K. Rahkamaa-Tolonen, T. Maunula, M. Lomma, M. Huuhtanen, and R.L. Keiski, *Catal. Today* 100, 217 **(2005)**.

[22] A.M. Frey, S. Mert, J. Due-Hansen, R. Fehrmann, and C.H. Christensen, *Catal. Letters* 130, 1 **(2009)**.

[23] M.A. Camblor, A. Corma, and S. Valencia, *J. Mater. Chem.* 8, 2137 **(1998)**.

[24] G. Giordano, A. Katovic, and D. Caputo, *Stud. Surf. Sci. Catal.* 140, 307 **(2001)**.

[25] D. Aloi, F. Testa, L. Pasqua, R. Aiello, and J. B. Nagy, *Stud. Surf. Sci. Catal.* 142, 469 **(2002)**.

[26] R.B. Borade and A. Clearfield, *Microporous Mater.* 2, 167 **(1994)**.

[27] J. Perezramirez, J. Groen, A. Bruckner, M. Kumar, U. Bentrup, M. Debbagh, and L. Villaescusa, *J. Catal.* 232, 318 **(2005)**.

[28] P. Caullet, J. Hazm, J.L. Guth, J.F. Joly, J. Lynch, and F. Raatz, *Zeolites* 12, 240 **(1992)**.

[29] P. A. Jacobs and H. K. Beyer, *J. Phys. Chem.* 83(9), 1174 **(1979)**.

[30] S. Brandenberger, O. Kröcher, A. Tissler, and R. Althoff, *Appl. Catal. B*

Environ. 95, 348 **(2010)**.

[31] P.S. Metkar, N. Salazar, R. Muncrief, V. Balakotaiah, and M.P. Harold, *Appl. Catal. B Environ.* 104, 110 **(2011)**.

[32] S. Brandenberger, O. Kröcher, A. Wokaun, A. Tissler, and R. Althoff, *J. Catal.* 268, 297 **(2009)**.

[33] S. Shwan, R. Nedyalkova, J. Jansson, J. Korsgren, L. Olsson, and M. Skoglundh, *Ind. Eng. Chem. Res.* 51, 12762 **(2012)**.

[34] T. Sano, N. Yamashita, Y. Iwami, K. Takeda, and Y. Kawakami, *Zeolites* 16, 258 **(1996)**.

[35] L. Lietti, P. Forzatti, and F. Berti, *Catal. Letters* 41, 35 **(1996)**.

[36] L. Lietti, I. Nova, and P. Forzatti, *Top. Catal.* 11, 111 **(2000)**.

[37] G.H. Kühl, *J. Phys. Chem. Solids* 38, 1259 **(1977)**.

Chapter 3

Fe species in isomorphously substituted Fe-based BEA zeolites for low-temperature selective catalytic reduction of NO_x

1. **Introduction**

Use of Fe-based zeolite catalysts for reducing the amount of NO_x in automobile emissions by selective catalytic reduction with ammonia (NH_3-SCR) has been widely investigated [1-8]. This technique is especially effective for helping heavy-duty diesel vehicles meet environmental regulations, because zeolite catalysts are highly active and able to remove NO_x in a broad temperature range (150–500 °C). Generally, Fe-based zeolites are used for high-temperature (~500 °C) NH_3-SCR [9]. However, the low-temperature (150–250 °C) activity is also important owing to cold-start emission control and decrease in the emission gas temperature due to increased combustion efficiency. It is also well known that the catalytic activity of Fe-based zeolites is very sensitive to the NO/NO_2 relative amount, with the best performance observed at an equimolar ratio of NO and NO_2 [10]. Therefore, a better understanding of the nature of the active species in Fe-based zeolites is needed for developing de-NO_x catalysts with higher low-temperature activity. Moreover, the hydrothermal stability of Fe-based zeolites must also be improved for application in harsh environments and long-term use of the catalyst converter.

As I showed in Chapter 2, I found that an isomorphously substituted Fe-based BEA zeolite synthesized in fluoride media shows high catalytic activity in NH_3-SCR, and the Al-free Fe-based BEA zeolite has excellent hydrothermal stability compared to that of the conventional Fe-loaded BEA zeolite [11]. To clarify the difference in the catalytic performance, in this chapter, I investigated the chemical states of Fe species in Fe-BEA zeolites before and after hydrothermal treatment using various analytical techniques such as ^{27}Al magic-angle spinning nuclear magnetic resonance (MAS NMR), ^{29}Si MAS NMR, X-ray photoelectron spectroscopy (XPS), diffuse reflectance ultraviolet-visible absorption spectroscopy (UV-Vis), and electron paramagnetic resonance (EPR). On the basis of results obtained, the nature of the active species in NH_3-SCR catalyzed by the Fe-based BEA zeolite is discussed.

2. **Experimental**

2.1. Synthesis of Fe-based BEA zeolites

Fe-based BEA zeolites were hydrothermally synthesized according to the method reported by Pérez-Ramírez et al. [12]. $Fe(NO_3)_3 \cdot 9H_2O$ and $Al(NO_3)_3 \cdot 9H_2O$ were added to an aqueous solution of tetraethylammonium hydroxide (35 wt. %, TEAOH, Sachem) and the reaction mixture was stirred until the solids completely dissolved. Then, tetraethylorthosilicate (TEOS, 98%, Kishida Chemical Co., Ltd.) was added to the solution, which was stirred at room temperature. After complete hydrolysis of TEOS, the generated ethanol was removed by evaporation. Finally, aqueous HF (47 wt. %, Hirota Chemical Industry Co., Ltd.) was added dropwise, and the resulting

hydrogel was homogenized using a mortar. The molar composition of the hydrogel was SiO_2:$x$$Al_2O_3$:$y$$Fe_2O_3$:0.61TEAOH:0.50HF:7.5$H_2O$, where x = 0–0.05 and y = 0.0114–0.0308. The hydrogel was heated at 150 ºC under static conditions in a Teflon-sealed stainless steel autoclave (80 mL). After the crystallization was complete, the solid Fe-based BEA zeolite was filtered, washed, and dried overnight at 110 ºC. The dried product was calcined in air at 600 ºC for 2 h to remove the TEA cations occupying the zeolite pores.

2.2. Preparation of Fe-loaded BEA and Cu-loaded CHA zeolites

The conventional Fe-loaded BEA zeolite, Fe/beta(Si/Al), was also prepared by the incipient wetness impregnation method. Commercial beta zeolite with a Si/Al ratio of 14 (beta(14) from TOSOH Co.) was used as catalyst support. First, an aqueous $Fe(NO_3)_3$ solution was prepared, with the volume equal to the micropore volume of the support zeolite. Then, this solution was added to the zeolite, and the obtained wet powder was mixed to homogeneity and dried overnight at 110 ºC. Finally, the obtained solid product was calcined in air at 500 ºC for 2 h. The amount of Fe loading for Fe/beta(14) was 3.2 wt. %. A commercial H^+ type beta zeolite with a Si/Al ratio of 19 (beta(19) from TOSOH Co.) was also used as a non-Fe-loaded BEA zeolite for comparison.

For a better understanding the catalytic activity of Fe-based BEA zeolites compared to the state of the art catalysts, a Cu-loaded CHA (SSZ-13) zeolite (Cu/CHA) was prepared by the incipient wetness method. The CHA zeolite (Si/Al = 11) was

synthesized according to the literature [13]. Deionized water, sodium hydroxide (48 wt. %, Kaname Chemicals Co., Ltd.), and an aqueous solution of *N*,*N*,*N*-trimethyl-1-adamantylammonium hydroxide (13.3 wt. %, TMAdaOH, Sachem) were mixed, followed by the addition of aluminum hydroxide (Wako Pure Chemical Industries, Ltd.). Next, fumed silica (Aerosil 300, Nippon Aerosil Co., Ltd.) was added and mixed uniformly. The molar composition of the resulting hydrogel was $28SiO_2$:Al_2O_3:0.20TMAdOH:0.20NaOH:$44H_2O$. The hydrogel was then heated at 150 ºC under static conditions in a Teflon-sealed stainless steel autoclave (80 mL) for 4 d. After the crystallization was complete, the obtained solid was filtered, washed, and dried overnight at 110 ºC. The dried product was calcined in air at 600 ºC for 2 h to remove the TMAda cations occupying the zeolite pores. Prior to the catalytic tests, the Na cations in the calcined zeolite were exchanged with NH_4^+ in an aqueous solution of NH_4Cl (ca. 20 wt. %) at 40 °C for 0.5 h. Ion-exchange was repeated three times, and the resulting NH_4^+-form zeolite was thus obtained. Cu loading was carried out by the same procedure as that employed for Fe/beta(14), except for the use of aqueous $Cu(NO_3)_2$ as Cu source and performing calcination at 550 ºC for 2 h. The Cu loading for Cu/CHA was 4.5 wt. %.

2.3. Characterization

Powder X-ray diffraction patterns of the products were measured on a diffractometer (X'pert PRO MPD, Spectris, Japan) using Cu K_α radiation. The scanning range (2θ) was 3–43º. Elemental analysis was carried out by ICP-AES (OPTIMA 3000

DV, Perkin Elmer). Solid-state ^{29}Si and ^{27}Al MAS NMR spectra were measured on an NMRS-400 spectrometer (Varian, USA) using tetramethylsilane and $Al(NO_3)_3$ as internal standards, with resonance frequencies of 79.4 MHz and 104.2 MHz, respectively. The valence state of Fe was probed by XPS (ESCA-3400, Shimadzu, Japan) using Al K_α radiation. UV-Vis spectra were recorded on a diffuse reflectance UV-Vis spectrometer (UV-Vis 3100, Shimadzu, Japan) in the range of 220–700 nm using $BaSO_4$ as a blank, and subjected to the Kubelka-Munk conversion. EPR spectra were measured on JES-TE200 (JEOL, Japan) operating in X-band frequency (9.4 GHz) at –196 °C and room temperature. Nitrogen adsorption isotherms were measured at –196 °C with a volumetric apparatus (BELSORP-max, MicrotracBEL Corp., Japan). Samples (~0.05 g) were kept under vacuum at 350 °C for 2 h prior to the measurement.

The NH_3-SCR reaction was performed in a fixed-bed flow reactor under atmospheric pressure in the 150–500 ºC temperature range. The catalyst was pelletized, crushed, and sieved to 0.85–1.4 mm, and 1.5 mL of the sieved sample was placed in a quartz tube. The gas composition used was 200 ppm NO, 200 ppm NH_3, 10 vol. % O_2, 3 vol. % H_2O, with the rest being N_2. The total flow rate was set to 1.5 L/h, and the gas hourly space velocity (GHSV) was 60,000 h^{-1}. During the experiments, the temperature was lowered from 500 to 150 °C in steps of approximately 50 °C, and the NO_x conversion was calculated as follows:

$$NO_x \text{ conversion } (\%) = \frac{NO_{in} - NO_{out} - NO_{2out}}{NO_{in}} \times 100$$

Here, NO_{in} represents the NO inlet concentration (200 ppm) and NO_{out} and NO_{2out}

represent the NO and NO_2 outlet concentrations, respectively. In order to assess the long-term hydrothermal durability of the catalyst, I also investigated its performance after hydrothermal treatment at 700 °C for 20 h in a stream of gas containing 10 vol. % H_2O and 90 vol. % air with a GHSV of 6,000 h^{-1} (300 mL/min flow, 3 mL catalyst). To evaluate the steady state catalytic activity, the concentrations of NH_3, NO, and NO_2 in the outlet gas after 10 min of time-on-stream at each reaction temperature were analyzed by an FT-IR spectrometer (FT/IR-6100, JASCO, Japan) equipped with a gas cell (LPC-12M-S, 12m) and a mercury cadmium telluride detector cooled by liquid nitrogen. The concentrations were determined based on the intensities of the peaks at 1033, 1875, and 2917 cm^{-1} for NH_3, NO, and NO_2, respectively. Averaging over 30 scans was performed for each normalized spectrum.

3. **Results and discussion**

3.1. Synthesis and characterization of Fe-based BEA zeolites

Table 3-1 lists the hydrothermal synthesis conditions and characteristics of Fe-based BEA zeolites. Their XRD patterns were typical of *BEA zeolites containing no impurities from a co-crystallized phase, indicating that highly crystalline and pure-phase *BEA-type zeolites were obtained. All of the as-prepared samples were white, suggesting that Fe present in the zeolite was successfully incorporated into its framework. However, all of the prepared samples, with the exception of sample 3 (having the lowest Fe content of 1.1 wt. %), turned light brown after calcination. This change of color suggests a possible partial removal of Fe from the zeolite framework.

The good agreement of the Brunauer–Emmett–Teller (BET) surface area and the micropore volume calculated from the N_2 adsorption isotherm with those reported in literature [12] also confirmed that a highly crystalline BEA-type zeolite was obtained.

Table 3-1 Synthetic conditions and characteristics of Fe-based BEA zeolites.

Sample	Synthetic conditions[a]			Product (Fe-based BEA)				
	Si/Al	Si/Fe	Synthesis time [d]	Si/Al[b]	Si/Fe[b]	Fe [wt. %][b]	BET surface area [m^2/g][c]	Micropore volume [cm^3/g][d]
1	–	44	10.0	2400	31	2.9	480	0.22
2	250	33	10.0	200	26	3.5	–	–
3	36	35	10.5	36	33	2.7	470	0.23
4	20	88	10.5	21	83	1.1	–	–

[a] H_2O/SiO_2 = 7.5, $TEAOH/SiO_2$ = 0.61, HF/SiO_2 = 0.50, Temperature = 150 ºC, under static conditions.

[b] Measured by ICP.

[c] Calculated by the BET method.

[d] Calculated by the *t*-plot method.

3.2. Catalytic tests

Figure 3-1 shows the NO_x conversions at 200 °C over various Fe-based BEA zeolites, i.e., Fe/beta(14), beta(19), and Cu/CHA, before and after hydrothermal treatment at 700 °C for 20 h. All of the Fe-based BEA samples exhibited catalytic activity greater than that of Fe/beta(14). After hydrothermal treatment, however, NO_x conversions over the Fe-based zeolites with a higher Al content (samples 3 and 4) considerably decreased, almost reaching the conversion values of Fe/beta(14), i.e., 38–42%. In contrast, the Fe-based zeolites with a lower Al content (samples 1 and 2) still showed high catalytic activity, with 68% conversion for sample 1 and 73% for sample 2. However, no linear correlation between Al content and NO_x conversion after hydrothermal treatment was found. The catalytic activity of beta(19) was much lower than that of other Fe-containing zeolites, indicating that Fe is the catalytically active component in the SCR reaction.

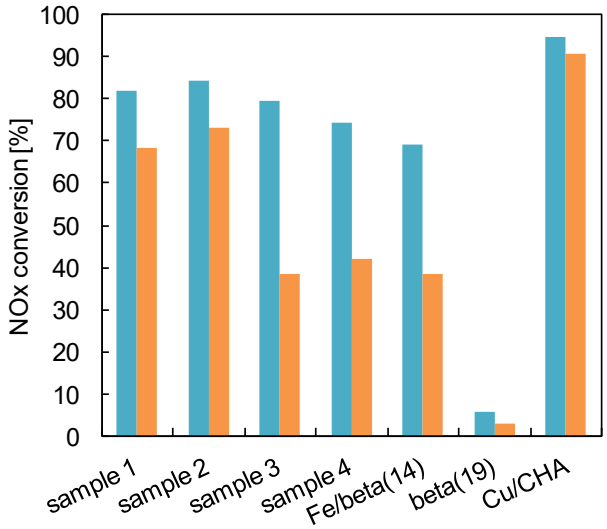

Figure 3-1 Conversion of NO_x at 200 °C over Fe-based BEA zeolites, Fe/beta(14), beta(19), and Cu/CHA before (blue) and after (orange) hydrothermal treatment at 700 °C for 20 h.

It is well known that Cu-loaded CHA zeolites show excellent performance in the low temperature NH_3-SCR since their sensitivity to the NO/NO_2 relative amount is much lower than that of Fe-based catalysts [1]. In this study, it was also confirmed that Cu/CHA exhibited the highest catalytic activity before and after hydrothermal aging. Surprisingly, the Fe-based BEA zeolites demonstrated high catalytic activity and hydrothermal stability even in the absence of NO_2.

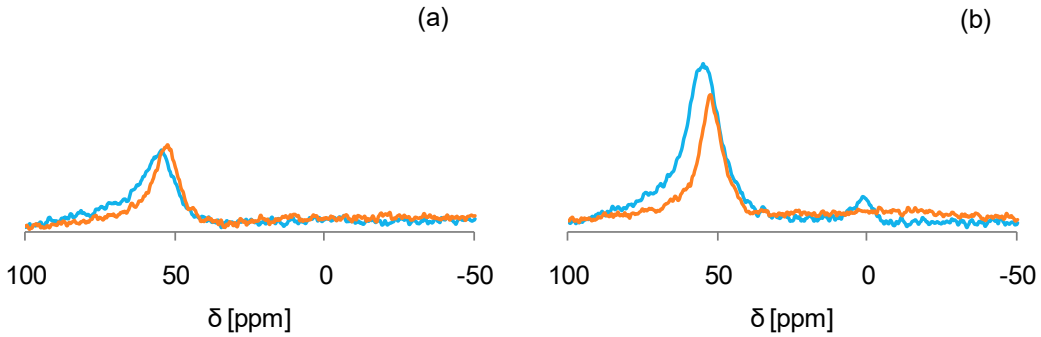

Figure 3-2 ^{27}Al MAS NMR spectra of (a) Fe-based BEA zeolite (sample 3) and (b) Fe/beta(14) before (blue) and after (orange) hydrothermal treatment at 700 °C for 20 h.

3.3. ^{27}Al and ^{29}Si MAS NMR

Figure 3-2 shows ^{27}Al MAS NMR spectra of sample 3 (Si/Al = 36, Fe = 2.7 wt. %) and Fe/beta(14) (Si/Al = 14, Fe = 3.2 wt. %). Both samples had a peak at around 52 ppm, which was assigned to tetrahedrally coordinated Al [14]. The peak around 0 ppm, attributable to octahedrally coordinated Al [14], was not observed for sample 3. For sample 3, no decrease in the intensity of the peak at 52 ppm was observed after hydrothermal treatment, indicating absence of dealumination. For Fe/beta(14), however, the reduction in the peak intensity was clearly observed (33%). The differing behavior of sample 3 and Fe/beta(14) is probably due to the differences in the number of

structural defects [15] and the framework Al content [16].

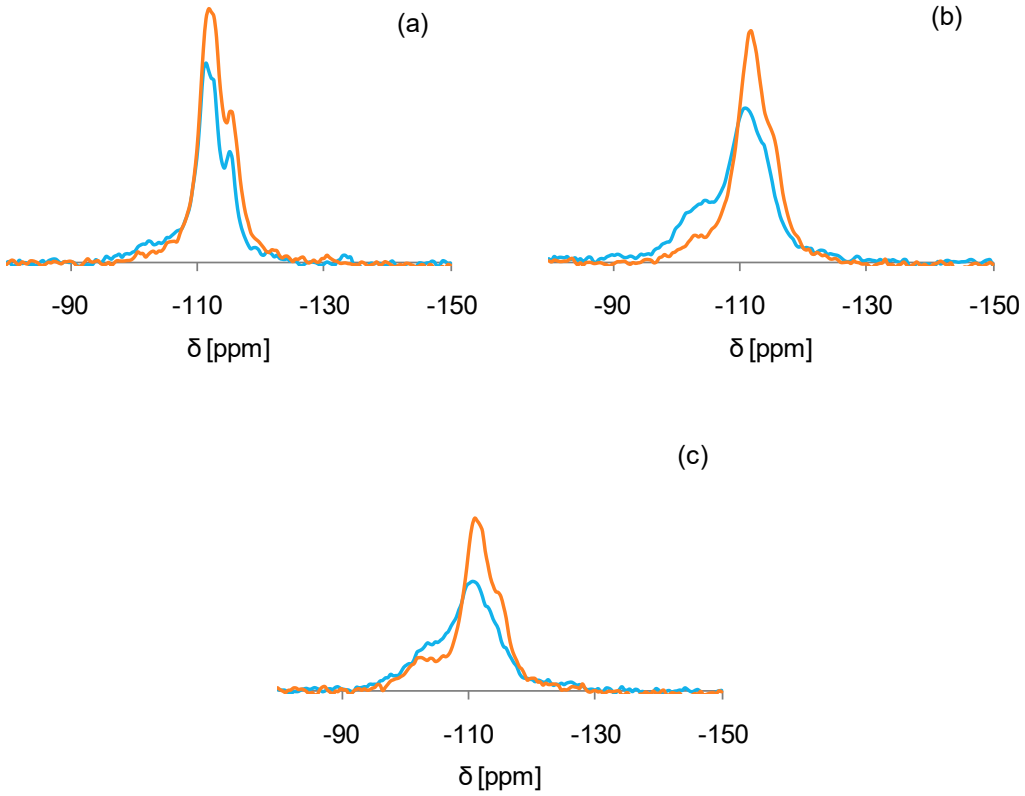

Figure 3-3 ^{29}Si MAS NMR spectra of Fe-based BEA zeolites and Fe/beta(14) before (blue) and after (orange) hydrothermal treatment at 700 °C for 20 h. (a) sample 1, (b) sample 3, and (c) Fe/beta(14).

The ^{29}Si MAS NMR spectra of sample 1, sample 3, and Fe/beta(14) before and after hydrothermal treatment are shown in Figure 3-3. The observed chemical shift reflects the coordination environment of Si, varying from approximately −103 to −117 ppm for Si(4Si) and from −97 to −106 ppm for Si(2Si, 2Al), Si(2Si, 1Al, 1Fe), Si(2Si, 2Fe), Si(3Si, 1Al), Si(3Si, 1Fe), or Si(3Si, 1OH) [14, 17]. In the spectrum of freshly prepared sample 1 (before hydrothermal treatment), the main peaks were detected at −111 and −115 ppm, characteristic of Si surrounded by 4 Si. A very weak broad peak was observed between −97 and −106 ppm. Taking into account the fact that the Si/Al

ratio of sample 1 is 2400, and the peak of the Si(3Si,1Fe), Si(2Si, 2Fe), or Si(2Si, 1Al, 1Fe) species is broadened by spin interaction with Fe^{3+}, the presence of Si in a Si(3Si,1OH) environment (structural defect) can be inferred. However, the intensity of the broad peak slightly decreased after hydrothermal treatment, suggesting detachment of framework Fe and the occurrence of dehydration between neighboring silanols during the hydrothermal treatment process.

On the other hand, the spectrum of freshly prepared sample 3 displayed a broad peak between −97 and −106 ppm. Even after hydrothermal treatment, the peak was clearly visible, although its intensity decreased. Since dealumination of framework Al hardly occurred for sample 3 (Figure 3-2), the difference between sample 1 and sample 3 in the intensity of the abovementioned broad peak suggests that the removal of framework Fe in sample 3 takes place easier than in sample 1. Subsequently, dehydration between the generated neighboring silanols occurs, resulting in the reduction of the number of Si(3Si, 1OH) species. The formation of Si(4Si) species was confirmed by an increase in peak intensity between −103 and –117 ppm. Since there is no difference in the Si/Fe ratio between sample 1 and sample 3, this phenomenon is probably due to the presence of strongly acidic sites, like Si(OH)Al, in sample 3, which accelerate the removal of framework Fe.

In the ^{27}Si MAS NMR spectrum of Fe/beta(14), the observed peak appeared to be broader compared to samples 1 and 3. As Fe/beta(14) was prepared by the incipient wetness impregnation method, most of the Fe species introduced were located in the zeolite pores, not in the framework. As a result, peak broadening occurred due to spin

interaction between the Fe species and the framework Si. The spectrum of sample 3 was also more broadened compared to sample 1, suggesting that more Fe exists as an extra-framework species.

3.4. XPS

The valence states of Fe in sample 3 were probed by XPS measurements (Figure 3-4). Fe_3O_4 and Fe_2O_3 were used as references for Fe^{2+} and Fe^{3+}. Roosendaal et al. reported that Fe 2p spectra show Fe^{2+} and Fe^{3+} binding energies of approximately 710 and 711 eV, respectively [18]. As shown in Figure 3-4, Fe_2O_3 showed a peak at 711.2 eV, whereas Fe_3O_4 showed a shoulder peak at 709.2 eV together with a peak at 711.2 eV, indicating the existence of Fe^{2+} in Fe_3O_4. Freshly prepared sample 3 had a Fe^{3+} peak at 711.2 eV and no apparent Fe^{2+} peak at 709.2 eV. However, the spectrum of this sample after hydrothermal treatment (aged) showed a weak shoulder peak around 709.2 eV. These results suggest that iron in the freshly prepared Fe-based BEA zeolite is mostly present as Fe^{3+}, but a minor part of it is reduced to Fe^{2+} during the hydrothermal treatment. The shoulder peak at 709.2 eV, assigned to Fe^{2+}, was not observed for the same sample after several months of storage (data not shown). Therefore, it was concluded that the Fe^{2+} species generated by hydrothermal treatment exists as extra-framework Fe that can be easily re-oxidized by atmospheric oxygen due to greater redox state stability of the Fe in the zeolite framework than that of the extra-framework Fe [19].

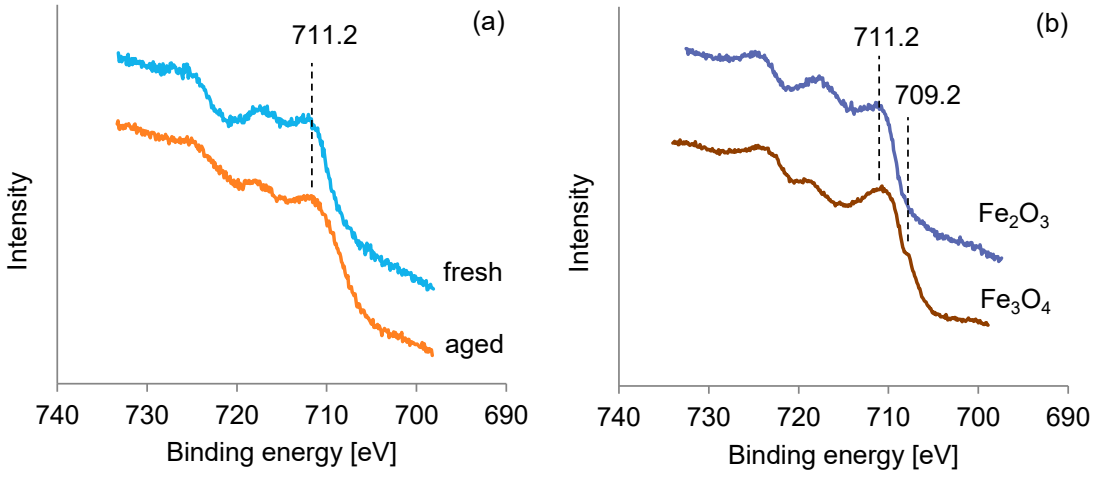

Figure 3-4 Fe 2p XPS spectra of (a) Fe-based BEA(sample 3) and (b) Fe_2O_3 and Fe_3O_4.

3.5. Diffuse reflectance UV-Vis

Diffuse reflectance UV-Vis spectra were measured to investigate the dispersion state of Fe (Figures 3-5 and 3-6). In previous UV-Vis studies of isomorphously substituted Fe zeolites, two different types of absorption bands were observed [12, 20-22]. The intense absorption band typically observed in the range of approximately 200–500 nm is attributed to charge transfer (CT) from the O^{2-} ligand to Fe^{3+} [12,21]. Isolated Fe^{3+} species, either tetrahedral or octahedral, absorb between 200 and 300 nm, and the $Fe^{3+}_xO_y$ cluster shows absorption at longer wavelengths (*ca.* 300–400 nm) [12, 23]. For larger Fe_2O_3 particles, absorption bands appear above 400 nm [12, 23]. Although definitive discrimination of Fe species is difficult, this grouping is useful for quantitative understanding of the transformation of Fe species during hydrothermal treatment [12]. Another type of absorption is observed between 350 and 550 nm, attributable to the *d-d* transitions of Fe^{3+} [12, 20-22]. Because the *d-d* transitions are

symmetry- and spin-forbidden, the absorption peak intensity is more than three orders of magnitude less than that of CT transitions. However, the absorption due to *d-d* transitions gives us useful information on the coordination environment of Fe^{3+}. For example, Goldfarb et al. reported that Fe-substituted SOD zeolite has four absorption lines at 373, 410, 436, and 480 nm, indicating tetrahedral coordination of Fe^{3+} [22]. Similar assignments were also found in other sources [20, 24].

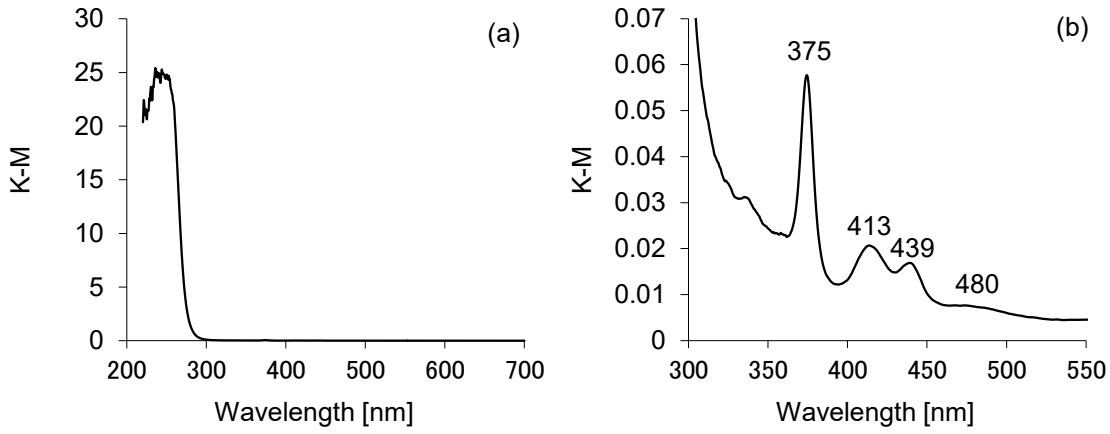

Figure 3-5 Diffuse reflectance UV-Vis spectra of the as-prepared sample 1 in (a) CT and (b) *d-d* transition regions.

Figure 3-5 shows the UV-Vis spectrum of the as-prepared sample 1. In the region of the *d-d* transitions, four absorption peaks were observed at 375, 413, 439, and 480 nm (very broad). These peaks were consistent with the results of Goldfarb et al. [22], suggesting that Fe^{3+} in sample 1 was successfully incorporated in the framework with tetrahedral coordination. The absorption in the CT region was observed only below 300 nm, confirming that the Fe species in the as-prepared sample 1 is exclusively isolated Fe^{3+}.

The spectra of all samples before and after hydrothermal treatment are compared in Figure 3-6. Li et al. [25] and Perez-Ramirez et al. [12] reported that absorption spectra can be deconvoluted to subbands by a Gausian curve. The amounts of Fe species calculated from the deconvoluted subbands are summarized in Table 3-2, where the absorption subbands of <300 nm, 300–400 nm, and >400 nm were regarded as isolated Fe^{3+}, $Fe^{3+}_xO_y$ clusters, and Fe_2O_3 particles, respectively. Freshly prepared Fe-based BEA samples showed similar absorption spectra, mainly consisting of the subbands at 211 and 272 nm, and having some weak subbands above 300 nm. Therefore, most of the Fe^{3+} (>89%) exists as isolated Fe^{3+} in fresh samples, although the coordination environment of Fe^{3+} (framework or extra-framework) is not clear at the present time. In contrast, the Fe/beta(14), prepared by the incipient wetness impregnation method, had a broader absorption spectrum compared to Fe-based BEA samples. The higher proportion of the subbands above 300 nm indicates that Fe/beta(14) contains considerable amounts of $Fe^{3+}_xO_y$ clusters and Fe_2O_3 particles (17.2 wt. % and 3.1 wt. %, respectively), even when fresh. Unfortunately, the absorption due to *d-d* transitions was masked by the CT peak, which extended to longer wavelengths (>300 nm) for all samples. Therefore, no information concerning the coordination environment could be derived from this region.

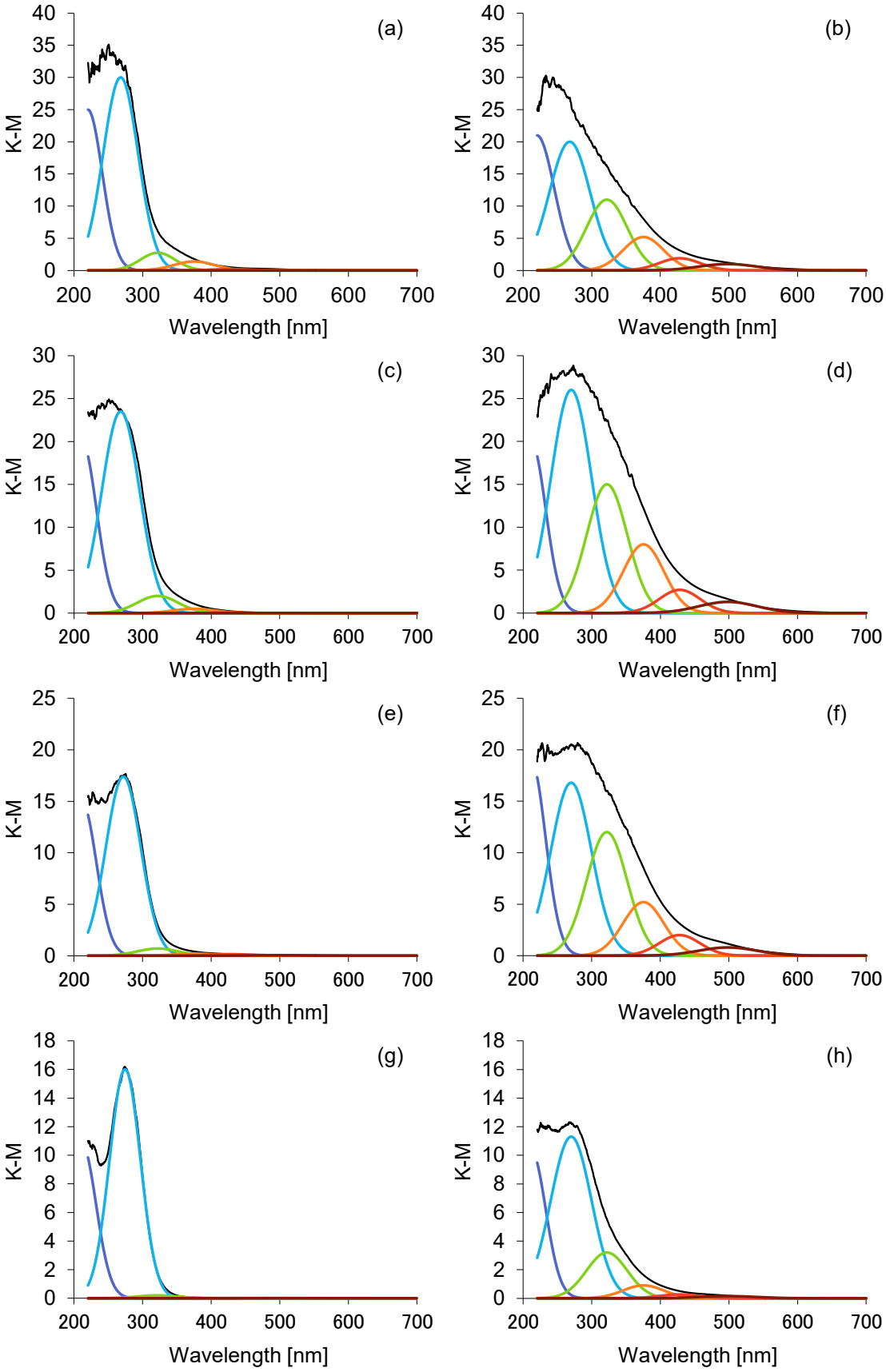
(a)
(b)
(c)
(d)
(e)
(f)
(g)
(h)
K-M
Wavelength [nm]

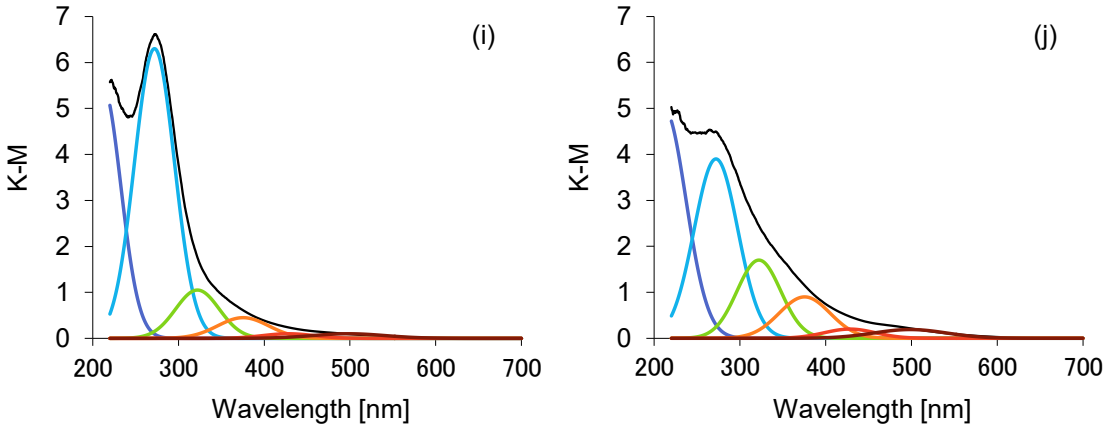

Figure 3-6 Diffuse reflectance UV-Vis spectra of Fe-based BEA zeolites and Fe/beta(14) before and after hydrothermal treatment at 700 °C for 20 h. (a) sample 1 (fresh), (b) sample 1 (aged), (c) sample 2 (fresh), (d) sample 2 (aged), (e) sample 3 (fresh), (f) sample 3 (aged), (g) sample 4 (fresh), (h) sample 4 (aged), (i) Fe/beta(14) (fresh), and (j) Fe/beta(14) (aged).

Another feature was observed for the intensity of the subbands at 211 and 272 nm (denoted as Sb1 and Sb2, respectively) shown in Figure 3-6. The Fe-rich samples (samples 1, 2, and 3; Si/Fe < Si/Al) had nearly equivalent Sb1 and Sb2 subbands. In contrast, the Al-rich samples (sample 4 and Fe/beta(14)) had an apparently stronger Sb2 subband. Perez-Ramirez et al. found that the subband at 285 nm in calcined and hydrated Fe-ZSM-5 disappeared after thermal treatment at 500 °C, demonstrating that it is due to octahedral Fe^{3+} [12]. Therefore, it can be assumed that the formation of octahedral (extra-framework) Fe^{3+} contributes to the increase in the intensity of the Sb2 subband in Fe/beta(14), where the Fe species should be in an extra-framework position. I can therefore assume that sample 4 has more extra-framework Fe^{3+} than that of other Fe-rich zeolites; in other words, the detachment of framework Fe occurs more easily in Al-rich zeolites. As listed in Table 3-2, however, the percentage of isolated Fe^{3+} in fresh samples increases concomitantly with the Al content (decrease in the Si/Al ratio). This

can be explained by Al acidic sites anchoring the detached Fe^{3+} and preventing its agglomeration. Obviously, Fe acidic sites could also be considered anchoring sites. Such detached Fe^{3+} species anchored on Fe acidic sites could be recognized as binuclear clusters, since the anchored Fe^{3+} species coordinate to the oxygen atoms next to the framework Fe. Based on the definition used in this study, Fe binuclear clusters should exhibit absorption in the 300–400 nm range in the UV-Vis spectrum; however, Pirngruber *et al.* reported that Fe binuclear clusters could absorb below 300 nm [26]. Thus, at the present time, I cannot determine the region where the binuclear clusters exhibit their absorption bands. However, considering the ^{29}Si MAS NMR results showing that the detachment of Fe in sample 1 (Si/Al = 2400) was more suppressed than that in sample 3 (Si/Al = 36), it can be concluded that the amount of Fe binuclear clusters was so small that it would lead to no major change in the UV-Vis spectrum. Therefore, combining these characterization results with the catalytic test data in Figure 3-1, it can be concluded that the isolated Fe^{3+} (both framework and extra-framework) is the catalytically active species in the low-temperature NH_3-SCR.

Table 3-2 Fe species content calculated from the deconvoluted UV-Vis subbands.

Sample		Isolated Fe^{3+}		$Fe^{3+}{}_xO_y$ clusters		Fe_2O_3 particles	
		[%][a]	[wt%]	[%][a]	[wt%]	[%][a]	[wt%]
1	fresh	89.5	2.6	10	0.29	0.5	0.02
	aged	58.8	1.7	34.2	0.99	7.0	0.20
2	fresh	91.0	3.1	8.8	0.30	0.2	0.01
	aged	51.9	1.8	40.2	1.38	8.0	0.27
3	fresh	94.2	2.5	4.6	0.12	1.1	0.03
	aged	50.4	1.3	41.9	1.12	7.7	0.20
4	fresh	98.4	1.0	1.4	0.01	0.2	0.00
	aged	74.4	0.8	22.9	0.24	2.7	0.03
Fe/beta(14)	fresh	79.6	2.5	17.2	0.55	3.1	0.10
	aged	63.2	2.0	30.7	0.98	6.1	0.20

[a]Calculated from integrated subbands.

Isolated Fe^{3+}: $\lambda < 300$ nm

$Fe^{3+}{}_xO_y$ clusters: 300 nm $< \lambda <$ 400 nm

Fe_2O_3 particles: $\lambda > 400$ nm

After hydrothermal treatment, the intensities of subbands above 300 nm increased for all samples (Figure 3-6), indicating further formation of $Fe^{3+}_xO_y$ clusters and Fe_2O_3 particles. Among Fe-based BEA samples, only sample 4 showed a higher percentage of isolated Fe^{3+}. Probably, the low amount of Fe (1 wt. %) in sample 4 is beneficial for preserving isolated Fe^{3+}. Among the other samples (1–3), there was no significant difference in the Fe^{3+} species content, despite the wide variation of the Si/Al ratio. However, a large difference in NO_x conversion of the NH_3-SCR reaction was observed among Fe-based BEA zeolites with different Si/Al ratios after hydrothermal treatment (Figure 3-1). This inconsistency implies the existence of several isolated Fe^{3+} species with different chemical environments. To confirm the characterization, EPR measurements were performed to elucidate the chemical environment of isolated Fe^{3+}, which is most relevant to catalytic activity.

3.6. EPR

EPR spectra were measured at both room temperature and –196 °C to further investigate the environment of isolated Fe^{3+}. Although many researchers have already investigated the chemical states of Fe species present in zeolites using this technique, the interpretation of the measurement results is not straightforward [21-24, 27-31]. The major *g* values observed in Fe zeolites are *ca.* 2.0 and 4.3. The peak at $g \approx 4.3$ has sometimes been assigned to framework Fe^{3+} in zeolites [27, 32, 33]. However, the peak at $g \approx 2.0$ has also been attributed to framework Fe^{3+} [21, 24, 29]. Since the positions of EPR peaks depend solely on the Fe^{3+} environment symmetry (highly symmetric or distorted), EPR alone cannot discriminate between tetrahedrally or octahedrally coordinated Fe^{3+} [12, 23]. Therefore, elucidation of the Fe^{3+} environment is possible only in combination with analytical results obtained using several other methods.

Figure 3-7 shows the EPR spectrum of the as-prepared sample 1, measured at –196 °C. Several signals were observed at $g \approx 2.0$, $g \approx 4.3$, and $g \geq 4.3$. Since the UV-Vis data confirmed the presence of tetrahedrally coordinated Fe^{3+} in sample 1, these signals can be attributed to tetrahedral Fe^{3+} with different symmetries. The signal at $g \approx 2.0$ is assigned to highly symmetric tetrahedral Fe^{3+} [12, 23]. As the signals at $g \approx 4.3$ and $g \geq 4.3$ are known to correspond to Fe^{3+} in a distorted tetrahedral or octahedral environment [12, 23], I can assign them to distorted tetrahedral Fe^{3+}. The as-prepared sample contains TEA^+ in its micropores, which may lead to the distortion of some tetrahedral Fe^{3+} by the interaction between Si-O^--Fe and TEA^+. The lattice expansion caused by TEA^+ may also affect the distortion of the coordination environment.

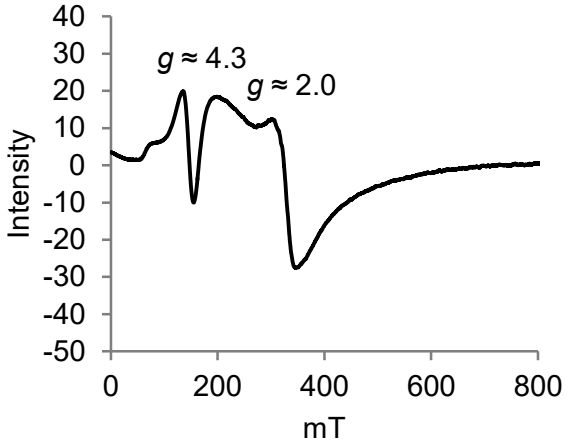

Figure 3-7 EPR spectrum at –196 °C of the as-prepared sample 1.

Before EPR measurements at –196 °C, the temperature dependence of the signal intensity was investigated. Figure 3-8 shows the comparison of the spectra of sample 1 (before and after hydrothermal treatment) measured at room temperature and –196 °C. The signal at $g \approx 2.0$ appeared to be dominant after calcination, suggesting that the distortion of Fe^{3+} disappears after removal of TEA^{+}. Bordiga et al. reported that Fe clusters and oxide particles exhibit stronger $g \approx 2.0$ signals at 25 °C than at –196 °C, disobeying the Curie law due to mutual magnetic interaction [21]. In Figure 3-8, the intensity of the signal at $g \approx 2.0$ was enhanced by decreasing the measurement temperature (in agreement with the Curie law), suggesting that the signal at $g \approx 2.0$ can be assigned to isolated Fe^{3+} in a highly symmetric environment. Presently, discrimination between tetrahedral or octahedral Fe^{3+} is not possible. After hydrothermal aging, the signal intensity at $g \approx 2.0$ (measured at room temperature) slightly increased. This is due to an increase in the amounts of Fe clusters and oxide particles, as confirmed by UV-Vis measurements. However, no difference in signal temperature dependence between fresh and aged samples was observed, and the

dominant Fe^{3+} species having a signal at $g \approx 2.0$ would still be isolated Fe^{3+} in a highly symmetric environment, even after hydrothermal aging.

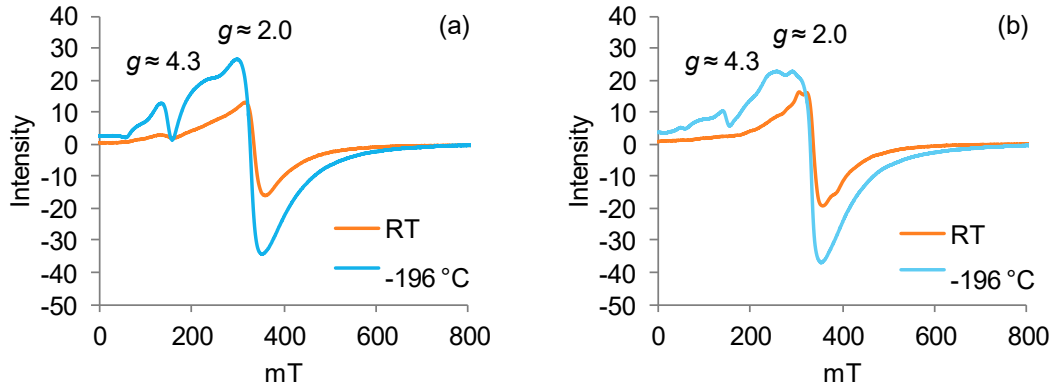

Figure 3-8 EPR spectra of (a) sample 1 (fresh) and (b) sample 1 (aged) measured at room temperature (red) and –196 °C (blue).

Figure 3-9 shows the EPR spectra of all samples measured at –196 °C before and after hydrothermal treatment. The fresh samples are discussed first. EPR signals of $g \approx 2.0$, $g \approx 4.3$, and $g \geq 4.3$ were observed for every sample. Samples 1, 2, and 3 had considerably larger signals at $g \approx 2.0$ compared to Fe/beta(14). Sample 4 exhibited a smaller signal at $g \approx 2.0$, due to its low Fe content (1.1 wt. %). It was also found that although there was no difference in the amount of Fe loading between sample 1, sample 3, and Fe/beta(14), sample 1 with low Al content showed a considerably stronger signal. The dominant Fe^{3+} species for sample 1 and 2 was the isolated Fe^{3+} in a highly symmetric environment ($g \approx 2.0$). In contrast, the relatively stronger signals at $g \approx 4.3$ were observed for samples 3 and 4. Similar signals were observed for Fe/beta(14) prepared by the incipient wetness impregnation method, being consistent with signals of the Fe ion-exchanged zeolites in previous reports [21, 30]. Therefore, it is speculated

that a part of framework Fe^{3+} in samples 3 and 4 detached during calcination process, yielding an extra-framework Fe^{3+} species, e.g. FeO^{+}. This speculation seems to be supported by the results of ^{29}Si MAS NMR and UV-Vis measurements.

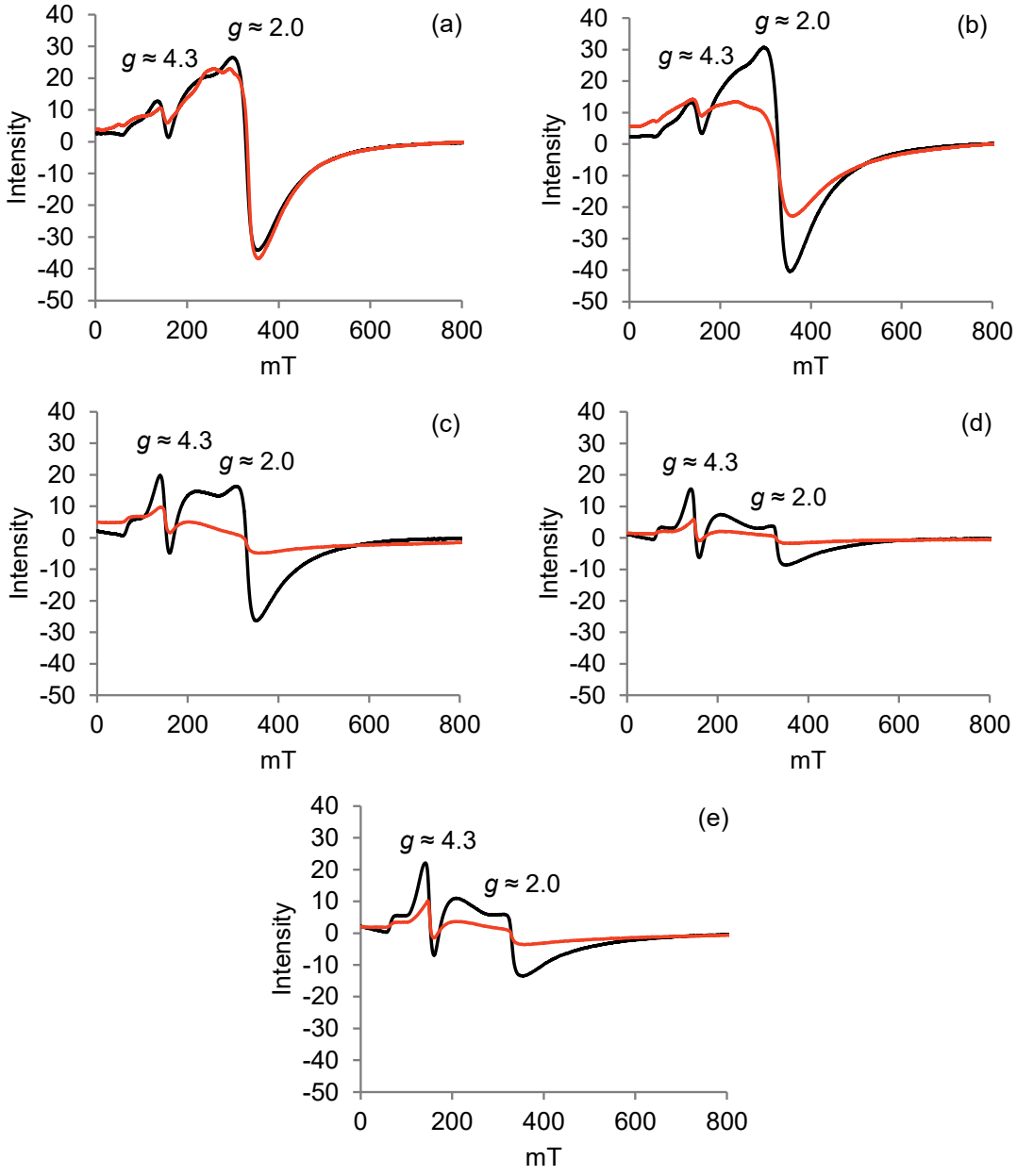

Figure 3-9 EPR spectra at –196 °C of Fe-based BEA zeolites and Fe/beta(14) before (black) and after (red) hydrothermal treatment at 700 °C for 20 h. (a) sample 1, (b) sample 2, (c) sample 3, (d) sample 4, and (e) Fe/beta(14).

For aged samples, an interesting result was obtained for the signals at $g \approx 2.0$. The signal intensity of sample 1 was hardly changed by the hydrothermal treatment. The signal intensity for the aged sample 2 was nearly half of that of the fresh sample. On the other hand, sample 3, sample 4, and Fe/beta(14) exhibited almost identical spectra with weak signals. Since highly asymmetric Fe species are known to be EPR-silent [31], I assume a high degree of asymmetry for the Fe species in the above samples with weak signals. Figure 3-10 shows the relationship between the degree of signal retention at $g \approx 2.0$ before and after hydrothermal treatment [(signal height of aged sample / signal height of fresh sample) × 100%], and the Fe/Al ratio. Clearly, the retention degree increased with increasing Fe/Al ratio in the range of Fe/Al > 1. This means that the decrease in the number of highly symmetric Fe^{3+} species is suppressed more when the number of framework Fe atoms exceeds that of the framework Al. More specifically, I believe that during hydrothermal treatment, framework Fe (tetrahedral or octahedral) is easily attacked by protons from Brønsted acidic sites (Si(OH)Al), resulting in detachment of Fe from the zeolite framework if the Fe/Al ratio is below 1. Such detached Fe^{3+} species are more likely to move and form clusters and particles during hydrothermal treatment. The proposed scheme for Fe detachment is illustrated in Figure 3-11. In samples with Fe/Al > 1, the probability of the occurrence of a neighboring Fe and Al pair in the zeolite framework decreases, because of which Fe^{3+} stays within the framework. The signal behavior at $g \approx 2.0$ during hydrothermal treatment strongly suggests that the isolated Fe^{3+} species responsible for this signal is most relevant to the catalytic activity in the low-temperature NH_3-SCR. Such isolated Fe^{3+} species can be assigned to both framework Fe^{3+} with tetrahedral coordination and non-framework Fe^{3+}

with tetrahedral or octahedral coordination, where the Fe atom is connected to the framework only by one, two, or three remaining chemical bonds.

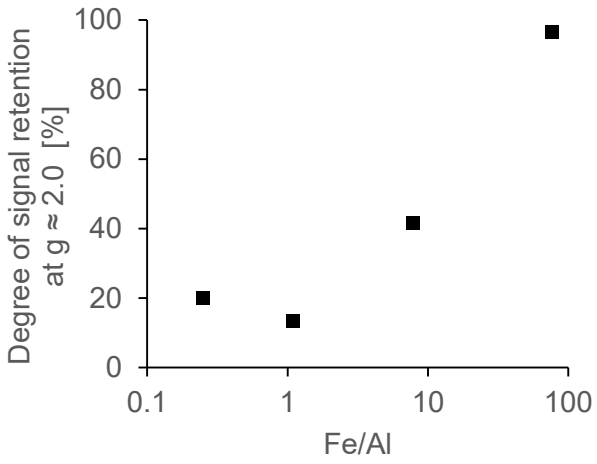

Figure 3-10 Relationship between the degree of signal retention at $g \approx 2.0$ before and after hydrothermal treatment at 700 °C for 20 h, and the Fe/Al ratio of Fe-based BEA zeolites. Degree of signal retention at $g \approx 2.0$ = (signal height of aged sample / signal height of fresh sample) × 100 (%).

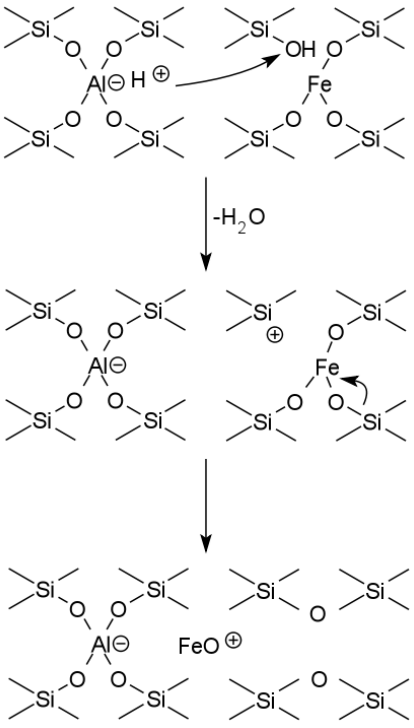

Figure 11 Proposed scheme of Fe detachment in Fe-based BEA zeolites.

4. **Conclusions**

Isomorphously substituted and highly crystalline Fe-based BEA zeolites with various Si/Al and Si/Fe ratios were synthesized in fluoride media, and the relationship between the chemical states of the Fe species and catalytic activity in the NH_3-SCR reaction was investigated. The ^{27}Al and ^{29}Si MAS NMR measurements show that dealumination hardly occurred in Fe-based BEA zeolites, but structural defects (silanols) were generated by the detachment of framework Fe for Al-rich samples. UV-Vis measurements confirmed that the majority of Fe species in the fresh samples was isolated Fe^{3+}. These results therefore indicate that isolated Fe^{3+} is the active species for the low-temperature NH_3-SCR. EPR measurements at –196 °C also revealed that the Fe species with a signal at $g \approx 2.0$ is most relevant to the high catalytic activity at low temperatures. For samples with Fe/Al ratios > 1, such Fe^{3+} species were mostly preserved after hydrothermal aging. In contrast, the signal at $g \approx 2.0$ significantly decreased for samples with Fe/Al ratios < 1 due to the detachment of framework Fe by protonation via neighboring acidic sites (Si(OH)Al). The high catalytic activity and stability of the Fe-based BEA zeolites with Fe/Al ratios > 1 is probably due to the high content of isolated Fe^{3+} and the suppression of framework Fe detachment due to fewer Al acidic sites.

References

[1] I. Nova and E. Tronconi, *Urea-SCR Technology for deNOx After Treatment of Diesel Exhausts*, Springer-Verlag New York **(2014)**.

[2] S. Brandenberger, O. Kröcher, A. Tissler, and R. Althoff, *Catal. Rev.* 50, 492 **(2008)**.

[3] T. J. Toops, K. Nguyen, A. L. Foster, B. G. Bunting, N. A. Ottinger, J. A. Pihl, E. W. Hagaman, and J. Jiao, *Catal. Today* 151, 257 **(2010)**.

[4] H. Y. Huang, R. Q. Long, and R. T. Yang, *Appl. Catal. A Gen.* 235, 241 **(2002)**.

[5] P. Balle, B. Geiger, and S. Kureti, *Appl. Catal. B Environ.* 85, 109 **(2009)**.

[6] A. Grossale, I. Nova, and E. Tronconi, *Catal. Today* 136, 18 **(2008)**.

[7] M. P. Ruggeri, I. Nova, and E. Tronconi, *Top. Catal.* 56, 109 **(2013)**.

[8] Q. Sun, Z.-X. Gao, H.-Y. Chen, and W. M. Sachtler, *J. Catal.* 201, 89 **(2001)**.

[9] S. Brandenberger, O. Kröcher, A. Tissler, and R. Althoff, *Appl. Catal. B Environ.* 95, 348 **(2010)**.

[10] M. Koebel, G. Madia, and M. Elsener, *Catal. Today* 73, 239 **(2002)**.

[11] Y. Naraki, K. Ariga, and H. Aoyama, Nitrogen oxide-reducing catalyst and method for reducing nitrogen oxide. U.S. Patent 7,794,680, September 14 **(2010)**.

[12] J. Pérez-Ramírez, J. Groen, A. Bruckner, M. Kumar, U. Bentrup, M. Debbagh, and L. Villaescusa, *J. Catal*. 232, 318 **(2005)**.

[13] H. Robson, *Verified Syntheses of Zeolitic Materials Second Revised Edition 2001*, Elsevier, Amsterdam, **(2001)**.

[14] J. Pérez-Pariente, J. Sanz, V. Fornés, and A. Corma, *J. Catal.* 124, 217 **(1990)**.

[15] P. A. Barrett, M. A. Camblor, A. Corma, R. H. Jones, and L. A. Villaescusa,

Chem. Mater. 9, 1713 **(1997)**.

[16] T. Sano, N. Yamashita, Y. Iwami, K. Takeda, and Y. Kawakami, *Zeolites* 16, 258 **(1996)**.

[17] C. A. Fyfe, J. M. Thomas, J. Klinowski, and G. C. Gobbi, *Angew. Chemie Int. Ed. English* 22, 259 **(1983)**.

[18] S. J. Roosendaal, B. van Asselen, J. W. Elsenaar, A. M. Vredenberg, and F. H. P. M. Habraken, *Surf. Sci.* 442, 329 **(1999)**.

[19] J. Pérez-Ramírez, G. Mul, F. Kapteijn, J. A. Moulijn, A. R. Overweg, A. Doménech, A. Ribera, and I. W. C. E. Arends, *J. Catal.* 207, 113 **(2002)**.

[20] J. H. Yun and R. F. Lobo, *J. Catal.* 312, 263 **(2014)**.

[21] S. Bordiga, R. Buzzoni, F. Geobaldo, C. Lamberti, E. Giamello, A. Zecchina, G. Leofanti, G. Petrini, G. Tozzola, and G. Vlaic, *J. Catal.* 158, 486 **(1996)**.

[22] D. Goldfarb, M. Bernardo, K. G. Strohmaier, D. E. W. Vaughan, and H. Thomann, *J. Am. Chem. Soc.* 116, 6344 **(1994)**.

[23] M. S. Kumar, M. Schwidder, W. Grünert, and A. Brückner, *J. Catal.* 227, 384 **(2004)**.

[24] J. W. Park and H. Chon, *J. Catal.* 133, 159 **(1992)**.

[25] L. Li, Q. Shen, J. Li, Z. Hao, Z. P. Xu, and G. Q. M. Lu, *Appl. Catal. A Gen.* 131, 344 **(2008)**.

[26] G.D. Pirngruber, P.K. Roy, and R. Prins, *Phys. Chem. Chem. Phys.* 8, 3939 **(2006)**.

[27] B. Wichterlová and P. Jiru, *React. Kinet. Catal. Lett.* 13, 197 **(1980)**.

[28] A. V. Kucherov and A. A. Slinkin, *Zeolites* 8, 110 **(1988)**.

[29] G. Catana, J. Pelgrims, and R. A. Schoonheydt, *Zeolites* 15, 475 **(1995)**.

[30] A. Brückner, U. Lohse, and H. Mehner, *Microporous Mesoporous Mater.* 20, 207 **(1998)**.

[31] S. Faggian, P. Fisicaro, E. Giamello, R. Gobetto, A. Viale, G. Berlier, C. Lamberti, and I. Rossetti, *J. Phys. Chem. B* 107, 8922 **(2003)**.

[32] P. Wenquin, Q. Shilun, K. Zhiyun, and P. Shaoyi, *Stud. Surf. Sci. Catal.* 49, 281 **(1989)**.

[33] A. F. Ojo, J. Dwyer, and R. V. Parish, *Stud. Surf. Sci. Catal.* 49, 227 **(1989)**.

Chapter 4

An isomorphously substituted Fe-BEA zeolite with high Fe content: facile synthesis and characterization

1. **Introduction**

Fe-based zeolites are attractive catalysts due to their broad applicability and the abundance of iron in nature [1-5]. Having attracted attention in the field of automobile emission technology, these materials have been widely investigated, particularly as catalysts for the selective catalytic reduction of NO_x with ammonia (NH_3-SCR) [6-10]. As the emission regulations become stricter, low-temperature (150–250 °C) catalytic activity becomes indispensable for practical applications. Currently, Cu-based small-pore zeolites such as CHA and AEI are often used for low-temperature NH_3-SCR due to their excellent catalytic activity and hydrothermal stability [6,11-13]. Fe-based zeolites can also effectively catalyze the NH_3-SCR reaction, exhibiting the advantage of greater resistance to sulfur poisoning. However, a drawback of Fe-based zeolite catalysts is that their NH_3-SCR activity is very sensitive to the NO/NO_2 ratio, with the best performance achieved only at an equimolar ratio of NO and NO_2 [14].

Isomorphous substitution method is a well-known technique for giving highly dispersed and tetrahedrally coordinated hetero-atom in the framework structure. Also, it has been extensively studied to control acidity of zeolite catalysts in acid-base reactions because the strength of Brønsted acid sites decreases by substitution of Al in the

framework with other trivalent cations (e.g., B, Fe, Ga, and In) [15,16]. In Chapter 2 and Chapter 3, I reported that an isomorphously substituted Al-free Fe-based BEA zeolite (Fe-BEA) synthesized in a fluoride medium exhibited high catalytic activity and hydrothermal stability in the NH_3-SCR reaction in the absence of NO_2 [17,18]. From an industrial point of view, however, the use of fluoride in zeolite production is a challenge, because it causes serious corrosion. Kumar et al. and Borade et al. reported that an isomorphously substituted Fe-BEA zeolite with a high Fe content could be synthesized without the addition of fluoride [19,20]. The described method, however, required a long crystallization time of more than 10 days and a significant amount of tetraethylammonium cations (TEA^+) as an organic structure-directing agent (OSDA), with a TEA^+/SiO_2 ratio of 0.48–1.4. Raj et al. also reported the synthesis of an isomorphously substituted Fe-BEA zeolite using a TEA^+/SiO_2 ratio of 0.05 and an OH^-/SiO_2 ratio of 0.165 [21]. However, this synthesis also required a long crystallization time (15 days).

Therefore, in this chapter, I tried to synthesize an isomorphously substituted Al-free Fe-BEA zeolite with a high Fe content by adopting a more industrially friendly approach. When an excess amount of sodium hydroxide was used, the amount of tetraethylammonium hydroxide (TEAOH) could be reduced, and a highly crystalline Fe-BEA zeolite was obtained after only 90 h of crystallization time. The obtained zeolite was unique due to its extremely high Fe content (~7 wt.%) and bipyramidal crystal morphology that is typically observed for beta zeolites synthesized in a fluoride medium [22]. The obtained zeolite was characterized using various analytical techniques such as diffuse reflectance ultraviolet-visible (UV-Vis) absorption

spectroscopy, electron paramagnetic resonance (EPR) spectroscopy, and X-ray absorption fine structure (XAFS) spectroscopy. To gain further insights into the application of this material as a catalyst and adsorbent, its hydrothermal stability, NH_3-SCR activity, and dynamic toluene adsorption-desorption behavior were investigated.

2. **Experimental**

2.1. Synthesis of Fe-BEA zeolites

Fe-BEA zeolites were synthesized as follows. Sodium silicate (SiO_2 30 wt.%, Na_2O 9.1 wt.%, Al_2O_3 0.01 wt.%, Fuji Chemical), sulfuric acid (98 wt.%, Kishida Chemical Co., Ltd.), deionized water, and $Fe(NO_3)_3 \cdot 9H_2O$ (Kishida Chemical Co., Ltd.) were used to prepare the precursor gel. A diluted sodium silicate solution (ca. 14 wt.% SiO_2) and an aqueous solution of $Fe(NO_3)_3$ with sulfuric acid were mixed dropwise in deionized water under vigorous stirring to promote the dispersion of Fe atoms in the precursor gel. After the gel was filtered and washed with deionized water, an aqueous solution of TEAOH (35 wt.%, Sachem), sodium hydroxide (48 wt.%, Kaname Chemicals Co., Ltd.), deionized water, and commercial beta seeds (1 wt.% of the total solid, HSZ-940NHA (SiO_2/Al_2O_3 ratio of 38), Tosoh Corporation) were added to the gel under vigorous stirring. The representative molar composition of the obtained hydrogel was 65 SiO_2 : Fe_2O_3 : 13 Na_2O : 9.8 TEAOH : 650 H_2O. The hydrogel was transferred into a Teflon-sealed stainless steel autoclave (80 ml) and heated at 150 or 170 °C under rotation. After the reaction was complete, the solid was filtered, washed, dried at 110 °C overnight, and finally calcined in air at 600 °C for 2 h to remove TEA cations occupying

zeolite pores. Prior to catalytic tests, the Na cations in the calcined zeolite were exchanged with NH_4^+ in an aqueous solution of NH_4Cl (~20 wt.%) at 40 °C for 0.5 h. The ion-exchange was repeated three times, furnishing the NH_4^+-form zeolite.

For comparison, the synthesis of Fe-BEA zeolites in a fluoride medium (Fe-BEA-F) was also carried out, according to procedures described in literature [17]. $Fe(NO_3)_3 \cdot 9H_2O$ was added to an aqueous solution of 35 wt.% TEAOH, and the mixture stirred until the solids completely dissolved. Then, tetraethylorthosilicate (TEOS, 98 wt.%, Kishida Chemical Co., Ltd.) was added to the above solution under stirring at room temperature. After the complete hydrolysis of TEOS, the generated ethanol was removed by evaporation. Finally, an aqueous HF solution (47 wt.%, Hirota Chemical Industry Co., Ltd.) was dropwise added, and the resulting hydrogel, with a molar composition corresponding to 88 SiO_2 : Fe_2O_3 : 53.7 TEAOH : 44 HF : 660 H_2O, was homogenized in a mortar. The above hydrogel was heated at 150 °C under static conditions in a Teflon-sealed stainless steel autoclave (80 ml). After crystallization was complete, the solid was filtered, washed, and dried overnight at 110 °C.

2.2. Preparation of Fe-loaded beta and Fe-loaded ZSM-5 zeolites

Conventional Fe-loaded beta and Fe-loaded ZSM-5 zeolites were prepared by an incipient wetness impregnation method. A commercial beta zeolite (Tosoh Corporation, SiO_2/Al_2O_3 ratio of 28) and a ZSM-5 zeolite (Tosoh Corporation, SiO_2/Al_2O_3 ratio of 40) were used as catalyst supports. An aqueous solution of $Fe(NO_3)_3$ was prepared, with its volume equaling the micropore volume of the zeolite support. This solution was used to treat the zeolites, and the obtained wet powders were mixed to

homogeneity and dried overnight at 110 °C. The obtained solid products were calcined in air at 500 °C for 2 h, yielding Fe-loaded beta and Fe-loaded ZSM-5 zeolites with Fe contents of 3.2 and 2.5 wt.%, respectively.

2.3. Characterization

Powder X-ray diffraction (XRD) patterns were recorded on a diffractometer (X'pert PRO MPD, Spectris, Japan) using Cu K_α radiation and a scanning range (2θ) of 3–43°. Elemental analysis was carried out by inductively coupled plasma atomic emission spectroscopy (ICP-AES) (OPTIMA 3000 DV, Perkin Elmer), and crystal morphology was characterized by scanning electron microscopy (SEM; JSM-6390LV, JEOL). UV-Vis spectra were recorded on a diffuse reflectance UV-Vis spectrometer (UV-Vis 3100, Shimadzu, Japan) in the range of 220–700 nm using $BaSO_4$ as a blank and subjected to the Kubelka-Munk (K-M) conversion. EPR spectra were recorded at –196 °C on a JES-TE200 instrument (JEOL, Japan) operating in the X-band frequency (9.4 GHz). Fe *K*-edge XAFS spectra were measured at BL15 (SAGA-LS, Tosu, Japan) in transmission mode at room temperature, employing a double-crystal Si (111) monochromator. Fe_2O_3 (hematite) and $FePO_4$ (redolicoite) were used as references.

To assess the long-term hydrothermal durability of zeolites, they were hydrothermally treated at 850, 900, and 1000 °C for 5 h in a stream of gas containing 10 vol.% H_2O and 90 vol.% air with a gas hourly space velocity (GHSV) of 6000 h^{-1} (300 ml/min flow, 3 ml of catalyst). The durability of the catalyst in the NH_3-SCR reaction was evaluated by hydrothermal treatment at 700 °C for 20 h. Micropore volumes of samples were calculated by the t-plot method based on nitrogen adsorption isotherms

measured at –196 °C using a volumetric apparatus (BELSORP-max, MicrotracBEL Corp., Japan). Prior to measurements, samples (~0.05 g) were kept under vacuum at 350 °C for 2 h.

The NH_3-SCR reaction was performed in a fixed-bed flow reactor under atmospheric pressure between 150 and 500 °C. The catalyst was pelletized, crushed, and sieved to 0.85–1.4 mm, and 1.5 ml of the sieved sample was placed in a quartz tube. The composition of the used gas corresponded to 200 ppm NO, 200 ppm NH_3, 10 vol.% O_2, 3 vol.% H_2O, and N_2 as balance. The total flow rate was set to 1.5 L min^{-1}, and the GHSV was set to 60000 h^{-1}. During the experiments, the temperature was lowered from 500 to 150 °C in steps of ~50 °C, and the NO_x conversion was calculated as follows:

$$NO_x \text{ conversion } (\%) = \frac{NO_{in} - NO_{out} - NO_{2out}}{NO_{in}} \times 100\%$$

where NO_{in} represents the NO inlet concentration (200 ppm), and NO_{out} and NO_{2out} represent the NO and NO_2 outlet concentrations, respectively. To evaluate steady-state catalytic activity, the outlet concentrations of NH_3, NO, and NO_2 after 10 min of time-on-stream at each reaction temperature were analyzed by an FT-IR spectrometer (FT/IR-6100, JASCO, Japan) equipped with a gas cell (LPC-12M-S, 12 m) and a mercury cadmium telluride detector cooled by liquid nitrogen. The concentrations of NH_3, NO, and NO_2 were determined based on the intensities of their peaks at 1033, 1875, and 2917 cm^{-1}, respectively. Averaging over 30 scans was performed for each normalized spectrum.

Dynamic adsorption-desorption of toluene was characterized in a fixed-bed flow reactor under atmospheric pressure, similarly to the NH_3-SCR reaction. The

sample was pelletized, crushed, and sieved to 0.85–1.4 mm, and 0.10 g of the sieved sample was placed in a quartz tube. The used gas stream contained 3000 ppm toluene (carbon basis), 3 vol.% H_2O, and N_2 as balance. After pre-treatment in a flow of N_2 at 500 °C for 1 h and cooling to 50 °C, the temperature was linearly increased to 600 °C at 10 °C min^{-1}, with the model gas flow equaling 200 ml min^{-1}. The concentration of hydrocarbons in the outlet gas was continuously measured using a flame ionization detector. The amount of adsorbed toluene was calculated from the difference in the concentration between the outlet gas and the bypass flow (3000 ppm, carbon basis).

3. **Results and discussion**

3.1. Synthesis and characterization of Fe-BEA zeolites

Table 4-1 summarizes the hydrothermal synthesis conditions and the characteristics of obtained products. Pure *BEA phase was obtained only for starting hydrogel OH^-/SiO_2 ratios above 0.50. The influence of this ratio on the relative crystallinity of Fe-BEA zeolites, as determined from the XRD peak intensity at 2θ = 22.4°, is shown in Figure 4-1, where the peak intensity of sample 9 is set to 100%. When crystallization was performed at 150 °C, the product obtained at an OH^-/SiO_2 ratio of 0.50 was amorphous. However, a highly crystalline Fe-BEA zeolite was obtained at a ratio of 0.55, corresponding to maximum relative crystallinity (sample 6), whereas the crystallinity decreased as the OH^-/SiO_2 ratio was increased to 0.60 (sample 7). This suggests that the crystallization conditions of the Fe-BEA zeolite in this system are fairly limited. On the other hand, a similar OH^-/SiO_2 ratio dependence was observed for treatment at 170 °C utilizing 1 wt.% seeds and a lower TEA^+/SiO_2 ratio. However,

the pure *BEA phase was observed even at an OH^-/SiO_2 ratio of 0.60 (sample 10). It is interesting that a similar high OH^-/SiO_2 ratio in the starting gel is required for syntheses of Ti-beta [23] (TEAOH/(SiO_2 + TiO_2) = 0.50–0.54), Sn-beta [24] (TEAOH/(SiO_2 + SnO_2) = 0.50), and OSDA-free beta [25] (NaOH/SiO_2 = 0.48–0.60). Taking into account the fact that the conventional Al-beta can be synthesized without such high OH^-/SiO_2, the high OH^-/SiO_2 ratio may be a critical factor for the crystal growth of these zeolites including Fe-BEA. The XRD patterns of Fe-BEA (sample 9) and Fe-BEA-F (sample 11) zeolites are shown in Figure 4-2. In general, zeolites synthesized in a fluoride medium exhibit less defects and larger crystal sizes, showing very sharp and strong XRD peaks [22,26]. The peak intensity of the Fe-BEA zeolite was comparable to that of the Fe-BEA-F zeolite, even though the former was synthesized in a hydroxide medium. The full width at half maximum (FWHM) of the peak at 2θ = 22.4° equaled 0.18° for samples 9 and 11. The SiO_2/Fe_2O_3 ratios of the obtained Fe-BEA zeolites equaled 22–25, corresponding to 7.5–6.7 wt.% Fe. Despite the large amount of Fe, the zeolite powder was white, suggesting that Fe atoms were successfully incorporated into the zeolite framework. The amount of Fe incorporated in the zeolite framework is influenced by the framework structure and the synthesis condition. Shamzhy et al. succeeded in synthesizing Fe-substituted UTL zeolite. However, the color of the obtained zeolite was not white but brown when an excess amount of Fe was used in the starting gel ((SiO_2 + GeO_2)/Fe_2O_3 ratio < 65) [27]. Figure 4-3 shows the SEM images of both samples, with the Fe-BEA zeolite exhibiting a truncated square bipyramidal crystal shape that is typically observed for beta zeolites synthesized in fluoride media, as exemplified by the Fe-BEA-F zeolite. This morphology can also be observed for beta zeolites synthesized

in the absence of an OSDA [25].

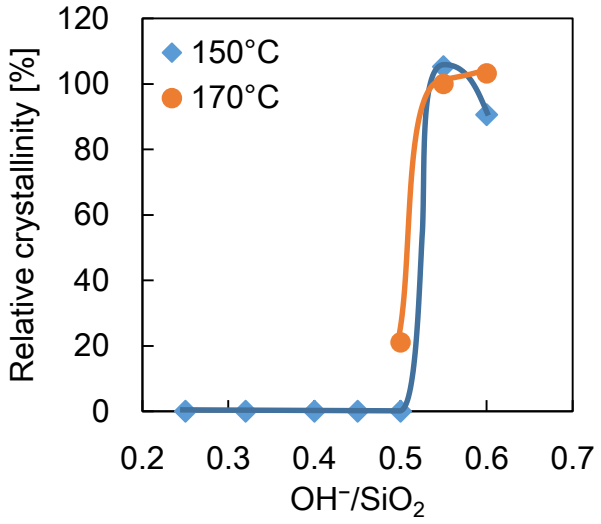

Figure 4-1 Influence of the OH^-/SiO_2 ratio of the starting hydrogel on the relative crystallinity of Fe-BEA zeolites prepared at ◆ 150 °C and ● 170 °C.

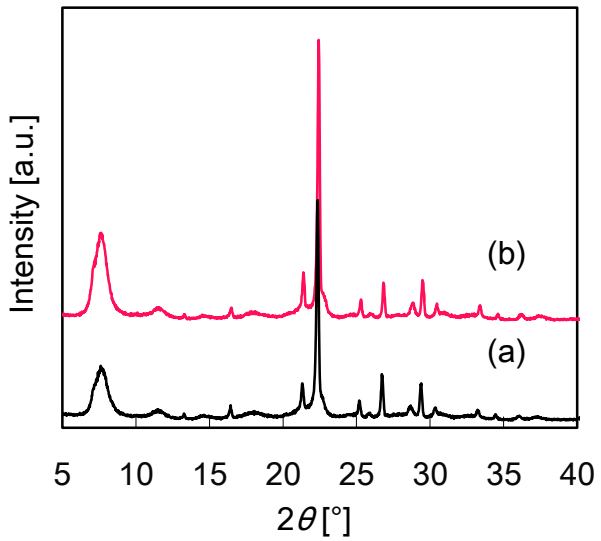

Figure 4-2 XRD patterns of (a) sample 9 (Fe-BEA) and (b) sample 11 (Fe-BEA-F).

Table 4-1. Hydrothermal synthesis conditions and characteristics of Fe-based BEA zeolites.

Sample	Synthesis condition									Product				
	SiO_2 /Fe_2O_3	H_2O /SiO_2	TEA^+ /SiO_2	Na^+ /SiO_2	OH^- /SiO_2	F^- /SiO_2	Seed [wt.%]	Temp. [°C]	Time [h]	Phase[a]	SiO_2 /Al_2O_3[b]	SiO_2 /Fe_2O_3[b]	Fe [wt. %][b]	Micropore volume [cm^3/g][c]
1	65	10	0.20	0.05	0.25	0	0	150	90	Am				
2	65	10	0.20	0.12	0.32	0	0	150	90	Am				
3	65	10	0.20	0.20	0.40	0	0	150	90	Am				
4	65	10	0.20	0.25	0.45	0	0	150	90	Am				
5	65	10	0.20	0.30	0.50	0	0	150	90	Am				
6	65	10	0.20	0.35	0.55	0	0	150	90	*BEA	880	25	6.7	
7	65	10	0.20	0.40	0.60	0	0	150	90	*BEA + Am				
8	65	10	0.15	0.35	0.50	0	1	170	90	MTW + *BEA	1500	36	4.8	
9	65	10	0.15	0.40	0.55	0	1	170	90	*BEA	1100	23	7.3	0.24
10	65	10	0.15	0.45	0.60	0	1	170	90	*BEA	1000	22	7.5	
11(Fe-BEA-F)	88	7.5	0.61	0	0.11	0.50	0	150	240	*BEA	4800	62	2.9	0.22

[a] Am: amorphous

[b] Measured by ICP.

[c] Calculated by the t-plot method.

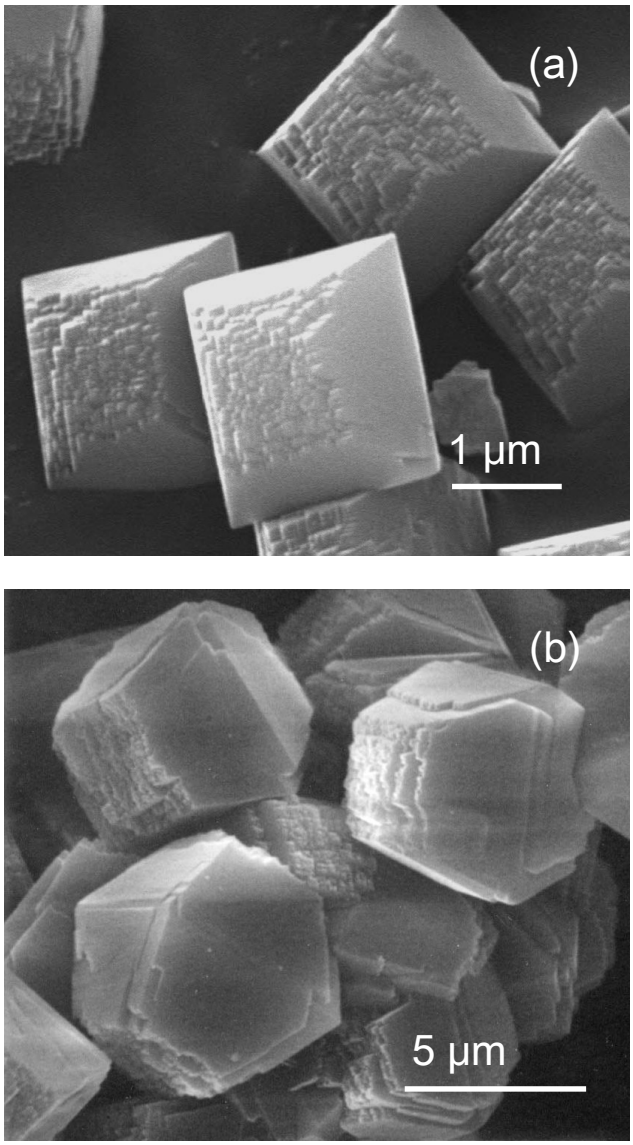

Figure 4-3 SEM images of (a) sample 9 (Fe-BEA) and (b) sample 11 (Fe-BEA-F).

Next, the chemical states of Fe present in Fe-BEA zeolites were investigated to understand whether the Fe-BEA zeolites synthesized in hydroxide and fluoride media exhibit any differences. The Fe-BEA-F zeolite has already been extensively characterized by various methods (including UV-Vis and EPR) in Chapter 3 [18]. In the present study, I additionally performed XAFS measurements to directly analyze

tetrahedrally coordinated Fe^{3+} and emphasize the comparison of zeolites synthesized in hydroxide and fluoride media.

The existence of tetrahedral Fe^{3+} in the zeolite framework of the as-prepared (not calcined) sample was first confirmed by measuring absorption in the *d-d* transition region of its UV-Vis spectrum (Figure 4-4). The Fe-BEA zeolite showed four absorption peaks at 375, 414, 439, and 479 nm, which were well consistent with the results of Goldfarb et al. [28]. who reported that an Fe-substituted SOD zeolite showed four absorption peaks at 373, 410, 436, and 480 nm, indicating the presence of tetrahedrally coordinated Fe^{3+}. Unfortunately, this technique cannot be applied to calcined samples, because the signal intensity of *d-d* transitions is much weaker than that of CT transitions, mostly being masked. Figure 4-5 shows the diffuse reflectance UV-Vis spectra of Fe-BEA (sample 9) and Fe-BEA-F (sample 11) zeolites before and after hydrothermal treatment at 700 °C for 20 h. As Fe species with different dispersion states (isolated Fe^{3+}, $Fe^{3+}_xO_y$ clusters, and Fe_2O_3 particles) exhibited different absorption subbands in their UV-Vis spectra, the dispersion state of Fe in zeolites could be quantitatively analyzed by deconvoluting absorption curves [18,29,30], with the relative amounts of Fe species calculated in this way summarized in Table 4-2, where the absorption subbands of < 300 nm, 300–400 nm, and > 400 nm were regarded as isolated Fe^{3+}, $Fe^{3+}_xO_y$ clusters, and Fe_2O_3 particles, respectively [18,29,30]. Gaussian curve was assumed for deconvolution in Figure 4-5, with two deconvoluted absorption curves corresponding to each subband. A more detailed description of this technique can be found elsewhere [31-33]. The Fe-BEA zeolite retained more than 95% of Fe as isolated Fe^{3+} in its fresh (calcined)

state, whereas the corresponding value of the Fe-BEA-F zeolite was 89.5%. The latter zeolite exhibited more intense subbands in the 300–400 nm region compared to its Fe-BEA counterpart (Figure 4-5 (a) and (b)). Surprisingly, the Fe-BEA zeolite retained a higher fraction of isolated Fe^{3+} than its Fe-BEA-F counterpart, despite containing more than twice as much Fe. After aging at 700 °C, both samples showed similar spectra, indicating similar dispersion states of Fe species.

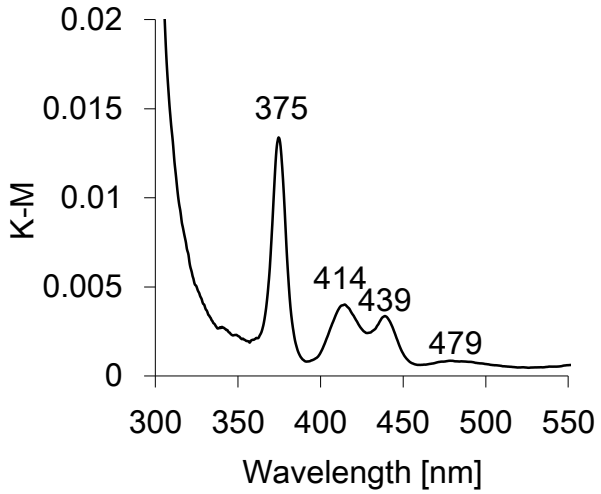

Figure 4-4 Diffuse reflectance UV-Vis spectrum of the as-prepared Fe-BEA (sample 9) in the *d-d* transition region.

Table 4-2. Fractions of Fe species calculated from deconvoluted UV-Vis subbands.

Sample		Isolated Fe^{3+} [%][a]	$Fe^{3+}{}_xO_y$ clusters [%][a]	Fe_2O_3 particles [%][a]
9 (Fe-BEA)	fresh	95.8	4.1	0.1
	aged	61.4	32.6	6.0
11 (Fe-BEA-F)	fresh	89.5	9.9	0.5
	aged	58.9	34.1	7.0

[a] Calculated from integrated subbands.
Isolated Fe^{3+}: $\lambda < 300$ nm
$Fe^{3+}{}_xO_y$ clusters: 300 nm < λ < 400 nm
Fe_2O_3 particles: $\lambda > 400$ nm

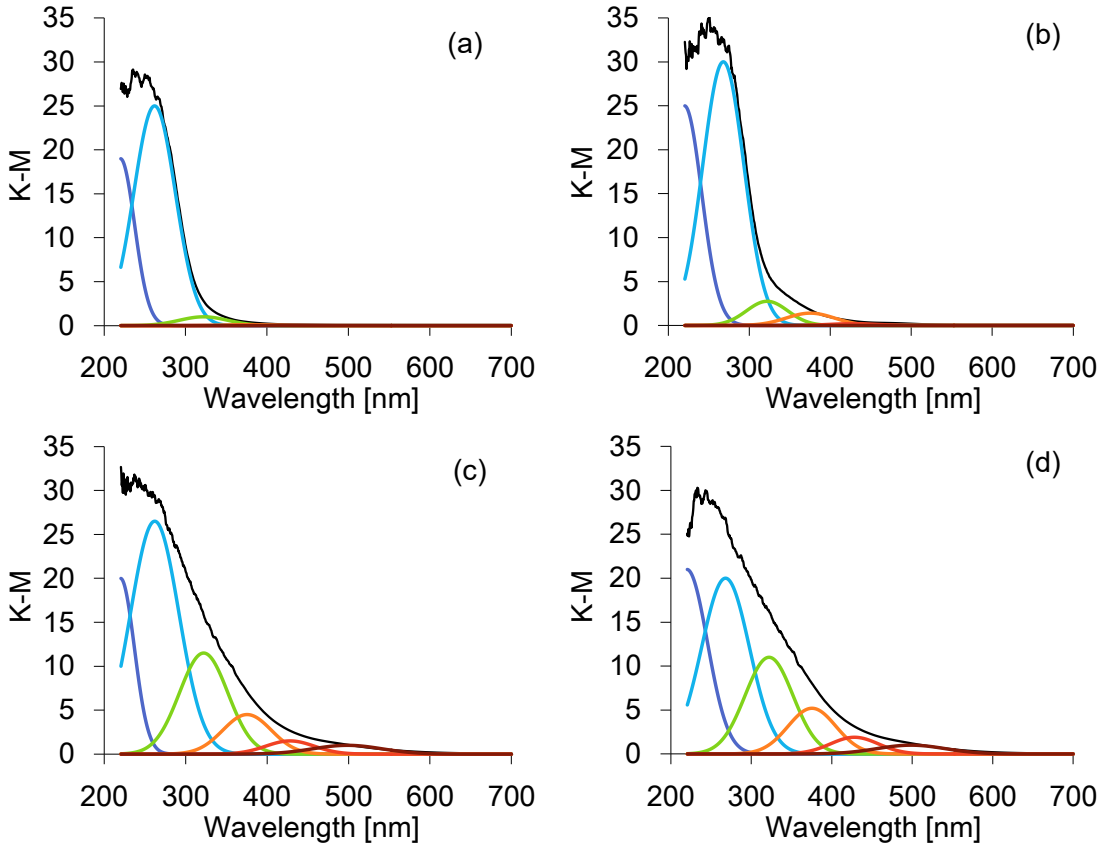

Figure 4-5 Diffuse reflectance UV-Vis spectra of Fe-BEA (sample 9) and Fe-BEA-F (sample 11) before and after hydrothermal treatment at 700 °C for 20 h. (a) Fe-BEA (fresh), (b) Fe-BEA-F (fresh), (c) Fe-BEA (aged), and (d) Fe-BEA-F (aged).

EPR technique is frequently used to analyze the symmetry of Fe^{3+} environments in zeolites, together with UV-Vis spectroscopy [28-32]. For Fe-containing zeolites, several signals are generally observed at $g \approx 2.0$, $g \approx 4.3$, and $g \geq 4.3$. In Chapter 3, an Al-free Fe-BEA-F zeolite exhibited a strong signal at $g \approx 2.0$, which was retained after hydrothermal treatment and was attributed to isolated Fe^{3+} in a highly symmetric environment (tetrahedral Fe^{3+} in the framework or tetrahedral/octahedral Fe^{3+} partially connected to the framework) [18]. The signal at $g \approx 4.3$ was assigned to distorted Fe^{3+} species occupying ion-exchange sites. Figure 4-6 shows the EPR spectra

of Fe-BEA and Fe-BEA-F zeolites recorded at –196 °C before and after hydrothermal treatment at 700 °C for 20 h. The Fe-BEA zeolite had a very strong signal at $g \approx 2.0$, similarly to the Fe-BEA-F zeolite, retaining a high peak intensity after hydrothermal treatment. This result supports my proposed mechanism, in which the detachment of Fe^{3+} from the zeolite framework is suppressed at Fe/Al molar ratios greater than unity due to the decreased acidity of Al sites. Moreover, this mechanism can operate regardless of the preparation method of Fe-BEA zeolites.

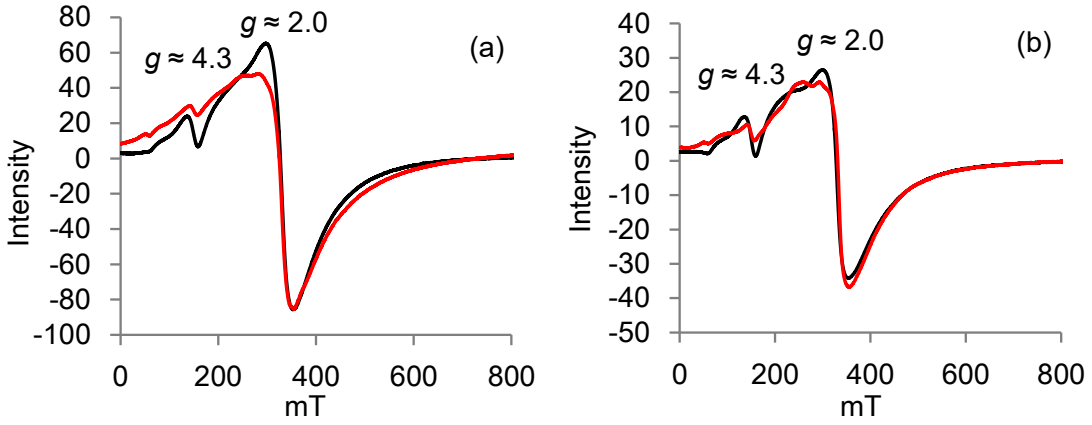

Figure 4-6 EPR spectra recorded at –196 °C for (a) Fe-BEA (sample 9) and (b) Fe-BEA-F (sample 11) before (black) and after (red) hydrothermal treatment at 700 °C for 20 h.

The above UV-Vis and EPR spectra provided me with useful information concerning the chemical states of Fe species in Fe-BEA zeolites. However, since the coordination state of Fe^{3+} was still ambiguous, XAFS measurements were additionally carried out. For Fe *K*-edge XAFS spectra, a pre-edge peak, providing information on the local structure of Fe species, was observed at the lower energy side. The intensity of this

peak is known to be high for tetrahedrally coordinated Fe and low for octahedrally coordinated Fe [34]. Figure 4-7 shows pre-edge peaks of Fe-BEA (sample 9) and Fe-BEA-F (sample 11) zeolites in their Fe *K*-edge XAFS spectra, with Fe_2O_3 and $FePO_4$ used as references for octahedrally and tetrahedrally coordinated Fe^{3+}, respectively. All spectra were normalized with respect to the intensity of the Fe *K*-edge peak (Fe concentration). The valence state of Fe in these samples was determined as Fe^{3+}, since the *K*-edge energies of all samples equaled ~7125 eV. $FePO_4$ (tetrahedral Fe^{3+}) showed a large pre-edge peak at 7113 eV, whereas that of Fe_2O_3 (octahedral Fe^{3+}) was relatively small, indicating different Fe^{3+} coordination environments. Fe_2O_3 showed weak absorption around 7116 eV between the pre-edge and *K*-edge peaks. Takahashi et al. presumed that the intensity in the region from 7114 to 7120 eV, characterized by tailing of the Fe *K*-edge, reflects Fe-Fe interactions between Fe species and can be used to quantitatively evaluate the dispersion of Fe in zeolites [35,36]. The large pre-edge peaks observed for both as-prepared samples (confirmed to have tetrahedrally coordinated Fe^{3+} by UV-Vis) are shown in Figure 4-7 (a) and (b) together with the data for $FePO_4$, indicating that the Fe species in these samples mostly correspond to tetrahedrally coordinated Fe^{3+}. The larger pre-edge peak of as-prepared samples compared to that of $FePO_4$ might imply that the Fe species in the former are in a highly symmetric Td state. The pre-edge peak intensity decreased for fresh (calcined) samples, but was still larger than that of Fe_2O_3, suggesting that a part of tetrahedrally coordinated Fe^{3+} (59–66%) was still preserved. Interestingly, the pre-edge peak height of the aged sample did not change after hydrothermal treatment, with the peak intensity in the 7114–7120 eV

region (reflecting Fe-Fe interactions between Fe species) increasing instead. This strongly suggests that the additional detachment of framework Fe^{3+} was suppressed, and the non-framework Fe^{3+} already detached by the first calcination underwent agglomeration during aging. Table 4-3 lists the relative amounts of tetrahedrally coordinated Fe^{3+} in Fe-BEA and Fe-BEA-F zeolites based on pre-edge peak area, assuming a value of 100% for the as-prepared sample and 0% for Fe_2O_3.

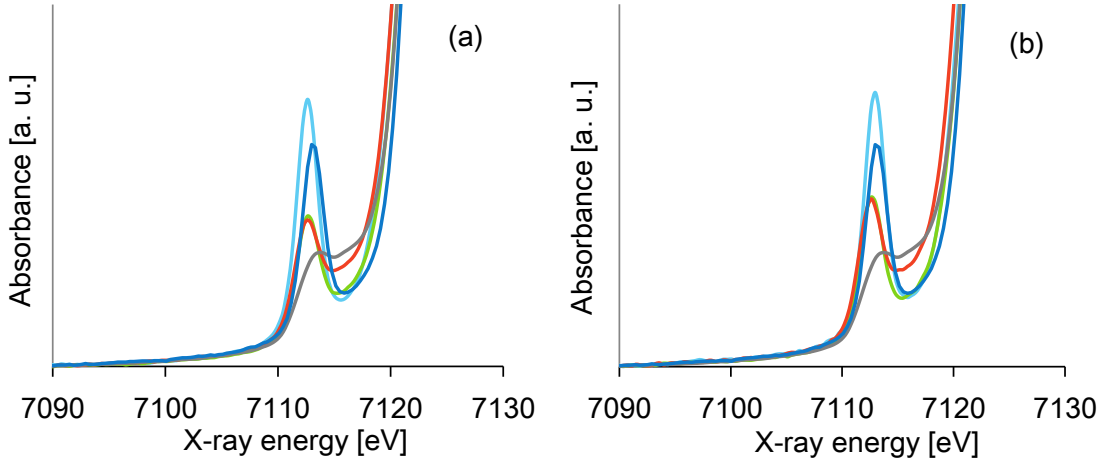

Figure 4-7 Comparison of pre-edge peaks in XAFS spectra of (a) Fe-BEA (sample 9) and (b) Fe-BEA-F (sample 11). Light blue, as-prepared; green, fresh; red, aged; grey, Fe_2O_3; and blue, $FePO_4$.

Table 4-3. Fractions of tetrahedrally coordinated Fe^{3+} calculated from XAFS spectra.

Sample	Tetrahedrally coordinated Fe^{3+} [%]		
	As-prepared	Fresh (calcined)	Aged
9 (Fe-BEA)	100	59	53
11 (Fe-BEA-F)	100	66	63

3.2. Hydrothermal stability

The hydrothermal stability of zeolites is an important factor for various applications, particularly for automobile catalysts and adsorbents used in a

moisture-rich atmosphere. The small XRD peak FWHM values and the well-facetted crystal morphology of Fe-BEA zeolites suggest that they can exhibit excellent hydrothermal stability. Figure 4-8 shows the micropore volume of the Fe-BEA zeolite (sample 9) after various hydrothermal treatments. Even after treatment at 1000 °C for 5 h, the Fe-BEA zeolite maintained more than 88% of its micropore volume, indicating high hydrothermal stability.

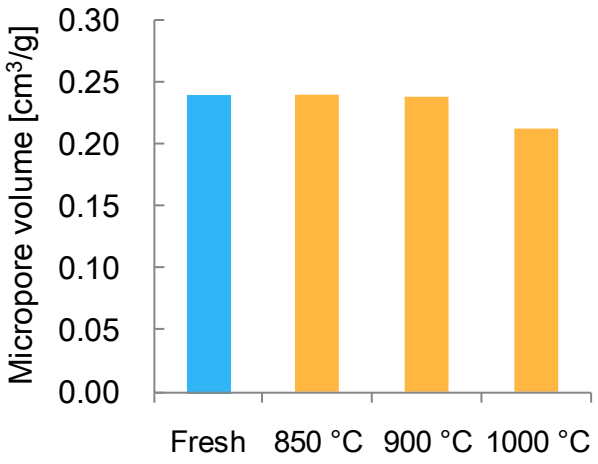

Figure 4-8 Micropore volume of the Fe-BEA zeolite (sample 9) before and after hydrothermal treatment at various temperatures for 5 h.

3.3. NH_3-SCR activity

The NH_3-SCR catalytic activities of Fe-BEA (sample 9), Fe-BEA-F (sample 11) and Fe-loaded zeolites are compared in Figure 4-9. Surprisingly, the fresh Fe-BEA zeolite exhibited better NO_x conversion over the whole temperature range than the Fe-BEA-F zeolite, despite the absence of major differences between the chemical states of Fe in both samples (see Section 3.1). The high content of Fe^{3+} (7.3 wt.%) and the large fraction of isolated Fe^{3+} in the Fe-BEA catalyst probably contributed to its greater catalytic activity. The incorporation of such large amounts of well-dispersed Fe^{3+} into

zeolites can only be achieved by isomorphous substitution, because Fe^{3+} ions incorporated in the Fe-BEA zeolite above a certain ion-exchange capacity easily undergo agglomeration. After hydrothermal treatment at 700 °C for 20 h, the Fe-BEA zeolite still showed higher activity than its Fe-BEA-F counterpart, being obviously superior to conventional Fe-loaded beta and ZSM-5 zeolites, particularly in the low-temperature region (150–250 °C).

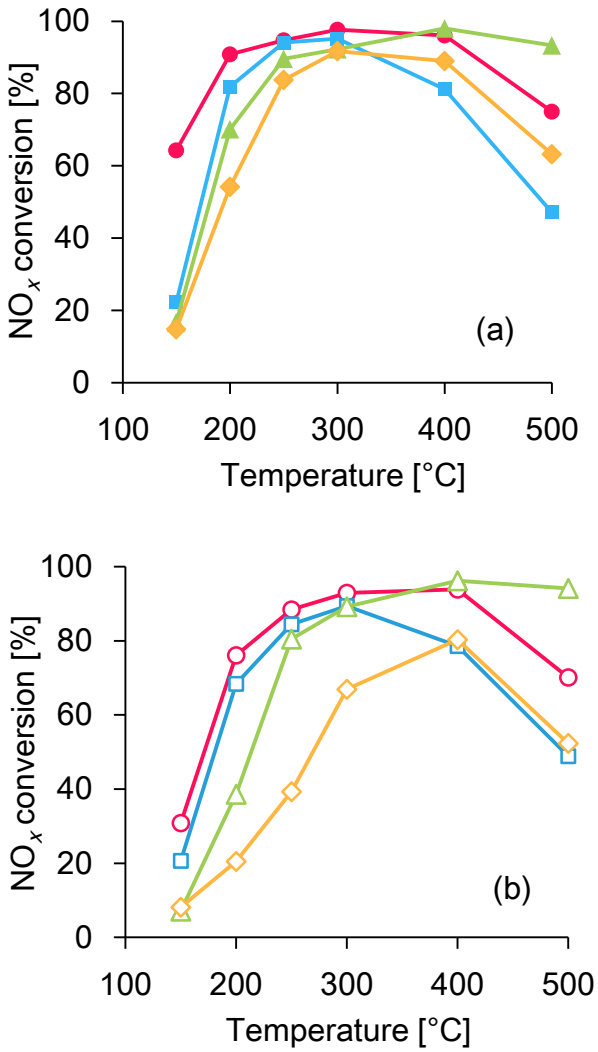

Figure 4-9 NO_x conversion on various zeolite catalysts (a) before and (b) after hydrothermal treatment at 700 °C for 20 h. Red circles, Fe-BEA (sample 9); blue squares, Fe-BEA-F (sample 11); green triangles, Fe-loaded beta zeolite; and orange diamonds, Fe-loaded ZSM-5.

3.4. Dynamic adsorption-desorption of toluene

Hydrocarbon adsorption-desorption characteristics are important for the use of zeolites as diesel oxidation catalysts and hydrocarbon traps for cold-start emission control. Toluene is a major hydrocarbon component of gasoline engine emissions. Figure 4-10 and Table 4-4 show the results of dynamic toluene adsorption-desorption measurements for the Fe-BEA zeolite (sample 9), with a commercial beta zeolite (SiO_2/Al_2O_3 ratio of 38, Tosoh Corporation) also characterized for comparison. The measurement performed in the present study was designed to evaluate the adsorption-desorption behavior in an environment close to the actual cold-start environment in automobiles. In a typical measurement, adsorption initially occurs at low temperature, followed by desorption as the temperature increases. If the hydrocarbons do not undergo any reactions on zeolites, their adsorbed and desorbed amounts should be the same. However, the amount of hydrocarbons desorbed from the Fe-BEA zeolite was reduced to 66% of the adsorbed quantity, whereas that of adsorbed hydrocarbons was almost the same as for the beta zeolite. Ogura et al. proposed their "hydrocarbon reformer trap" concept based on the results obtained for an Fe ion-exchanged beta zeolite able to retain hydrocarbons at higher temperatures than H-beta and oxidize them in an oxygen-containing gas stream [37,38]. Taking into account the facts that no oxygen was present in my gas stream and no coke deposition in the used Fe-BEA zeolite was detected by thermogravimetric and differential thermal analysis measurements, the obtained results suggest that toluene was probably oxidized by oxygen stored in $Fe^{3+}{}_xO_y$ clusters or Fe_2O_3 within the Fe-BEA zeolite. The above

concept is similar to the one proposed by Yang et al., who used zeolites and metal oxides for adsorption and oxidation of hydrocarbons, respectively [39]. Since the Fe-BEA zeolite prepared in this study exhibited toluene adsorption and oxidation by one material and high hydrothermal stability, it is a promising automobile hydrocarbon adsorbent. However, my investigation of the adsorption and oxidation of hydrocarbons on Fe-BEA zeolites is currently quite limited, with a further study in progress to clarify the high potential of Fe-based BEA zeolites.

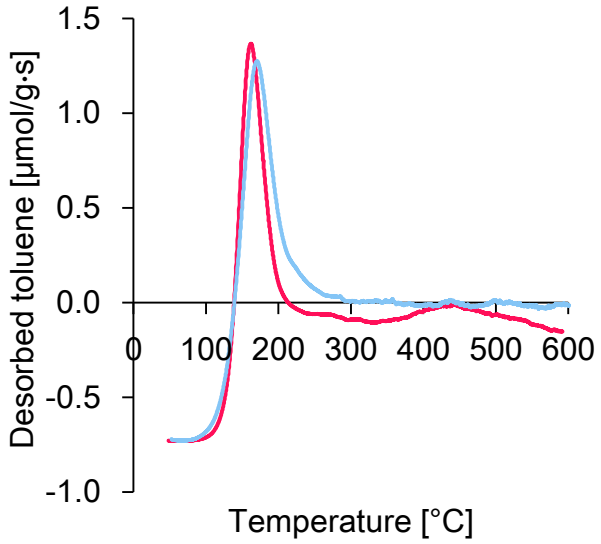

Figure 4-10 Dynamic adsorption-desorption curves of fresh Fe-BEA (sample 9, red) and commercial beta zeolites (SiO_2/Al_2O_3 = 38, blue).

Table 4-4. Amounts of adsorbed and desorbed toluene calculated by dynamic adsorption-desorption measurements.

Sample	Amount of toluene [µmol/g]			
	Adsorbed	Desorbed	Adsorbed – Desorbed	Oxidized[a]
9 (Fe-BEA, fresh)	326	215 (66%[b])	111	175
Beta (fresh)	299	288 (96%[b])	11	16

[a] Calculated from the negative amounts of toluene desorbed above 200 °C in dynamic adsorption-desorption curves.
[b] Based on the amount of adsorbed toluene.

4. **Conclusions**

A highly crystalline and Fe-rich (~7 wt.%) isomorphously substituted Al-free Fe-BEA zeolite was synthesized. The synthetic range of the *BEA phase in this study was very narrow ($OH^-/SiO_2 > 0.50$). An excess of NaOH was used instead of TEAOH as an alkali source (e.g., $NaOH/SiO_2$ ratio of 0.40 and $TEAOH/SiO_2$ ratio of 0.15). The obtained Fe-BEA zeolite showed excellent hydrothermal stability, retaining more than 88% of its micropore volume after aging at 1000 °C. The chemical state of Fe species in the Fe-BEA zeolite was similar to that of the one synthesized in a fluoride medium (Fe-BEA-F). Considering its high Fe content, it was surprising that the Fe-BEA zeolite contained above 90% of Fe as isolated Fe^{3+}. XAFS measurements revealed that the Fe-BEA zeolite retained 53% of tetrahedrally coordinated Fe^{3+} after hydrothermal treatment at 700 °C for 20 h. The Fe-BEA zeolite exhibited greater catalytic activity than the Fe-BEA-F zeolite in the NH_3-SCR reaction. The larger amount of isolated Fe^{3+} in the former zeolite is thought to contribute to its high performance. Dynamic adsorption-desorption measurements showed that only 66% of the adsorbed toluene was desorbed from the Fe-BEA zeolite (96% for beta zeolite), although the gas stream did not contain oxygen, suggesting that the hydrocarbons were oxidized by oxygen stored in the Fe-BEA zeolite. With these results, the Fe-rich Fe-BEA zeolite synthesized in a hydroxide medium is expected to be useful for various automotive applications.

References

[1] M. Watanabe, H. Uchida, K. Ohkubo, and H. Igarashi, Appl. Catal. B Environ. 46, 595 **(2003)**.

[2] G. I. Panov, G. A. Sheveleva, A. S. Kharitonov, V. N. Romannikov, and L. A. Vostrikova, Appl. Catal. A Gen. 82, 31 **(1992)**.

[3] C. D. Chang, W. H. Lang, and A. J. Silvestri, J. Catal. 56, 268 **(1979)**.

[4] H. Kušić, N. Koprivanac, and I. Selanec, Chemosphere 65, 65 **(2006)**.

[5] N. Herron and C. A. Tolman, J. Am. Chem. Soc. 109, 2837 **(1987)**.

[6] I. Nova and E. Tronconi, *Urea-SCR Technology for deNOx After Treatment of Diesel Exhausts*, Springer-Verlag New York **(2014)**.

[7] S. Brandenberger, O. Kröcher, A. Tissler, and R. Althoff, Catal. Rev. 50, 492 **(2008)**.

[8] T. J. Toops, K. Nguyen, A. L. Foster, B. G. Bunting, N. A. Ottinger, J. A. Pihl, E. W. Hagaman, and J. Jiao, Catal. Today 151, 257 **(2010)**.

[9] H. Y. Huang, R. Q. Long, and R. T. Yang, Appl. Catal. A Gen. 235, 241 **(2002)**.

[10] P. Balle, B. Geiger, and S. Kureti, Appl. Catal. B Environ. 85, 109 **(2009)**.

[11] D. W. Fickel, E. D'Addio, J. A. Lauterbach, and R. F. Lobo, Appl. Catal. B Environ. 102, 441 **(2011)**.

[12] M. Moliner, C. Franch, E. Palomares, M. Grill, and A. Corma, Chem. Commun. 48, 8264 **(2012)**.

[13] T. Sonoda, T. Maruo, Y. Yamasaki, N. Tsunoji, Y. Takamitsu, M. Sadakane, and T. Sano, J. Mater. Chem. A 3, 857 **(2015)**.

[14] M. Koebel, G. Madia, and M. Elsener, Catal. Today 73, 239 **(2002)**.

[15] C. T. W. Chu and C. D. Chang, J. Phys. Chem. 89, 1569 **(1985)**.

[16] J. Čejka, A. Vondrová, B. Wichterlová, G. Vorbeck, and R. Fricke, Zeolites 14, 147 **(1994)**.

[17] Y. Naraki, K. Ariga, and T. Sano, Adv. Porous Mater. 4, 125 **(2016)**.

[18] Y. Naraki, K. Ariga, H. Oka, H. Kurashige, and T. Sano, Adv. Porous Mater. 4, 91 **(2016)**.

[19] R. Kumar, A. Thangaraj, R. N. Bhat, and P. Ratnasamy, Zeolites 10, 85 **(1990)**.

[20] R. B. Borade and A. Clearfield, Microporous Mater. 2, 167 **(1994)**.

[21] A. Raj, S. Sivasanker, and K. Lazar, J. Catal. 147, 207 **(1994)**.

[22] P. Caullet, J. Hazm, J.L. Guth, J.F. Joly, J. Lynch, and F. Raatz, Zeolites 12 240 **(1992)**.

[23] M. A. Camblor, A. Corma, and J. Pérez-Pariente, Zeolites 13, 82 **(1993)**.

[24] C. Chang, H. J. Cho, Z. Wang, X. Wang, and W. Fan, Green Chem. 17, 2943 **(2015)**.

[25] Y. Kamimura, W. Chaikittisilp, K. Itabashi, A. Shimojima, and T. Okubo, Chem. Asian J. 5, 2182 **(2010)**.

[26] M. A. Camblor, A. Corma, and S. Valencia, J. Mater. Chem. 8, 2137 **(1998)**.

[27] M. V Shamzhy, O. V Shvets, M. V Opanasenko, P. S. Yaremov, L. G. Sarkisyan, P. Chlubná, A. Zukal, V. R. Marthala, M. Hartmann, and J. Čejka, J. Mater. Chem. 22, 15793 **(2012)**.

[28] D. Goldfarb, M. Bernardo, K. G. Strohmaier, D. E. W. Vaughan, and H. Thomann, J. Am. Chem. Soc. 116, 6344 **(1994)**.

[29] J. Pérez-Ramírez, J. Groen, A. Bruckner, M. Kumar, U. Bentrup, M. Debbagh, and L. Villaescusa, J. Catal. 232, 318 **(2005)**.

[30] J. W. Park and H. Chon, J. Catal. 133, 159 **(1992)**.

[31] S. Bordiga, R. Buzzoni, F. Geobaldo, C. Lamberti, E. Giamello, A. Zecchina, G. Leofanti, G. Petrini, G. Tozzola, and G. Vlaic, J. Catal. 158, 486 **(1996)**.

[32] M. S. Kumar, M. Schwidder, W. Grünert, and A. Brückner, J. Catal. 227, 384 **(2004)**.

[33] L. Li, Q. Shen, J. Li, Z. Hao, Z. P. Xu, and G. Q. M. Lu, Appl. Catal. A Gen. 131, 344 **(2008)**.

[34] T. E. Westre, P. Kennepohl, J. G. DeWitt, B. Hedman, K. O. Hodgson, and E. I. Solomon, J. Am. Chem. Soc. 119, 6297 **(1997)**.

[35] M. Wilke, F. Farges, P. Petit, G. E. Brown, and F. Martin, Am. Mineral. 86, 714 **(2001)**.

[36] H. Takahashi and H. Oka, Tosoh research & technology review, 55, 53 **(2011)**.

[37] M. Ogura, T. Okubo, and S. P. Elangovan, Catal. Letters 118, 72 **(2007)**.

[38] Y. Kobatake, K. Momma, S. P. Elangovan, K. Itabashi, T. Okubo, and M. Ogura, ChemCatChem 8, 2516 **(2016)**.

[39] B. L. Yang and H. H. Kung, Environ. Sci. Technol. 28, 1561 **(1994)**.

Chapter 5

ZTS-1 and ZTS-2: Novel intergrowth zeolites with AFX/CHA structure

1. **Introduction**

Among more than 230 known zeolite structures exist some able to generate disordered structures. Ordered structures exhibit three-dimensional framework periodicity, whereas disordered ones lack periodicity in at least one crystallographic direction. Well-known examples of disordered structures are intergrowths of FAU/EMT [1], BEA/BEB (beta) [2], MFI/MEL (pentasils) [3], etc. [4-11]. The disordered structures of the ABC-6 family have also been well described, e.g., the intergrowths of CHA/GME (partially random stacking) [12, 13], OFF/ERI [14], and babelite (completely random stacking) [15]. The ABC-6 family structures can be described as stacked six-membered rings (6MRs) in the *ab* plane of the hexagonal crystal system. This structural similarity allows a variety of framework types in this group and enables me to envision disordered structures that have never been synthesized. The structural properties of zeolites, e.g., crystal shape, size, dimensions, and connectivity of micropores affect their catalytic, sorption, and ion-exchange behavior. Novel disordered structures may provide me with new application insights, since the different channel systems in these structures are reciprocally connected on the nanometer scale, forming

new microporous systems.

In this study, I tried to synthesize an intergrowth zeolite with AFX/CHA structures using the dual structure-directing agent (dual-SDA) approach. The AFX zeolite structure belongs to the ABC-6 family, exhibiting a three-dimensional eight-ring pore system just as the CHA zeolite. The 6MR stacking sequences of AFX and CHA structures are AABBCCBB and AABBCC, respectively. As a result, the AFX framework contains *aft* cages, which are larger than the *cha* cages in the corresponding framework (Figure 5-1), suggesting the high potential of the unique AFX pore structure for various reactions [16-19]. The first aluminosilicate AFX zeolite, SSZ-16, was first synthesized by S. I. Zones [20]. A typical organic SDA (OSDA) used in the synthesis of SSZ-16 is the 1,1'-(1,4-butanediyl)bis(1-azonia-4-azabicyclo[2,2,2]octane) dication (Dab-4^{2+}), which is a relatively large molecule that fits inside the *aft* cage [20]. CHA-type zeolites are originally known as natural chabazite [21], with a silica-rich CHA zeolite synthesized as SSZ-13 using the *N,N,N*-trimethyl-1-adamantylammonium cation ($TMAda^{+}$) [22]. The dual-SDA method is a promising approach for obtaining an intergrowth of intended end-member structures, since each SDA (not necessarily OSDA) is exclusively selected for each structure [23]. The intergrowth design gets harder if all end-member structures are obtained from the same SDA system, e.g., the tetraethylammonium cation for beta-zeolite [2]. As SAPO materials, the AFX/CHA intergrowth (SAPO-56/34) was reported in a patent literature [23]. The dual-SDA approach was employed to obtain the intended intergrowth materials. In this study, I report the synthesis of a novel AFX/CHA intergrowth aluminosilicate zeolite (ZTS-1:

zeolite of Tosoh 1) using Dab-4^{2+} and $TMAda^{+}$ as OSDAs for AFX and CHA phases, respectively. However, the limited synthesis conditions of ZTS-1 made control of the AFX/CHA ratio (80:20–85:15) difficult, unless the hydrothermal synthesis conditions were drastically changed. ZTS-2, a CHA-rich AFX/CHA intergrowth (15:85–20:80), could only be obtained under completely different synthetic conditions, using K^{+} instead of $TMAda^{+}$ as an SDA for CHA phase.

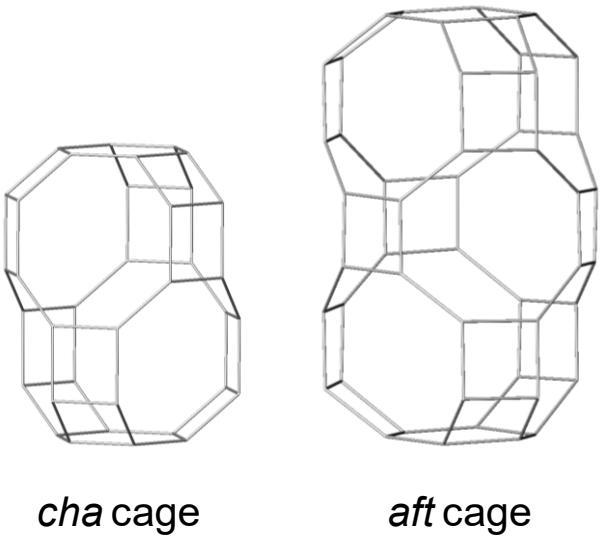

Figure 5-1 Structural models of *cha* and *aft* cages.

2. **Experimental**

2.1. Zeolite synthesis

The 1,1'-(1,4-butanediyl)bis(1-azonia-4-azabicyclo[2,2,2]octane) dication (Dab-4^{2+}) was synthesized according to a literature procedure [20]. 1,4-Diazabicyclo[2.2.2]octane (20.00 g) was dissolved in methanol (19.77 g) to produce solution A, while 1,4-dibromobutane (12.83 g) was added to methanol (6.6 g) and stirred for 15 min to prepare solution B. Solution B was dropwise added to solution A

under cooling. After stirring for 2 h, a white precipitate was obtained, which was washed and separated by decantation with diethyl ether, vacuum-dried at 50 °C, and dissolved in water to obtain 40 wt.% Dab-4Br_2.

The hydrothermal synthesis conditions were carefully investigated in preliminary experiments, as both AFX and CHA zeolites would crystallize from the same starting synthesis gel. As a result, the synthesis was carried out in a highly alkaline medium using a Y-type zeolite as an Al source to ensure crystallization of the AFX phase [20]. The starting synthesis gels were prepared by mixing sodium silicate (SiO_2 30 wt.%, Na_2O 9.1 wt.%, Al_2O_3 0.01 wt.%, Fuji Chemical), deionized water, 40 wt.% Dab-4Br_2, 25 wt.% *N*,*N*,*N*-trimethyl-1-adamantylammonium hydroxide (TMAdaOH, Sachem), 48 wt.% sodium hydroxide (Kaname Chemicals Co., Ltd.), and a commercial Y-type zeolite (HSZ-320NAA; SiO_2/Al_2O_3 = 5.5; Tosoh Corp.). The representative molar composition of the mixture used for ZTS-1 synthesis was as follows: 29.7 SiO_2 : Al_2O_3 : 11.5 Na_2O : 1.43 Dab-4Br_2 : 0.37 TMAdaOH : 843 H_2O. The obtained mixture was sealed in an 80-mL stainless steel autoclave and heated at 140 °C for 37 h under rotation. After the crystallization was complete, the obtained solid product was filtered, washed, and dried overnight at 110 °C. The pure AFX zeolite was also synthesized by replacing TMAdaOH with NaOH.

The CHA zeolite (SiO_2/Al_2O_3 = 23) was synthesized according to a literature procedure [24]. Deionized water, 48 wt.% sodium hydroxide, and 25 wt.% TMAdaOH were mixed, followed by the addition of aluminum hydroxide (Wako Pure Chemical Industries, Ltd.). Next, fumed silica (Aerosil 300, Nippon Aerosil Co., Ltd.) was added

and uniformly mixed. The molar composition of the resulting hydrogel was 28 SiO_2 : Al_2O_3 : 5.6 TMAdaOH : 5.6 NaOH : 1232 H_2O. The hydrogel was then heated at 150 °C under static conditions in a Teflon-sealed stainless steel autoclave (80 mL) for six days.

In the synthesis of ZTS-2, the potassium cation (K^+) was employed instead of $TMAda^+$, and a Y-type zeolite was used as a Si and Al source. The starting synthesis gel was prepared by mixing the Y-type zeolite, deionized water, 40 wt.% Dab-4Br_2, 48 wt.% NaOH, and 48 wt.% KOH. The molar composition of the mixture used to prepare ZTS-2 was as follows: 5.4 SiO_2 : Al_2O_3 : 1.59 Na_2O : 0.32 K_2O : 0.52 Dab-4Br_2 : 86 H_2O. The obtained mixture was sealed in an 80-mL stainless steel autoclave and heated at 100 °C for 72 h under rotation.

For a reference, a physical mixture of AFX and CHA zeolites was prepared by mixing weighed zeolite powders in a mortar for 10 min. SEM observation was performed to confirm that the zeolite powders were sufficiently mixed with each other.

2.2. Characterization

Powder X-ray diffraction (XRD) patterns of the products were recorded on an X'pert PRO MPD diffractometer (Spectris, Japan) using Cu K_α radiation and a scanning range (2θ) of 3–43°. The obtained XRD patterns were compared to the ones simulated by the DIFFaX software. Elemental analysis was carried out using inductively coupled plasma atomic emission spectroscopy (ICP-AES; OPTIMA 3300 DV, Perkin Elmer). The morphology of zeolite crystals was characterized using scanning electron

microscopy (SEM; JSM-6390LV, JEOL). Lattice images and electron diffraction patterns were obtained using a transmission electron microscope (TEM; JEM-ARM200F, JEOL). To confirm the presence of OSDA molecules in the zeolitic pores, solution ^{13}C NMR and solid-state ^{13}C DD/MAS NMR spectra were measured on a Varian VNMRS-400 NMR spectrometer at 100.5 MHz. In the solution NMR measurements, deuterium oxide (D_2O) was used as the lock-solvent, with trimethylsilylpropanoic acid (TSP) as an internal chemical shift reference. In the solid-state NMR measurements, hexamethylbenzene (HMB) was used as an external reference for the ^{13}C chemical shifts, and a recycle delay of 30 s was employed for quantitative comparison of peak intensities. Thermogravimetric and differential thermal analysis (TG/DTA) measurements were carried out using a thermal analyzer (TG-DTA 6300, Seiko Instruments, Inc.) to compare the decomposition behavior of OSDA molecules in zeolitic pores. The C/N ratio of organic molecules in micropores was calculated based on CHN analysis results provided by an organic elemental analyzer (2400 II, PerkinElmer). Nitrogen adsorption isotherms were measured at –196 °C using a volumetric apparatus (BELSORP-max, MicrotracBEL Corp.). Samples (~0.05 g) were evacuated at 350 °C for 2 h prior to the measurements.

2.3. Catalytic test

Cu-loaded ZTS-1, ZTS-2, and AFX zeolite catalysts for the NH_3-SCR reaction were prepared by the incipient wetness impregnation method [25]. The as-synthesized zeolite samples were calcined in air at 600 °C for 2 h to remove the OSDA cations

occupying the zeolite pores. Then, the Na cations in the calcined zeolite were exchanged for NH_4^+ in an aqueous solution of NH_4Cl (ca. 20 wt.%) at 40 °C for 0.5 h. This ion exchange was repeated three times, furnishing the NH_4^+-form of the zeolite. An aqueous $Cu(NO_3)_2$ solution was prepared, with its volume equal to the micropore volume of the support zeolite. This solution was added to the NH_4^+-zeolite, and the obtained wet powder was mixed to homogeneity and dried overnight at 110 °C. Finally, the obtained solid product was calcined in air at 550 °C for 2 h. The degree of Cu loading was 3 wt.% for all zeolites.

The NH_3-SCR reaction was performed using a fixed-bed flow reactor under atmospheric pressure between 150 and 500 °C. The catalyst was pelletized, crushed, and sieved to 0.85–1.4 mm, and 1.5 mL of the sieved sample were placed in a quartz tube. The gas composition used was 200 ppm NO, 200 ppm NH_3, 10 vol.% O_2, 3 vol.% H_2O, the rest being N_2. The total flow rate was set to 1.5 L/h, and the gas hourly space velocity (GHSV) was 60,000 h^{-1}. During the experiments, the temperature was reduced from 500 to 150 °C in steps of approximately 50 °C, and the NO_x conversion was calculated as follows:

NO_x conversion (%) = $[(NO_{in} - NO_{out} - NO_{2out})/ NO_{in}] \times 100\%$

where NO_{in} represents the NO inlet concentration (200 ppm) and NO_{out} and NO_{2out} represent the NO and NO_2 outlet concentrations, respectively. I also investigated the catalytic performance after hydrothermal treatment at 700 or 750 °C for 20 h in a flow of gas containing 10 vol.% H_2O and 90 vol.% air with a GHSV of 6,000 h^{-1} (300 mL/min flow, 3 mL catalyst). To evaluate the steady-state catalytic activity, the

concentrations of NH_3, NO, and NO_2 in the outlet gas after 10 min of time-on-stream at each reaction temperature were analyzed by an FT-IR spectrometer (FT/IR-6100, JASCO, Japan) equipped with a gas cell (LPC-12M-S, 12 m) and a mercury cadmium telluride detector cooled by liquid nitrogen. The NH_3, NO, and NO_2 concentrations were determined from their peak intensities at 1033, 1875, and 2917 cm^{-1}, respectively. Thirty scans were averaged for each normalized spectrum.

3. **Results and discussion**

3.1. Synthesis and characterization of ZTS-1

The hydrothermal synthesis conditions and characteristics of ZTS-1, AFX, and CHA zeolites are listed in Table 5-1, with the corresponding XRD patterns shown in Figure 5-2. All runs except AC-5, AFX-1, and CHA-1 produced an intergrowth phase (ZTS-1) supposedly consisting of AFX and CHA phases. Generally, the XRD pattern of intergrowth zeolites shows a mixture of sharp and broad peaks based on the direction of stacking faults in their structures [11, 13]. The peak positions of ZTS-1 were similar to those of AFX, with broadening of specific peaks observed. Assuming the AFX framework for ZTS-1, the sharp XRD peaks of this zeolite can all be indexed as parallel or perpendicular to the *c* direction (e.g., 2θ = 12.88° (110) and 17.86° (004)), suggesting the existence of stacking faults in this direction. The *d*-spacing of the AFX (004) plane corresponds to the spacing between double 6MRs (D6R) stacking layers. However, the CHA phase also exhibits the same *d*-spacing based on the same D6R stacking layers. Therefore, this is the reason for the sharpness of the XRD peak indexed as

perpendicular to the *c* direction, albeit ZTS-1 may exhibit stacking faults in this direction. The unit cell parameter *a* was calculated as 13.76 Å. This value varies depending on the ratio of single and double 6MRs in the framework of the ABC-6 family zeolites, e.g., being equal to 13.8 Å for GME and CHA (all-D6R), 13.1 Å for OFF (partially D6R), and 12.5 Å for CAN (all single 6MRs) [11]. Therefore, ZTS-1 was found to consist of all-D6R end-member structures. The overall XRD pattern of ZTS-1 was hardly changed by the hydrothermal synthesis conditions, leading to only a single CHA-phase byproduct or a pure AFX phase. Controlling the intergrowth ratio by simply adjusting the synthesis conditions seems to be difficult. The crystal morphologies of ZTS-1(AC-3) and ZTS-1 with a CHA byproduct (AC-1) are shown in Figure 5-3. ZTS-1 exhibits disk-like morphology, which is also observed for the disordered CHA phase [13]. Crystals with well-grown facets were considered as CHA crystals, and were all observed on the edge of ZTS-1, indicating that the single CHA phase crystallizes after completion of the intergrowth phase crystallization.

Table 5-1. Hydrothermal synthetic conditions and characteristics of ZTS-1, AFX, and CHA zeolites.

Sample	Chemical composition of starting synthesis gel						Temp. [°C]	Time [h]	Products	
	SiO_2/Al_2O_3	H_2O/Si	Dab-4^{2+}/Si	$TMAda^+$/Si	Na^+/Si	OH/Si			Phase	SiO_2/Al_2O_3
AC-1	29.7	28.4	0.096	0.045	0.755	0.800	140	96	ZTS-1[a] + CHA	9.0
AC-2	29.7	28.4	0.096	0.025	0.775	0.800	140	96	ZTS-1 + CHA	8.4
AC-3	29.7	28.4	0.096	0.015	0.785	0.800	140	96	ZTS-1	8.0
AC-4	29.7	28.4	0.020	0.025	0.775	0.800	140	96	CHA + ZTS-1	8.4
AC-5	29.7	28.4	0.096	0.025	0.800	0.850	140	96	AFX	-
AC-6	29.7	28.4	0.096	0.025	0.725	0.750	140	96	CHA + ZTS-1	-
AC-7	35.0	28.4	0.096	0.025	0.775	0.800	140	96	ZTS-1 + CHA	-
AC-8	25.0	28.4	0.096	0.025	0.775	0.800	140	96	ZTS-1	7.6
AFX-1	29.7	28.4	0.096	-	0.800	0.800	140	96	AFX	8.0
CHA-1	28.0	44.0	-	0.200	0.200	0.400	150	144	CHA	23

[a]AFX/CHA intergrowth phase.

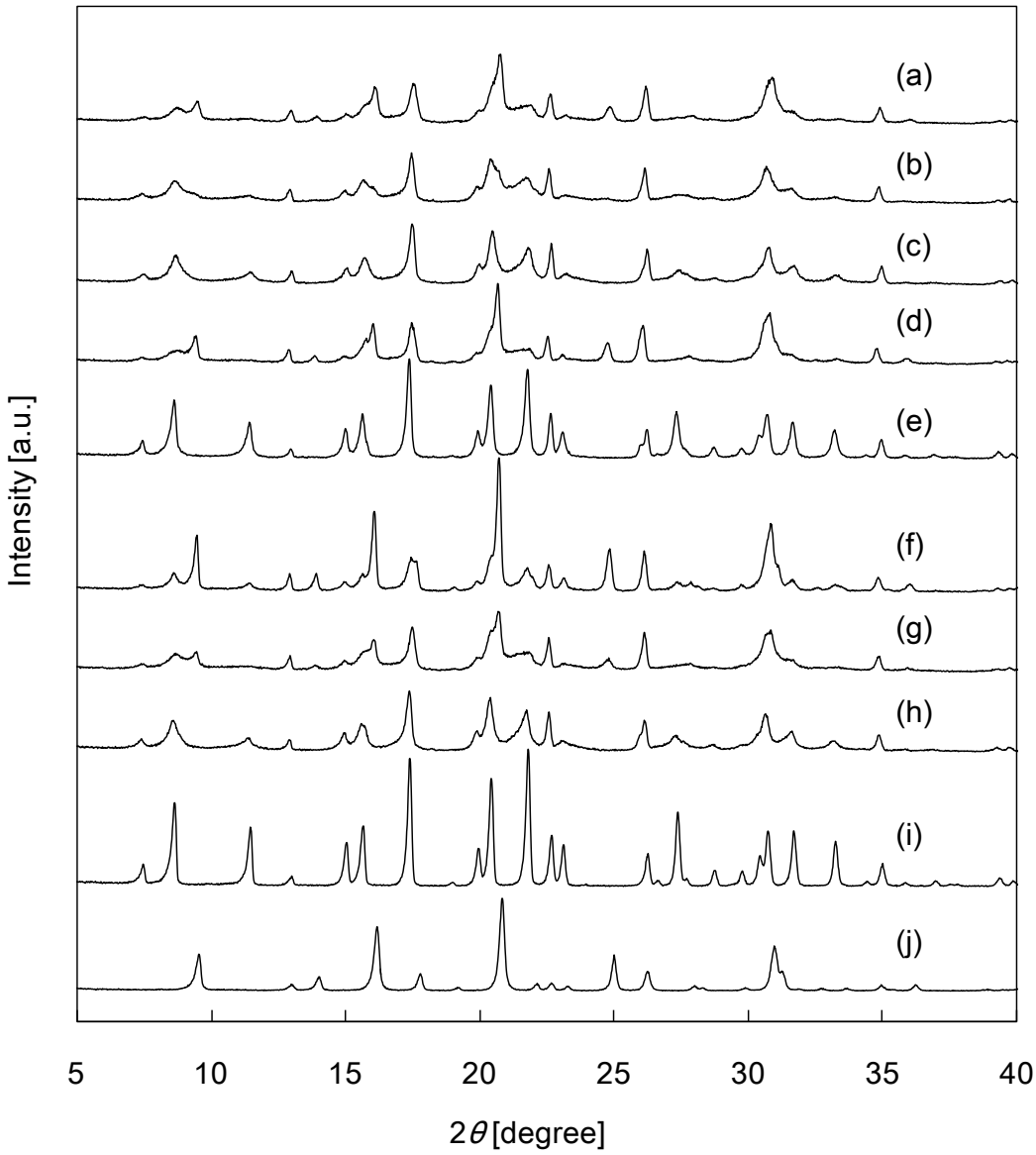

Figure 5-2 XRD patterns of as-synthesized samples. (a)–(h) AC-1 to AC-8, (i) AFX-1, and (j) CHA-1.

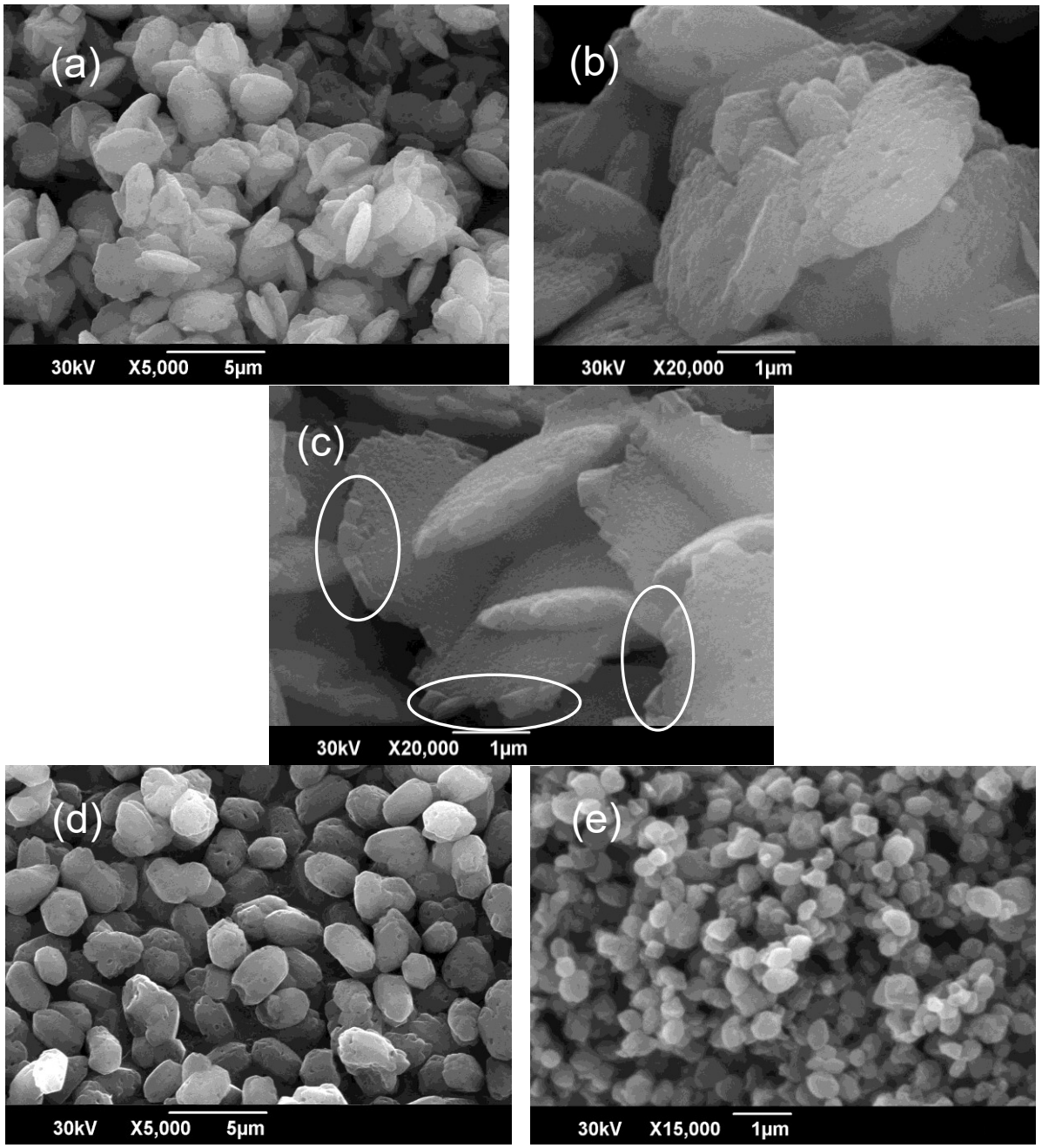

Figure 5-3 SEM images of as-synthesized ZTS-1, AFX, and CHA zeolites. (a), (b) AC-3, (c) AC-1, (d) AFX-1, and (e) CHA-1. Faceted CHA crystals were observed on the edge of the disk-like particles of ZTS-1 in (c), as indicated by white circles.

The crystallization behavior of AC-2 was investigated in detail to determine how both the intergrowth and single CHA phases are produced from the initial gel. Figures 5-4 and 5-5 show the changes in XRD patterns and SEM images of the obtained products, respectively. For a 13 h crystallization, the FAU phase of the Y-type zeolite used as an Al source was mainly observed. However, the presence of a small broad peak around $2\theta = 8.5°$ and the corresponding SEM image indicated that the intergrowth phase had already appeared. The crystallization of this phase was completed at 37 h, after the disappearance of the FAU phase, with no single CHA phase observed at this point. This result was consistent with the SEM characterization of AC-1 in Figure 5-3, which shows that CHA crystals grew at the end of the crystallization period. The N_2 adsorption isotherm of AC-2 obtained at 37 h showed a type I, indicating microporosity of the material (Figure 5-6). The micropore volume of AC-2 obtained at 37 h calculated from the N_2 adsorption isotherm was 0.26 cm^3/g, being comparable to that of AFX-1 (0.27 cm^3/g). The change in the chemical composition (SiO_2/Al_2O_3 and Na/Al ratios) during crystallization is shown in Figure 5-7. The SiO_2/Al_2O_3 ratio of ZTS-1 obtained at 37 h was ~8, slightly increasing after a prolonged crystallization time, probably due to the formation of a CHA byproduct. The fact that the Na/Al ratio of 0.63 at 13 h was lower than unity suggests that the Y-type zeolite included OSDA molecules in its micropores (about 2.4 OSDA cation charges per supercage). Taking into account that the Na/Al ratio (OSDA cation/Al) was almost constant until 96 h, ZTS-1 was considered to crystallize utilizing OSDAs in the micropores of the Y-type zeolite. If this speculation is correct, I may be able to control the ratio of the intergrowth phase by controlling the

ratio of OSDAs inside the Y-type zeolite. The electron diffraction pattern of ZTS-1 (AC-2 (37 h)) on the [100] zone axis is shown in Figure 5-8. Streaks along the c^*-axis were observed, suggesting stacking faults along the *c*-axis, as expected from the corresponding XRD pattern. In addition, Figure 5-9 shows the lattice image by the low-dose TEM. The image verified the existence of AFX/CHA intergrowth structure.

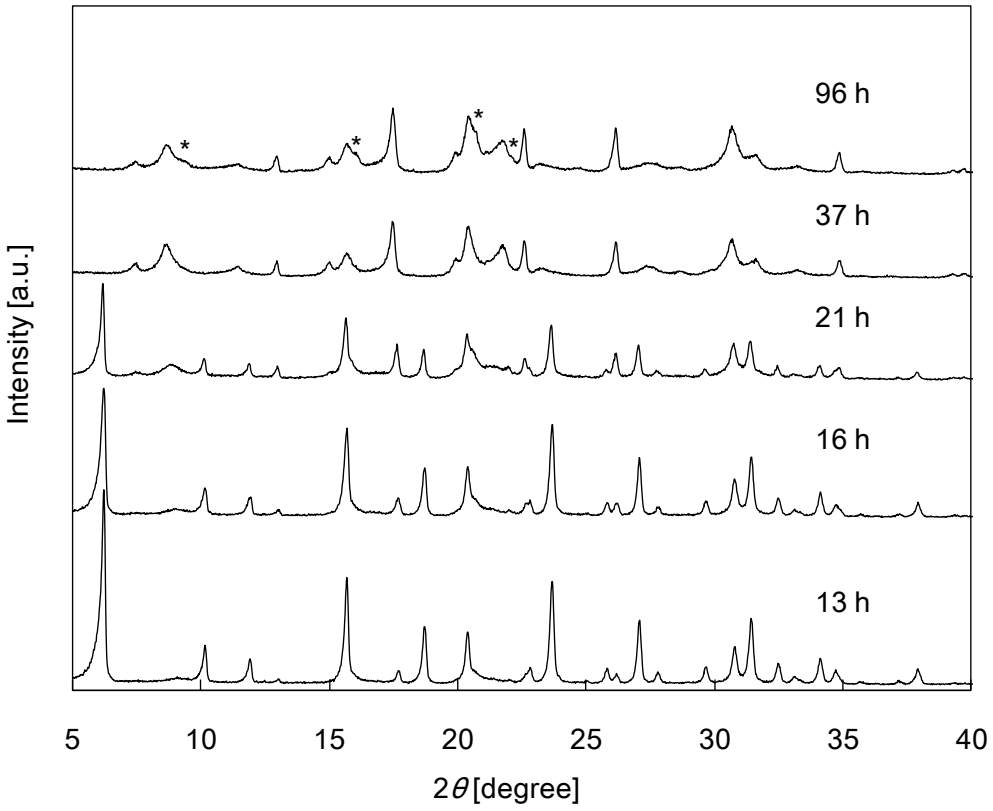

Figure 5-4 XRD pattern changes during the crystallization of ZTS-1. Asterisks indicate the pure CHA phase.

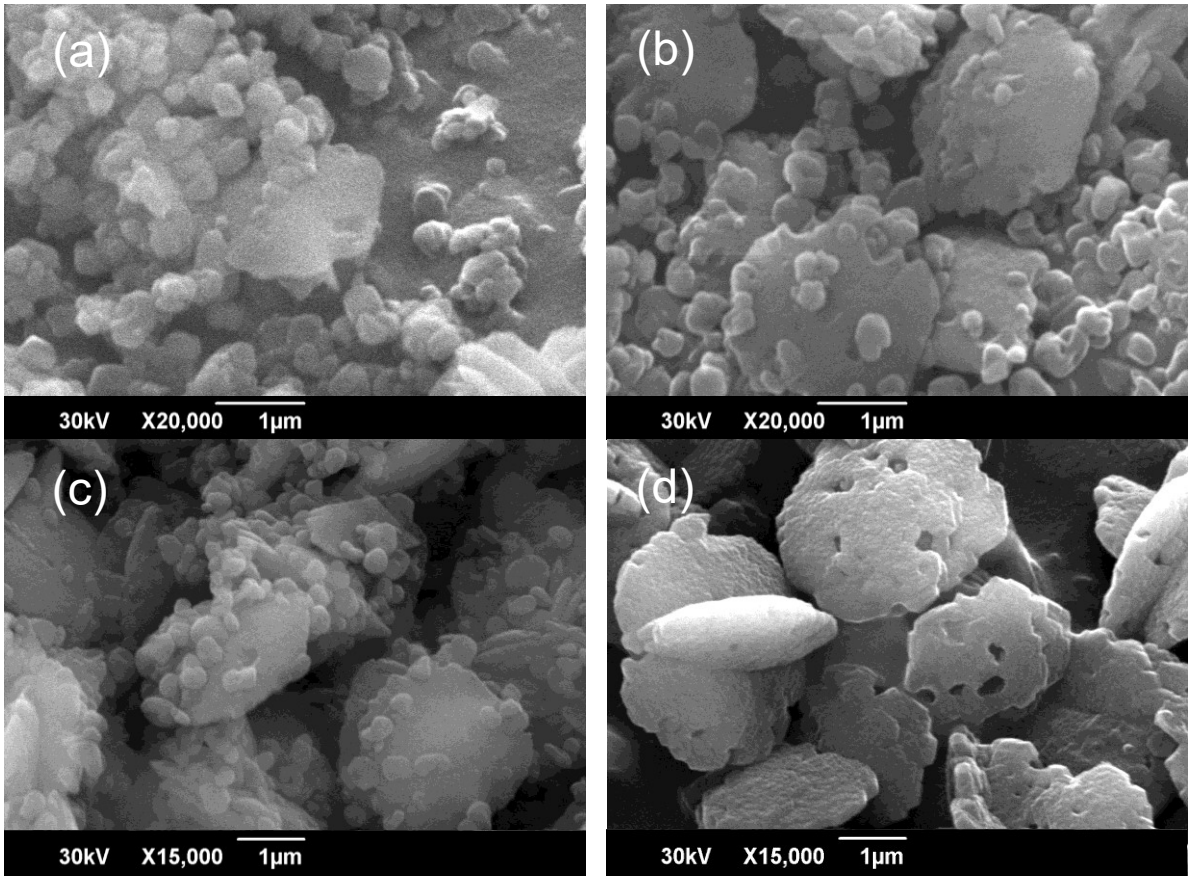

Figure 5-5 Crystal morphology changes during crystallization of ZTS-1. Crystallization time: (a) 13 h, (b) 16 h, (c) 21 h, and (d) 37 h.

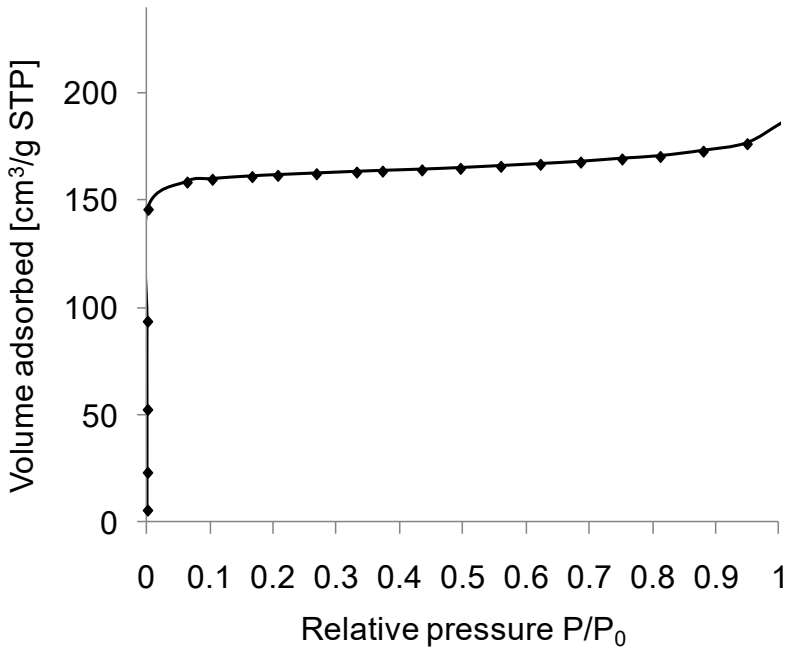

Figure 5-6 N_2 adsorption isotherm of ZTS-1.

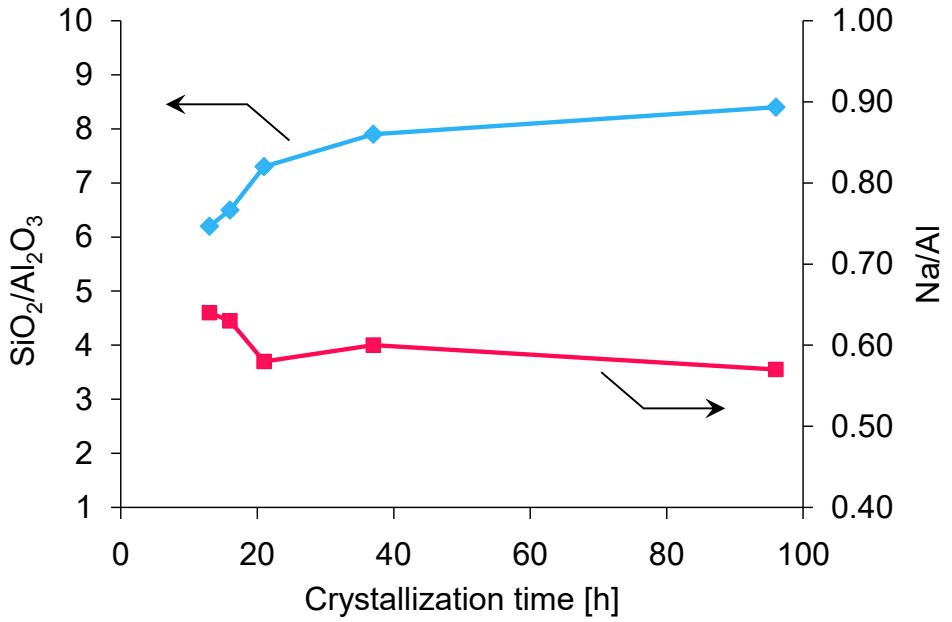

Figure 5-7 Changes in SiO_2/Al_2O_3 and Na/Al ratios during crystallization of ZTS-1.

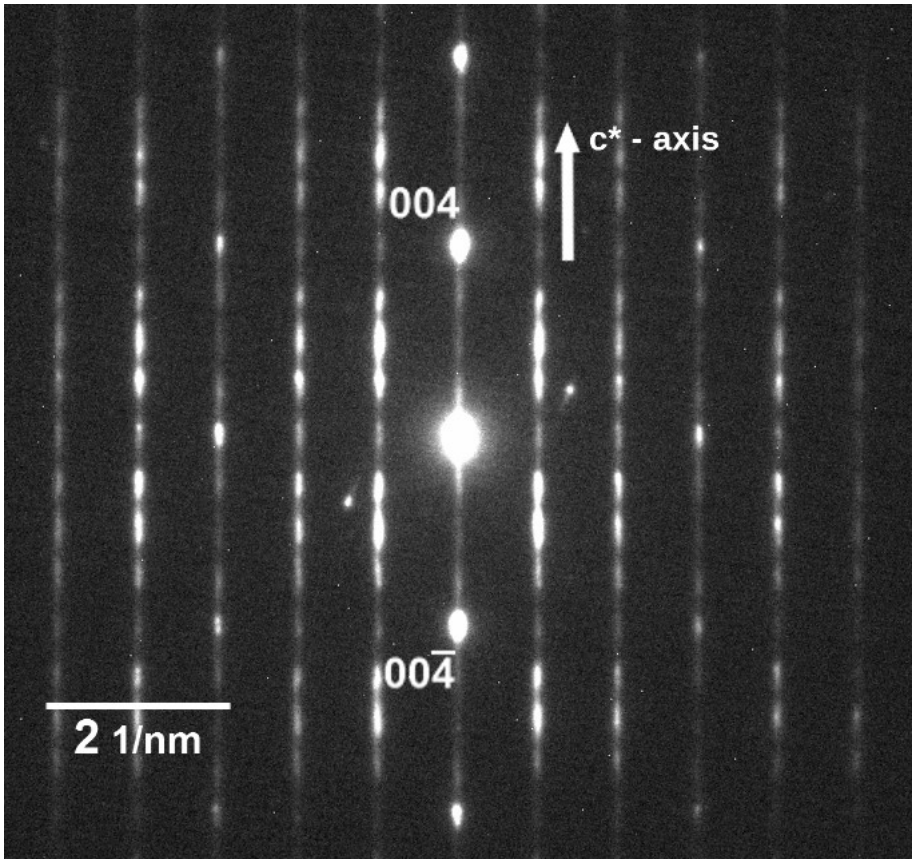

Figure 5-8 Electron diffraction pattern of ZTS-1 for the [100] zone axis.

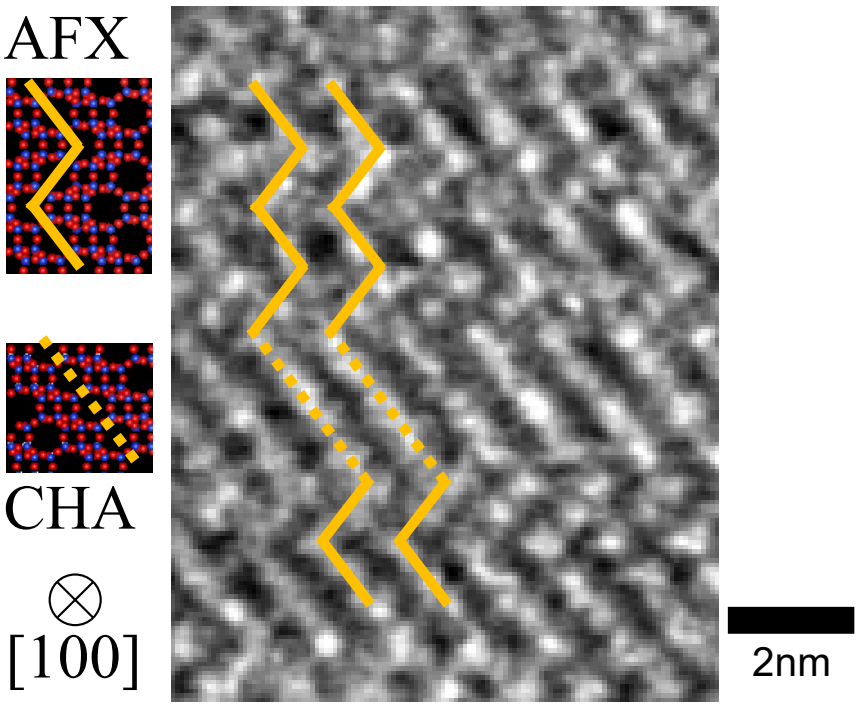

Figure 5-9 Lattice image of ZTS-1.

3.2. Determination of the AFX/CHA ratio

DIFFaX is a program developed by M. M. J. Treacy [26] to calculate the diffraction patterns of zeolites having stacking faults. I used this program to verify that ZTS-1 was composed of AFX and CHA end-member structures, and determine their ratio. Figure 5-10 shows the simulated XRD patterns of an AFX/CHA intergrowth zeolite with different AFX/CHA ratios (shown as AFX:CHA based on the number of unit cells). A pure silica composition was assumed for the simulation. Several peaks are useful to determine the AFX/CHA ratio, e.g., the position of the peak around 2θ = 8.5–9.5° shifts depending on this ratio. The peak at 2θ = 11.7° can only be observed for the AFX-rich phase, broadening with increasing CHA phase content. The XRD pattern of calcined ZTS-1 (AC-2 obtained at a crystallization time of 37 h) was different from

that of a physical mixture of AFX-1 and CHA-1 (80:20 based on the number of unit cells), and well fitted by the simulated pattern with an AFX/CHA ratio of 80:20, as shown in Figure 5-11. As described above, the AFX/CHA ratio of ZTS-1 could not be changed by varying the hydrothermal synthesis conditions in the present study (Table 5-1 and Figure 5-2). As for the simulation of XRD patterns of intergrowth zeolites, a new approach to obtain more precise description of the structures has been proposed; Slawinski et al. reported that the XRD patterns for SAPO-18/34 intergrowth vary depending on the different stacking fault type (*Displacement* and *Growth*) [27]. The simulated XRD patterns of AFX/CHA intergrowth in my study could be based on the *Displacement* stacking fault, because the direction of crystal growth was fixed on the DIFFaX simulation. Such an approach would be useful for the further refinement of the structure of ZTS-1.

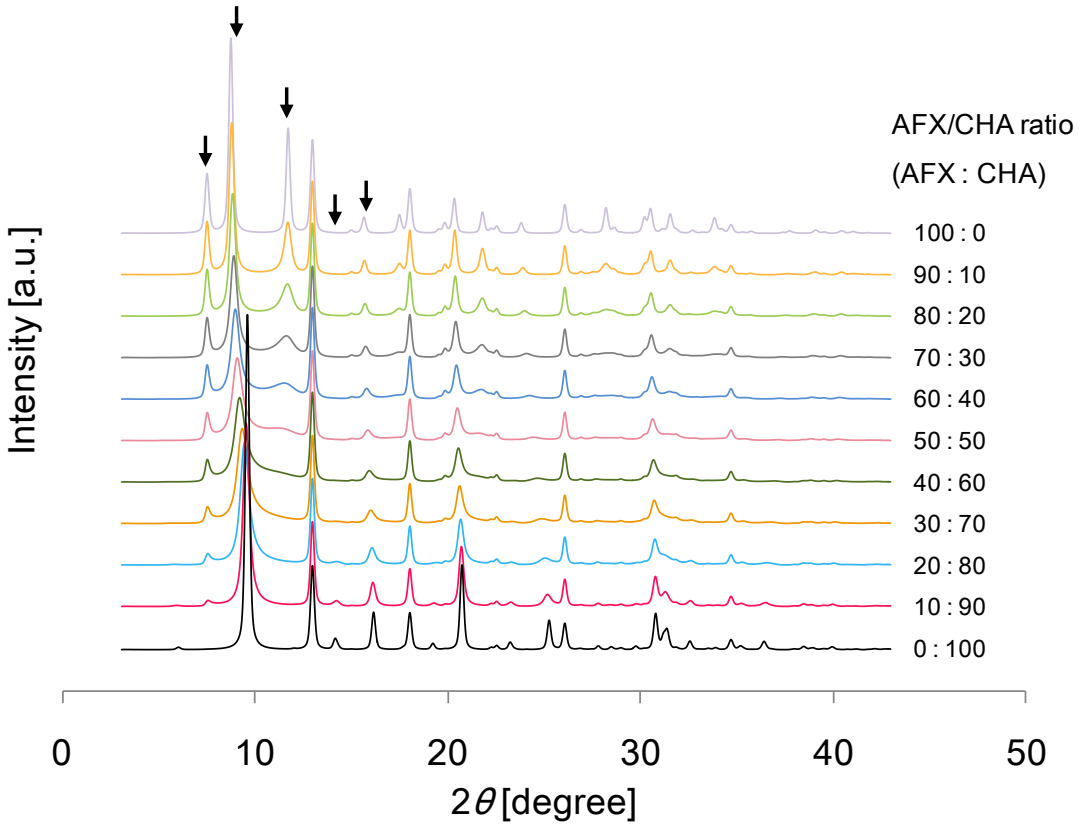

Figure 5-10 XRD patterns of AFX/CHA intergrowth zeolites simulated by DIFFaX software.

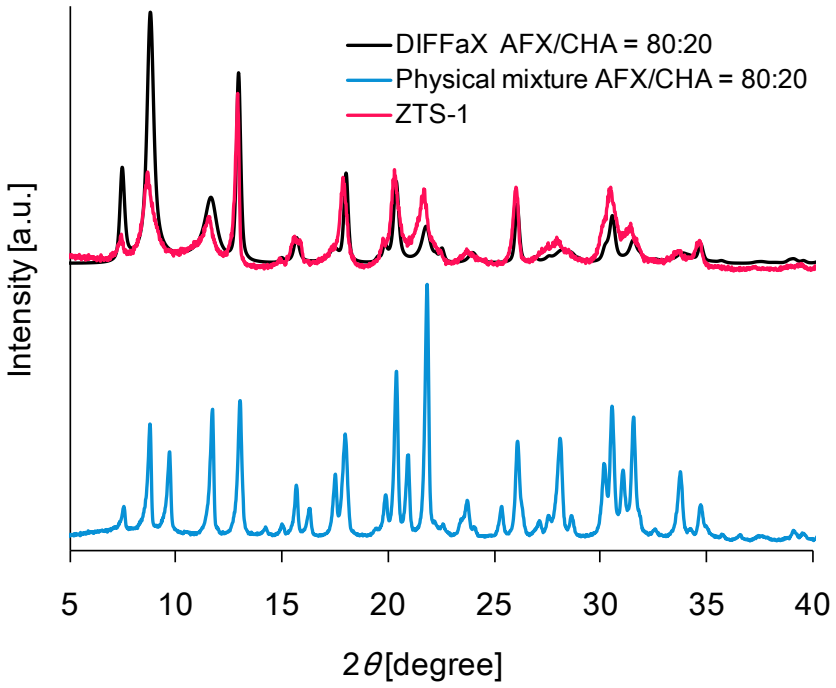

Figure 5-11 Comparison of the experimental XRD pattern of calcined ZTS-1 (AC-2 obtained at a crystallization time of 37 h) with the simulated XRD pattern of an AFX/CHA intergrowth zeolite and the physical mixture of AFX and CHA (AFX/CHA ratio = 80:20).

^{13}C NMR spectra were recorded to confirm that ZTS-1 incorporates two kinds of OSDAs without decomposition, namely Dab-4^{2+} and TMAda^{+}. Figure 5-12 shows the solution ^{13}C NMR spectra of the OSDA cations and the solid-state ^{13}C DD/MAS NMR spectrum of ZTS-1 (AC-2 obtained at a crystallization time of 37 h). Peak assignments in the solution NMR spectra (a) and (b) were based on the spectra simulated using the ACD/C NMR prediction software. The ZTS-1 peaks in the solid-phase spectrum (c) were assigned to the carbon atoms of both OSDAs based on the order/value of the chemical shifts in their solution NMR spectra as well as the comparison of the relative peak intensities and number of carbon atoms in their molecules. Apparently, ZTS-1 contained both Dab-4^{2+} and TMAda^{+} in its micropores. The shoulders observed for peaks 2A and 3A suggest that the molecular mobility and/or conformation is less restricted for a part of Dab-4^{2+} molecules, since the positions of the shoulder peaks were close to those in the solution-phase NMR spectrum. Using the peak area ratio of 2A (including the shoulder peak) for Dab-4^{2+} and 2B for TMAda^{+}, the molar ratio of Dab-4^{2+} to TMAda^{+} was calculated as 72:28. In this analysis, I hypothesized that Dab-4^{2+} and TMAda^{+} exclusively function as OSDAs for AFX and CHA phases, respectively, and all cages (*aft* cage in AFX and *cha* cage in CHA) are filled with these OSDAs as one molecule per cage, except for the *gme* cage in AFX due to its small void space. Based on the obtained OSDA molar ratio and the number of cages per unit cell (two cages for AFX and three for CHA), I calculated the AFX/CHA ratio of ZTS-1 as 80:20 (number of unit cells, Table 5-2). This estimation was consistent with the above DIFFaX simulation result.

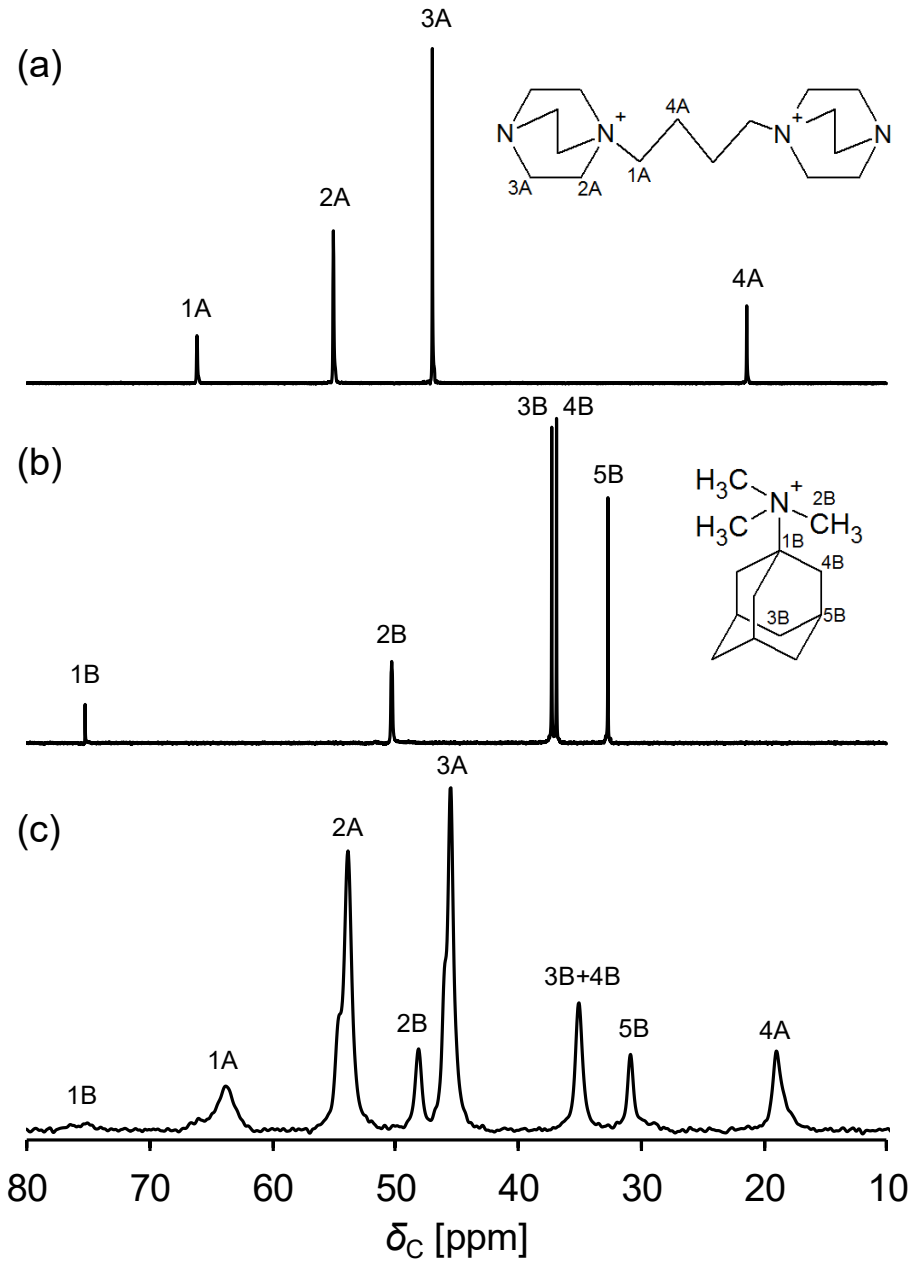

Figure 5-12 Solution ^{13}C NMR spectra of (a) Dab-4^{2+} and (b) $TMAda^{+}$, and (c) solid-state ^{13}C DD/MAS NMR spectrum of ZTS-1 (AC-2 obtained at a crystallization time of 37 h).

Table 5-2. Calculated AFX/CHA ratio based on the ^{13}C DD/MAS NMR spectrum of ZTS-1.

Sample	Phase	Peak of ^{13}C DD/MAS NMR spectrum in Fig. 12	Relative peak area [%]	Number of carbon atoms	Molar ratio of OSDAs [mol.%]	Number of unit cells [%]
AC-2 (37 h)	ZTS-1	2A	29.2	6	72 (Dab-4^{2+})	80 (AFX)
		2B	5.6	3	28 (TMAda^{+})	20 (CHA)

To obtain further information on OSDA cations occluded in zeolite crystals, TG/DTA measurements were carried out. Figure 5-13 shows the TG/DTA curve of the as-synthesized ZTS-1. For comparison, TG/DTA curves of CHA-1, AFX-1, and the physical mixture of these zeolites (50:50, w/w) are also shown. The physical mixture sample showed two peaks corresponding to each of the mixed zeolites, but the position of the CHA zeolite peak shifted toward lower temperature. Unexpectedly, only a single DTA peak was observed for ZTS-1, although it contained two kinds of OSDA cations, as confirmed by ^{13}C DD/MAS NMR. Moreover, this DTA peak was found at the lowest temperature compared to the other samples. Therefore, it seems obvious that the environment of OSDAs in ZTS-1 is somewhat different from that of OSDAs present in the physical mixture, resulting in a characteristic DTA peak. The sequential layers of certain phases in intergrowth zeolites are expected to be several nanometers thick, since the phase change should occur frequently enough (every several layers) to obtain the zeolite exhibiting the XRD pattern simulated by DIFFaX. From the viewpoint of OSDAs in the zeolite micropores, it is reasonable to consider that zeolite layers containing one OSDA are placed between ones containing another OSDA, which is reciprocally continued. Such close packing of different OSDAs might lead to their decomposition as if they were a single molecular entity, resulting in a single DTA peak. The low-temperature decomposition shift may also be explained by considering the above model, that is, the small domain or crystallite size of each zeolite phase, resulting in a weak stabilization of OSDA molecules in the zeolitic pores.

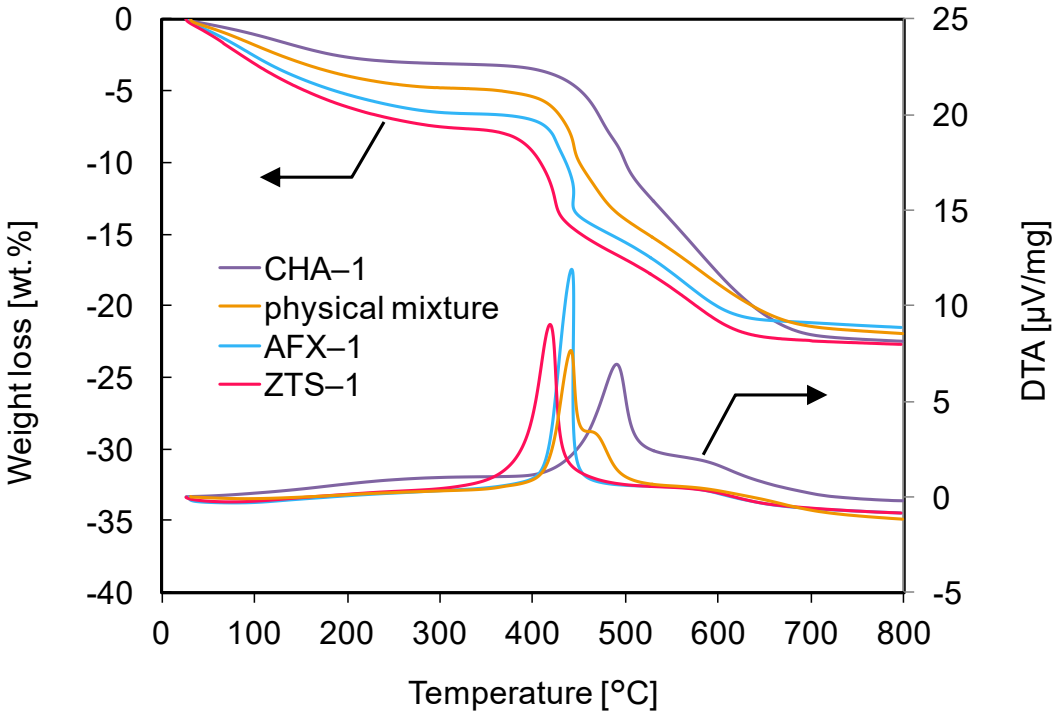

Figure 5-13 TG/DTA curves of various as-synthesized zeolites. ZTS-1 (red), AFX-1 (blue), CHA-1 (purple), and a physical mixture of 50 wt.% AFX-1 and 50 wt.% CHA-1 (orange).

Another estimation of the AFX/CHA ratio of ZTS-1 was carried out by CHN analysis, based on the C/N ratio of the organic compounds inside the micropores, with the results summarized in Table 5-3. The C/N ratio of AC-2 obtained at a crystallization time of 37 h was 4.6, slightly higher than that of Dab-4^{2+} (theoretical C/N = 4.0), indicating a composition of 79 mol.% Dab-4^{2+} and 21 mol.% TMAda^{+}. However, the C/N ratio of AFX-1, which contains only Dab-4^{2+}, was 3.8, indicating that the experimental C/N value may be lower than the theoretical one (4.0) within an experimental error. Based on the obtained molar ratio, the AFX/CHA ratio of ZTS-1 was estimated as 85:15. If I correct the C/N ratio of ZTS-1 using the theoretical C/N ratio of Dab-4^{2+} and the experimental C/N ratio of AFX-1 (4.0/3.8), the C/N ratio of

ZTS-1 is obtained as 4.8, and the calculated molar ratio of Dab-4^{2+} and $TMAda^{+}$ would be 72:28. Interestingly, the corrected molar ratio is the same as that determined by ^{13}C DD/MAS NMR. The C/N ratio increased to 5.2 when the CHA byproduct appeared for AC-2 obtained at a crystallization time of 96 h (AC-2 (96 h)), corresponding to the incorporation of $TMAda^{+}$ (theoretical C/N = 13). Taking all these results into account, I can conclude that ZTS-1 is an intergrowth zeolite exhibiting AFX/CHA phases in a ratio estimated as 80:20–85:15 with high probability.

Table 5-3. CHN analysis results and calculated AFX/CHA ratios.

Sample	Phase	C/N [mol/mol]	Molar ratio of OSDAs [mol.%]		Number of unit cells [%]	
			Dab-4^{2+}	$TMAda^{+}$	AFX	CHA
AC-2(37 h)	ZTS-1	4.6	79	21	85	15
AC-2(96 h)	ZTS-1 + CHA	5.2	63	37	71	29

3.3. NH_3-SCR of NO_x activity test

The catalytic performance of Cu-loaded ZTS-1 in the NH_3-SCR reaction was evaluated and compared to that of the Cu-loaded AFX (AFX-1) catalyst, which exhibits a SiO_2/Al_2O_3 ratio (8.0) close to that of ZTS-1 (7.9). Fickel et al. reported the high catalytic activity of SSZ-16 (AFX) in this reaction [16]. Figure 5-14 shows the NO_x conversion over the Cu-loaded ZTS-1 and the Cu-loaded AFX catalysts before hydrothermal treatment (fresh). The NO_x conversion of the Cu-loaded ZTS-1 catalyst was almost equal to that of the corresponding AFX catalyst in the whole reaction

temperature range. No specific effect of the intergrowth phase was observed. However, after hydrothermal treatment at 700 or 750 °C for 20 h, the Cu-loaded ZTS-1 catalyst showed higher stability for low-temperature (150 °C) activity (Figure 5-15). In contrast, it was suggested from N_2 adsorption isotherms and the calculated micropore volumes (0.19 cm^3/g for Cu-loaded ZTS-1 and 0.28 cm^3/g for Cu-loaded AFX-1) by the t-plot method after hydrothermal treatment at 750 °C for 20 h that the crystals of ZTS-1 had more damage than SSZ-16(AFX) by the hydrothermal treatment (Figure 5-16). As shown in the TEM image (Figure 5-9), the crystallites, or domains, of intergrowth zeolites are intrinsically small, resulting in the less stability of a part of the crystals. Any major changes in the composition were not observed for both samples before and after hydrothermal treatment. Therefore, the improvement of hydrothermal stability of Cu-loaded ZTS-1 may be due to the CHA domain inserted between AFX phases. The typical SiO_2/Al_2O_3 ratio of the AFX zeolite (AFX-1) synthesized using Dab-4^{2+} is less than 10, since Dab-4^{2+} is a divalent cation, with additional cations (e.g., alkali metal cations) needed to stabilize the *gme* cage that cannot be occupied by Dab-4^{2+}. On the other hand, the $TMAda^+$ cation used in the case of the CHA zeolite is a bulky monovalent cation, making higher SiO_2/Al_2O_3 ratios more preferable compared to the case of Dab-4^{2+}. If the CHA domain in ZTS-1 has a higher SiO_2/Al_2O_3 ratio than the AFX one, the CHA domain in ZTS-1 is expected to show improved hydrothermal stability. Since the bulk SiO_2/Al_2O_3 ratios of ZTS-1 and AFX are almost the same, the difference in the SiO_2/Al_2O_3 ratios between AFX and CHA domains is expected to be small even if it exists.

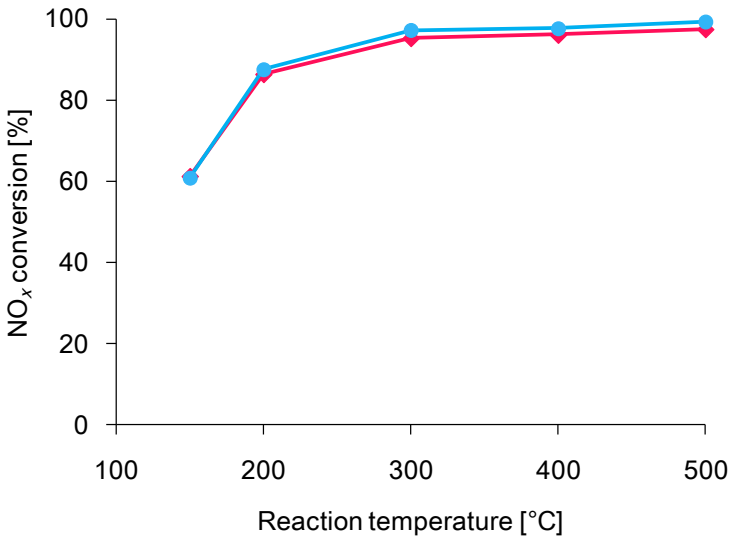

Figure 5-14 Conversion of NO_x over (◆) Cu-loaded ZTS-1 (AC-2 (37 h)) and (○) Cu-loaded AFX (AFX-1) catalysts before hydrothermal treatment.

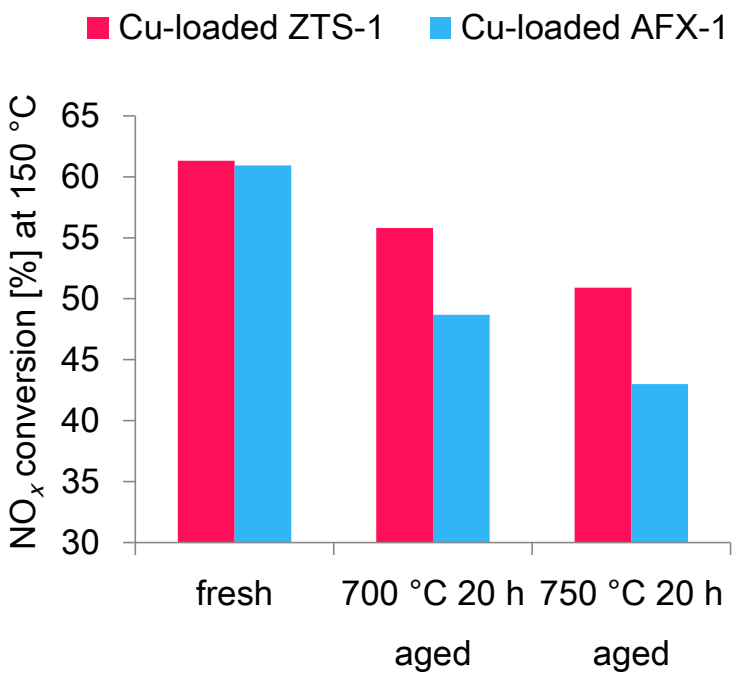

Figure 5-15 Conversion of NO_x at 150 °C over Cu-loaded ZTS-1 (red) and Cu-loaded AFX (AFX-1) (blue) catalysts after hydrothermal treatment at 700 or 750 °C for 20 h.

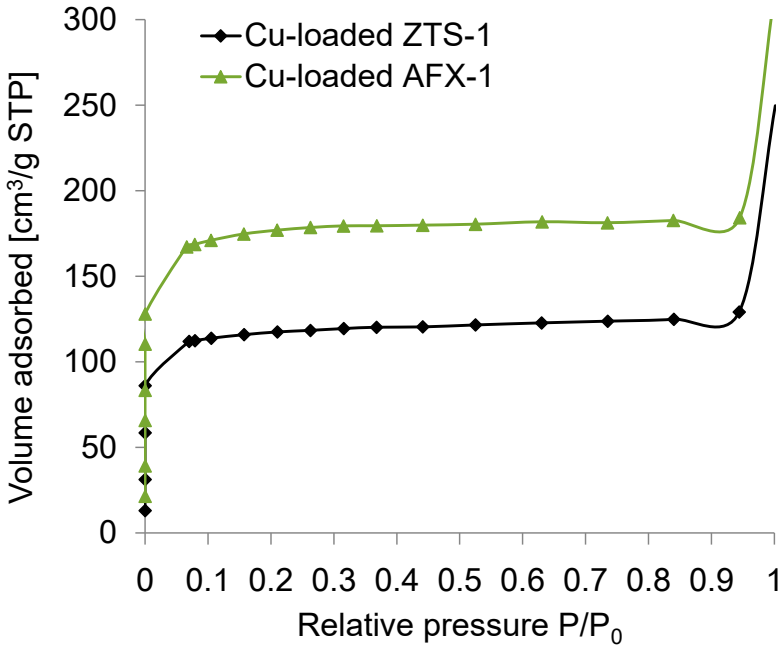

Figure 5-16 N_2 adsorption isotherms of Cu-loaded ZTS-1 and Cu-loaded AFX-1 after hydrothermal treatment at 750 °C for 20 h.

Table 5-4. Synthetic condition for ZTS-2.

Sample	Chemical composition of starting synthesis gel						Temp.	Time	Product	
	SiO_2/Al_2O_3	H_2O/Si	Dab-4^{2+}/Si	Na^+/Si	K^+/Si	OH/Si	[°C]	[h]	Phase	SiO_2/Al_2O_3
ZTS-2	5.4	16	0.096	0.59	0.12	0.71	100	72	ZTS-2[a]	4.2

[a]AFX/CHA intergrowth phase (CHA rich).

3.4. Synthesis of ZTS-2

As described above, controlling the AFX/CHA ratio by changing the hydrothermal synthesis conditions was difficult (Table 5-1). Therefore, I tried to synthesize the AFX/CHA intergrowth zeolite under conditions completely different from those of ZTS-1 to obtain zeolites with a different AFX/CHA ratio. Table 5-4 shows

the synthesis conditions of ZTS-2, with potassium cations (K^+) used instead of $TMAda^+$. The former is known to exhibit a structure-directing effect for CHA, especially for low-silica synthetic chabazite [28]. After 72 h of crystallization at 100 °C, an AFX/CHA intergrowth phase was obtained. The XRD pattern of calcined ZTS-2 was compared to that simulated by DIFFaX (AFX/CHA ratio of 20:80, Figure 5-17). It was also compared to that of the physical mixture of AFX and CHA zeolites (20:80 based on the number of unit cells), and I confirmed that ZTS-2 was not just a physical mixture of AFX and CHA phase. Compared to the simulated pattern, an apparent peak shift to lower angles was observed for ZTS-2 due to the lattice expansion caused by a higher Al content (SiO_2/Al_2O_3 = 4.2). The relatively large shift for 2θ = 17.6° may indicate the difference in the local structure of ZTS-2, since the simulation was based on a pure silica composition. Some intergrowth clues can be found in this pattern. The tiny peak at 2θ = 7.7° can only be observed for the intergrowth phase as opposed to the pure CHA phase. In contrast, the peak at 2θ = 14.1° clearly exists in the CHA phase, immediately disappearing with increasing AFX/CHA ratio (Figure 5-10). ZTS-2 showed no peak at this position, unlike the simulated pattern. The relative peak intensities are different in the experimental and simulated data, with peak broadening probably responsible for such weak intensity. The peak at 2θ = 16.0° is broadened, in accordance with the simulated pattern. Based on XRD pattern matching, the AFX/CHA ratio of ZTS-2 was estimated as 20:80. Figure 5-18 shows the SEM image of ZTS-2. The crystals of ZTS-2 had irregular shape and were agglomerated compared to ZTS-1 (Figure 5-5). The AFX/CHA ratio was also estimated from the amount of OSDA measured by TG/DTA

analysis. The decrease of weight from 300 to 800 °C was 2.9 wt.%, implying about 19 wt.% of the AFX phase in ZTS-2, assuming a 15.6 wt.% decrease for a purely AFX composition. The AFX/CHA ratio of ZTS-2 was calculated as 15:85 based on the number of unit cells. This estimation was quantitative and was considered to be more accurate than obtained by XRD pattern matching.

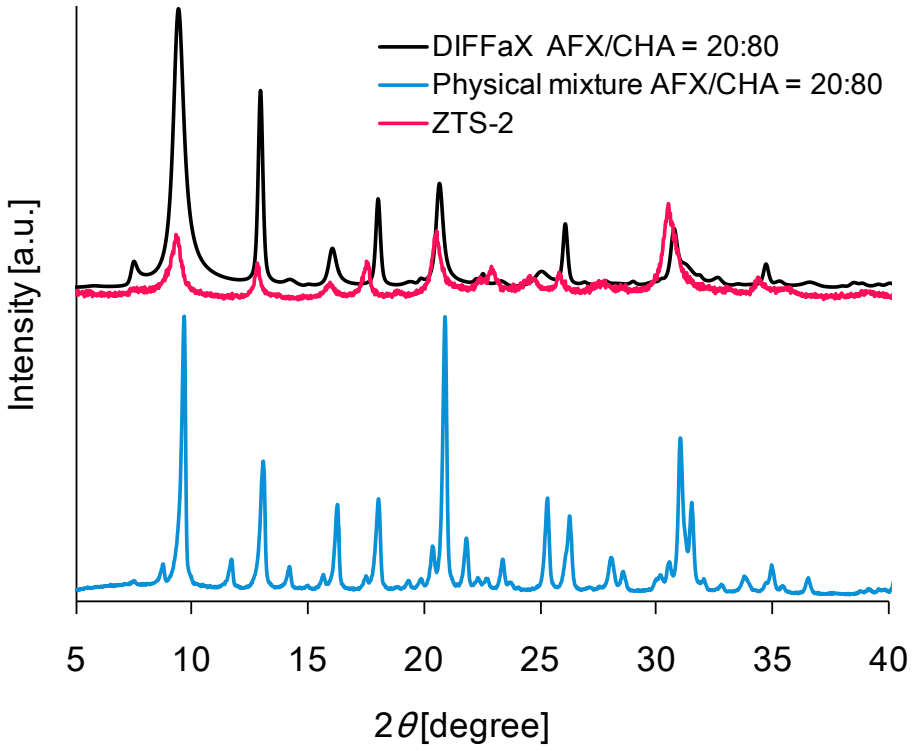

Figure 5-17 Comparison of the experimental XRD patterns of calcined ZTS-2 with the simulated XRD pattern of an AFX/CHA intergrowth zeolite and the physical mixture of AFX and CHA (AFX/CHA ratio = 20:80).

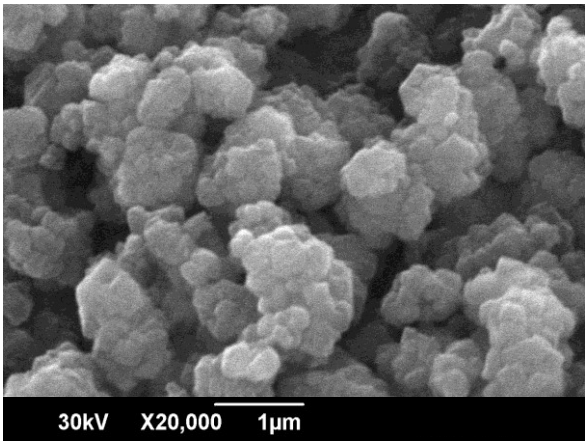

Figure 5-18 SEM image of as-synthesized ZTS-2.

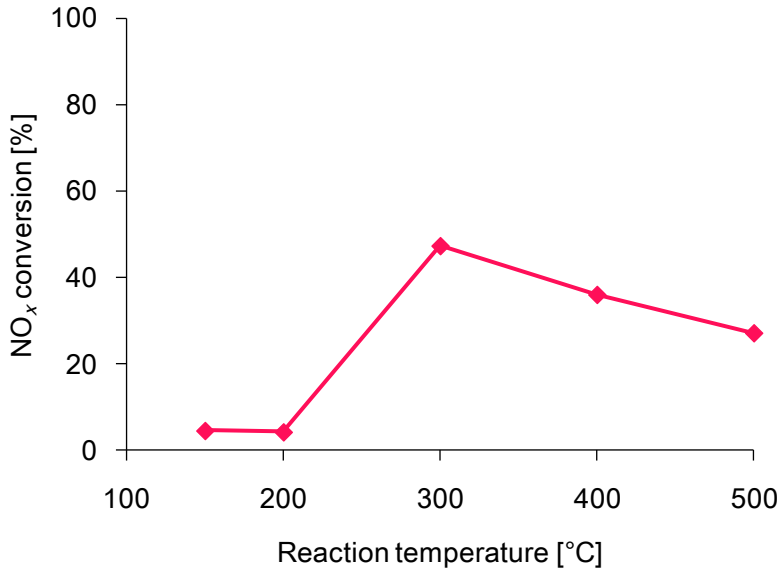

Figure 5-19 Conversion of NO_x over Cu-loaded ZTS-2 catalyst before hydrothermal treatment.

Finally, the catalytic performance of Cu-loaded ZTS-2 in the NH_3-SCR reaction was measured (Figure 5-19). It showed poor performance compared to the Cu-loaded ZTS-1 in fresh state. Moreover, XRD measurement showed that the crystals of ZTS-2 mostly collapsed after hydrothermal treatment at 700 °C for 20 h (data not shown). In the case of ZTS-1, the improvement of hydrothermal stability was observed by inserting CHA phase (Figure 5-15). However, N_2 adsorption data suggested that the

crystal of ZTS-1 had more damage than SSZ-16 (AFX) by hydrothermal treatment (Figure 5-16). Therefore, the lower hydrothermal stability of ZTS-2 is probably due to its low SiO_2/Al_2O_3 ratio and poor crystallinity. Further discussion about an effect of AFX/CHA ratio on the catalytic activity and hydrothermal stability will be possible if ZTS-1 and ZTS-2 with close SiO_2/Al_2O_3 ratio are synthesized.

4. **Conclusions**

Novel AFX/CHA intergrowth aluminosilicate zeolites ZTS-1 and ZTS-2 were synthesized by the dual-SDA approach. ZTS-1, an AFX-rich intergrowth, was obtained using Dab-4^{2+} and $TMAda^+$ as OSDAs for the AFX and CHA phases, respectively. The existence of AFX/CHA intergrowth structure was directly confirmed by low-dose TEM. The AFX/CHA ratio of ZTS-1 was determined as 80:20–85:15 by XRD pattern matching with DIFFaX simulation, ^{13}C DD/MAS NMR, and CHN analysis. TG/DTA measurements also indicated that the environment of OSDAs in ZTS-1 is different from that in the physical mixture of zeolites. The AFX/CHA ratio of ZTS-1 was hardly changed by variation of its synthetic parameters. Although the Cu-loaded ZTS-1 had more damage in its crystal structure by hydrothermal treatment compared to the Cu-loaded AFX catalyst, the Cu-loaded ZTS-1 showed high catalytic activity in the NH_3-SCR reaction and exhibited better hydrothermal stability than the Cu-loaded AFX catalyst, suggesting a contribution of the silica-rich CHA domain in ZTS-1.

ZTS-2, a CHA-rich intergrowth, was synthesized using K^+ instead of $TMAda^+$ for the CHA phase, under synthetic conditions completely different from those of ZTS-1.

The AFX/CHA ratio of ZTS-2 was estimated as 15:85–20:80 using XRD pattern matching and the amount of Dab-4^{2+} obtained by TG/DTA analysis.

Acknowledgement

TEM observation in this work was supported by NIMS microstructural characterization platform as a program of "Nanotechnology Platform" of the Ministry of Education, Culture, Sports, Science and Technology (MEXT), Japan.

References

[1] J.M. Newsam, M.M.J. Treacy, D.E.W. Vaughan, K.G. Strohmaier, and W.J. Mortier, *J. Chem. Soc. Chem. Commun.* 8, 493 **(1989)**.

[2] J.B. Higgins, R.B. LaPierre, J.L. Schlenker, A.C. Rohrman, J.D. Wood, G.T. Kerr, and W.J. Rohrbaugh, *Zeolites* 8, 446 **(1988)**.

[3] G.R. Millward, S. Ramdas, J.M. Thomas, and M.T. Barlow, *J. Chem. Soc. Faraday Trans.* 2, 79, 1075 **(1983)**.

[4] R.F. Lobo, M. Pan, I. Chan, R.C. Medrud, S.I. Zones, P.A. Crozier, and M.E. Davis, *J. Phys. Chem.* 98, 12040 **(1994)**.

[5] R.F. Lobo, M. Tsapatsis, C.C. Freyhardt, S. Khodabandeh, P. Wagner, C.-Y. Chen, K.J. Balkus, S.I. Zones, and M.E. Davis, *J. Am. Chem. Soc.* 119, 8474 **(1997)**.

[6] A. Philippou and M.W. Anderson, *Zeolites* 16, 98 **(1996)**.

[7] T. Willhammar, J. Sun, W. Wan, P. Oleynikov, D. Zhang, X. Zou, M. Moliner, J. Gonzalez, C. Martínez, F. Rey, and A. Corma, *Nat. Chem.* 4, 188 **(2012)**.

[8] B. Marler, A. Grünewald-Lüke, and H. Gies, *Zeolites* 15, 388 **(1995)**.

[9] H. van Koningsveld and R.F. Lobo, *J. Phys. Chem. B* 107, 10983 **(2003)**.

[10] K. Vinje, J. Ulan, R. Szostak, and R. Gronsky, *Appl. Catal.* 72, 361 **(1991)**.

[11] T. Willhammar and X. Zou, *Zeitschrift Fur Krist.* 228, 11 **(2013)**.

[12] K.P. Lillerud, R. Szostak, and A. Long, *J. Chem. Soc. Faraday Trans.* 90, 1547 **(1994)**.

[13] G.W. Skeels, M. Sears, C. A. Bateman, N.K. McGuire, E.M. Flanigen, M. Kumar, and R.M. Kirchner, *Microporous Mesoporous Mater.* 30, 335 **(1999)**.

[14] G.R. Millward, J.M. Thomas, O. Terasaki, and D. Watanabe, *Zeolites* 6, 91

(1986).

[15] R. Szostak and K.P. Lillerud, *J. Chem. Soc. Chem. Commun.* 20, 2357 **(1994)**.

[16] D.W. Fickel, E. D'Addio, J.A. Lauterbach, and R.F. Lobo, *Appl. Catal. B Environ.* 102, 441 **(2011)**.

[17] Y. Bhawe, M. Moliner-Marin, J.D. Lunn, Y. Liu, A. Malek, and M. Davis, *ACS Catal.* 2, 2490 **(2012)**.

[18] D.S. Santilli and S.I. Zones, *Catal. Letters* 7, 383 **(1990)**.

[19] H.Y. Jeon, C.H. Shin, H.J. Jung, and S.B. Hong, *Appl. Catal. A Gen.* 305, 70 **(2006)**.

[20] R.F. Lobo, S.I. Zones, and R.C. Medrud, *Chem. Mater.* 8, 2409 **(1996)**.

[21] L.S. Dent and J. V. Smith, *Nature* 181, 1794 **(1958)**.

[22] S.I. Zones, *US Pat.* 4,544,538 **(1985)**.

[23] G. Cao and M.J. Shah, *US Pat.* 7,906,099 **(2011)**.

[24] H. Robson, *Verified Syntheses of Zeolitic Materials, Second Revised Edition*, Elsevier, Amsterdam **(2001)**.

[25] G. Jacobs, F. Ghadiali, A. Pisanu, A. Borgna, W.E. Alvarez, and D.E. Resasco, *Appl. Catal. A Gen.* 188, 79 **(1999)**.

[26] M.M.J. Treacy, J.M. Newsam, and M.W. Deem, *Proc. R. Soc. A Math. Phys. Eng. Sci.* 433, 499 **(1991)**.

[27] W.A. Sławiński, D.S. Wragg, D. Akporiaye, and H. Fjellvåg, *Microporous Mesoporous Mater.* 195, 311 **(2014)**.

[28] M. Bourgogne, J.-L Guth, and R. Wey, *US Pat.* 4,503,024 **(1985)**.

Chapter 6

Summary

Chapter 1 is an overview of the entire research. First, the fundamentals of the material focused in this research, zeolites, was shortly described: their structural characteristics, chemical compositions, and chemistry (adsorption, molecular sieving, ion exchange, and catalysis). Then, the synthesis of zeolites was explained with the specific interest on the isomorphous substitution and intergrowth zeolites, which are the main features in the thesis. Finally, another interest of this research, the vehicle emission control was simply reviewed to understand the expected applications of the developed materials.

In Chapters 2–4, I tried to develop a novel catalyst with improved low-temperature activity in the selective catalytic reduction of NO_x with ammonia (NH_3-SCR). Highly dispersed active metal (Fe) in zeolite beta framework was the key concept to achieve the goal. To make Fe atoms be well dispersed, isomorphously substituted Fe-BEA zeolites were hydrothermally synthesized. One possible drawback of this strategy was that they could result in low crystallinity due to narrower synthetic conditions than those of aluminosilicate beta zeolite. Therefore, fluoride was first used to ensure the synthesis of Fe-BEA zeolites. These Fe-BEA zeolites, especially Al-free Fe-BEA zeolite, showed superior performance in the NH_3-SCR compared to

conventional Fe-loaded beta zeolites. With the results of various characterization techniques e.g. UV-Vis, EPR, and XAFS, I showed that the isolated and tetrahedrally coordinated Fe^{3+} species is the most relevant for the NH_3-SCR activity. Finally, I succeeded to synthesize highly crystalline Fe-BEA zeolite without using fluoride, by replacing TEAOH by excess amount of NaOH.

In Chapter 5, another approach was investigated for the development of zeolites for vehicle emission control. Novel AFX/CHA aluminosilicate intergrowth zeolites ZTS-1 and ZTS-2 were synthesized using the dual structure-directing agent (dual-SDA) approach. Control of the AFX/CHA ratio by simple variation of the hydrothermal synthetic parameters proved to be challenging. Cu-loaded ZTS-1 showed higher hydrothermal stability compared to Cu-loaded AFX catalyst. Characterization to verify the intergrowth structure and determine AFX/CHA ratio was also the highlight of the chapter.

In the field of vehicle emission control, functional and hydrothermally stable materials have been always desired and seeking new materials will continue in the future. The works in this thesis should be a part of this movement. The functional evaluation of the zeolites in this thesis has been mostly done on the NH_3-SCR, however, I also expect that these zeolites still have undiscovered and useful functions as catalysts and adsorbents. The results and knowledge of the main features investigated in this thesis, that is, isomorphous substitution and dual-SDA synthesis of intergrowth zeolites will be of use in developing future new materials.

List of publications

1. Y. Naraki, K. Ariga, T. Sano, “Synthesis of Fe-Based BEA Zeolites in Fluoride Media and Their Catalytic Performance in the NH_3-SCR of NO_x”, Adv. Porous Mater. 4, 125 **(2016)**.

2. Y. Naraki, K. Ariga, H. Oka, H. Kurashige, T. Sano, “Fe Species in Isomorphously Substituted Fe-Based BEA Zeolites for Low-Temperature Selective Catalytic Reduction of NO_x”, Adv. Porous Mater. 4, 91 **(2016)**.

3. Y. Naraki, K. Ariga, H. Oka, H. Kurashige, T. Sano, “An isomorphously substituted Fe-BEA zeolite with high Fe content: facile synthesis and characterization”, J. Nanosci. Nanotechnol. *in press*.

4. Y. Naraki, K. Ariga, K. Nakamura, K. Okushita, T. Sano, “ZTS-1 and ZTS-2: Novel intergrowth zeolites with AFX/CHA structure” Microporous Mesoporous Mater. *in press*.

Presentations in domestic / international conference

1. Y. Naraki, K. Ariga, H. Ogawa, “Iron-Substituted *BEA Zeolite for Reduction of NO with NH_3”, 8th International Conference on Environmental Catalysis (ICEC), EC-P-88, August in the US (Asheville, NC) **(2014)**.

2. 楢木祐介、有賀耕、小川宏、『高結晶性 Fe 骨格置換 β ゼオライトの合成とその機能』、第 30 回ゼオライト研究発表会、東京都 **(2014)**

3. 楢木祐介、有賀耕、『新規アルミノシリケートの合成とその同定』、第 31 回ゼオライト研究発表会、鳥取県 **(2015)**

4 Y. Naraki, K. Ariga, “ZTS-1: Novel intergrowth zeolite with AFX/CHA structure”, 18th International Zeolite Conference (IZC), OP-150, June in Brazil (Rio de Janeiro) **(2016)**.

List of patents

1. 楢木祐介、有賀耕、青山英和、『窒素酸化物浄化触媒及び窒素酸化物浄化方法』、特許第 4957176 号 **(2012)**

2. 楢木祐介、有賀耕、青山英和、『窒素酸化物浄化触媒及び窒素酸化物浄化方法』、特許第 5169779 号 **(2013)**

3. 楢木祐介、有賀耕、青山英和、『窒素酸化物浄化触媒及び窒素酸化物浄化方法』、特許第 5309936 号 **(2013)**

4 Y. Naraki, K. Ariga, H, Aoyama, “Nitrogen Oxide-Reducing Catalyst and Method for Reducing Nitrogen Oxide”, US Pat. 7,794,680 **(2010)**.

5 Y. Naraki, K. Ariga, H, Aoyama, “Nitrogen Oxide-Reducing Catalyst and Method for Reducing Nitrogen Oxide”, KR Pat. 101,473,007 **(2009)**.

6. 楢木祐介、有賀耕、『新規メタロシリケート』、特許第 5609620 号 **(2014)**

7 楢木祐介、徳永敬介、有賀耕、『新規メタロシリケート及び窒素酸化物浄化触媒』、特許第 5594121 号 **(2014)**

8 Y. Naraki, K. Tokunaga, K. Ariga “Novel Metallosilicate, Production Method Thereof, Nitrogen Oxide Purification Catalyst, Production Method Thereof, and Nitrogen Oxide Purification Method Making Use Thereof”, WO 2011/078149 A1 **(2011)**.

9 楢木祐介、有賀耕、『β 型鉄シリケート組成物及び窒素酸化物浄化触媒』、特許第 5958070 号 **(2016)**

10 Y. Naraki, K. Ariga, “B-Type Iron Silicate Composition And Method For Reducing Nitrogen Oxides”, US Pat. 9,539,565 **(2017)**.

11 Y. Naraki, K. Ariga, “B-Type Iron Silicate Composition And Method For Reducing Nitrogen Oxides”, KR Pat. 101,512,263 **(2015)**.

12 Y. Naraki, K. Ariga, “B-Type Iron Silicate Composition And Method For Reducing Nitrogen Oxides”, CN Pat. 103,534,210 **(2015)**.

13 楢木祐介、『新規結晶性アルミノシリケート』、特開 2017-65943 号 **(2017)**

Acknowledgements

I would like to express my gratitude to all people who have helped me with the preparation of this doctoral thesis. Especially, I am deeply indebted to my supervisor Prof. Dr. Tsuneji Sano for his advice, support, encouragement and invaluable suggestions concerning science. Without his patient guidance, it is almost impossible to finish my study. I also gratefully acknowledge Mr. Hiroshi Ogawa and Mr. Ko Ariga (Tosoh Corporation) for teaching me laboratorial techniques and work as well as valuable suggestions, giving me opportunities to pursue the investigation of the unique materials in this thesis, and allowing me to publish them. I must express special gratitude to the people in TOSOH Analysis and Research Center, Mr. Hideyuki Oka, Mr. Hirokazu Kurashige, Mr. Kazuto Nakamura, and Dr. Keiko Okushita for the valuable characterization data and generous help on interpretation.

I am grateful to all of the members in Zeolite Group, Tosoh Inorganic Materials Research Laboratory for their cooperation to my work.

Finally, I dedicate this thesis to my wife and children for their love, patience, and great encouragement.

September 2017

Yusuke Naraki